Four Novel Electron Point Source Applications

Dissertation
zur
Erlangung der naturwissenschaftlichen Doktorwürde
(Dr. sc. nat.)
vorgelegt der
Mathematisch-naturwissenschaftlichen Fakultät
der
Universität Zürich
von

Flavio Bruno Wicki

aus
Aristau AG

Promotionskomitee
Prof. Dr. Hans-Werner Fink (Vorsitz)
Prof. Dr. Peter Hommelhoff
Prof. Dr. Jürg Osterwalder
Dr. Roger Morin
Dr. Jean-Nicolas Longchamp
Dr. Conrad Escher

Zürich, 2016

Die vorliegende Arbeit wurde von der mathematisch-naturwissenschaftlichen Fakultät der Universität Zürich im Herbstsemester 2016 als Dissertation angenommen.

Promotionskomitee:

Prof. Dr. Hans-Werner Fink (Vorsitz)
Prof. Dr. Peter Hommelhoff
Prof. Dr. Jürg Osterwalder
Dr. Roger Morin
Dr. Jean-Nicolas Longchamp
Dr. Conrad Escher

Abstract

In the work presented here, four novel applications employing an ultra-sharp tungsten tip as a coherent electron point source are introduced.

The first part of the thesis describes the design and fabrication of a micron-sized electron column as a tool to collimate a divergent beam emitted by an electron point source into a parallel beam. The design criteria follow the notion of scaling down source size, lens-dimensions and kinetic electron energy for minimizing spherical aberrations. The column has an overall length of 700 micrometers and comprises two electron lenses: A two-electrode micro-lens with a minimal aperture diameter of 1 micrometer and a three-electrode mini-lens with an aperture diameter of 50 micrometers. The apertures are successively milled through stacks of sub-micron thick membrane electrodes using a gallium ion beam, ensuring high circularity on a well defined optical axis. The micron-sized column is demonstrated to collimate a divergent electron beam into a nearly parallel beam with a quasi-planar wave front characterized by a minimal full divergence angle of 4 mrad and electron energies as low as 100 eV.

In the second part of the thesis the development of a dedicated instrument is presented, which combines the technologies of low-energy electron point source microscopy and scanning probe microscopy. The new instrument allows to study freestanding graphene and adsorbate thereon with ultra-low-energy electrons and source-to-sample distances in the nanometer range. A novel type of scanning probe microscopy is presented, in which the relative absorption of the sample with respect to low-energy electrons emitted by an electron point source is employed as the contrast signal.

Angle-resolved electron transmission measurements through freestanding graphene sheets in the energy range of 18 to 30 eV have been carried out in the new instrument. As the transmission characteristics depend on the coupling of the incident electrons to the electronic states in the sample, this allowed to map unoccupied states above the vacuum level in freestanding graphene for the first time. The measurements are consistent with theoretical predictions of a scattering resonance in the band structure of graphene.

Furthermore, the origin of non-reconstructable features observed in low-energy electron holograms of freestanding graphene samples is investigated. A comparison with simulations reveals that they are caused by charged adsorbates. It is demonstrated that low-energy electron holography constitutes a unique probing tool to directly visualize charge distributions with a sensitivity of a fraction of an elementary charge. Spatial resolution in the nanometer range and fast data acquisition allows to investigate charge transfer processes and adsorbate diffusion.

Zusammenfassung

In der vorliegenden Doktorarbeit werden vier neue Anwendungen vorgestellt, welche auf ultrascharfen Wolframspitzen als Punktquellen von kohärenten Elektronen beruhen.

Der erste Teil der Arbeit beschreibt die Entwicklung und Herstellung einer submillimetergrossen elektronenoptischen Säule zur Bündelung eines divergenten Elektronenstrahls aus einer Elektronen-Punktquelle in einen parallelen Strahl. Die Kriterien für das Design beruhen auf der Idee, durch Verringern der Quellengrösse, der Linsendimensionen und der kinetischen Elektronenenergie sphärische Aberrationen zu minimieren. Die Elektronensäule hat eine Gesamtlänge von 700 Mikrometern und besteht aus zwei Elektronenlinsen: Einer Mikro-Linse mit zwei Elektroden und einem minimalen Aperturdurchmesser von 1 Mikrometer und einer Mini-Linse mit drei Elektroden und einer Apertur von 50 Mikrometern Durchmesser. Diese Aperturen werden mittels eines fokussierten Gallium-Ionen-Strahls sukzessiv durch einen Stapel von submikrometer-dicken Membranelektroden gebohrt, um eine wohldefinierte optischen Achse zu garantieren. Die Mikrolinse bündelt einen divergenten Elektronenstrahl nachweislich in einen annähernd parallelen Strahl mit einer quasi-planaren Wellenfront, charakterisiert durch einen minimalen Divergenzwinkel von 4 mrad und Elektronenenergien von lediglich 100 eV.

Im zweiten Teil der Arbeit wird die Entwicklung eines dedizierten Instruments beschrieben, welches die Technologien von niederenergetischer Elektronenpunktquellen-Mikroskopie und Rastersondenmikroskopie kombiniert. Dieses neue Instrument ermöglicht es, freitragendes Graphen und darauf gebundene Adsorbate mit Niedrigstenergie-Elektronen und Abständen zwischen Quelle und Probe im Nanometerbereich zu untersuchen. Ein neuartiges Rastersondenmikroskop wird präsentiert, bei welchem die relative Absorption von niederenergetischen Elektronen durch die Probe als Kontrastsignal verwendet wird.

Unter Verwendung des neuen Instruments wurden winkelaufgelöste Messungen der Elektronentransmission durch freitragende Graphen-Filme im Energiebereich von 18 bis 30 eV durchgeführt. Da die Transmissionscharakteristik durch die Wechselwirkung der einfallenden Elektronen mit den elektronischen Zuständen in der Probe bestimmt ist, erlauben diese Messungen erstmalig die Abbildung unbesetzter Zustände oberhalb des Vakuumniveaus von freitragendem Graphen.

Desweiteren wurden in niederenergetischen Elektronen-Hologrammen von freistehenden Graphen-Proben nicht-rekonstuierbare Signaturen beobachtet und deren Ursache untersucht. Der Vergleich mit Simulationen zeigt, dass diese Signaturen durch geladene Adsorbate hervorgerufen werden. Es wird gezeigt, dass niederenergetische Elektronen-Holographie eine einzigartige Methode darstellt, um Ladungsverteilungen im Bereich von Bruchteilen einer Elementarladung direkt zu visualisieren. Eine räumliche Auflösung im Nanometerbereich und

schnelle Datenerfassung ermöglichen zudem, Prozesse von Ladungsverschiebungen und die Diffusion von Adsorbaten zu untersuchen.

List of acronyms

AC-FESPM	absorption contrast field emission scanning probe microscopy
ADC	analog-to-digital converter
ARPES	angle-resolved photoelectron spectroscopy
ARSEE	angle-resolved secondary electron emission
CCD	charge-coupled device
CDI	coherent diffraction imaging
CVD	chemical vapor deposition
DAC	digital-to-analog converter
DFT	density functional theory
DNA	deoxyribonucleic acid
DSP	digital signal processor
EPS	electron point source
FESPM	field emission scanning probe microscopy
HOPG	highly oriented pyrolytic graphite
LEEM	low-energy electron microcopy
LEEPS	low-energy electron point source
MCP	micro-channel plate
NA	numerical aperture
NEG	non-evaporable getter
NFESEM	near field emission scanning electron microscopy
PMMA	polymethyl methacrylate
SEM	scanning electron microscopy
SPM	scanning probe microscopy
STEM	scanning transmission electron microscopy
STM	scanning tunneling microscopy
TEM	transmission electron microscopy
TMP	turbo molecular pump
uhp-H_2O	ultra-highly purified water

UHV	ultra-high vacuum
VLEED	very low energy electron diffraction

Contents

CHAPTER 1

Introduction

1.1 Short Introduction to Electron Microscopy

Microscopy has long since been a major driving force for progress in the natural sciences. The first microscopes relied on visible light as the imaging radiation, and such optical microscopes are still widely used. However, already 1873 Ernst Abbe recognized a fundamental resolution limit for conventional microscopes related to the wavelength of the radiation that is employed [1]. The Abbe diffraction limit $d = \lambda/(2 \cdot NA)$ relates the resolvable feature size d of a microscope to its numerical aperture (NA) and the wavelength λ of the radiation. Due to the large wavelength of visible light (about 390 to 700 nm), this limits the minimum resolvable distance of conventional optical microscopes to about 200 nm.

To overcome the resolution limit of visible light, scientists started to use electrons as the imaging radiation due to the significantly shorter wavelength (e.g. 0.01 nm for 10 keV electron energy). The first transmission electron microscope (TEM) was built in 1931 by Max Knoll and Ernst Ruska [2,3], and since then considerable progress was made both in methods and instrumentation. For decades however, the resolution in electron microscopy was limited by the poor quality of electron lenses. Already 1936, Otto Scherzer established a theorem that conventional stationary, rotationally symmetric electron lenses without space charges always exhibit aberrations in the same direction [4], and thus, unlike to light microscopy, it is not possible to correct for poor lens quality by employing several lenses in a row.

It was for this reason, that Dennis Gabor proposed *"a new microscopic principle"* in 1948 [5], today known as holography. He recognized that not only the amplitude of the object wave but also its phase, which is lost in a classical microscopy scheme, can be obtained by recording an interference pattern – the so called hologram – formed by the coherent superposition of the object wave with a well-known reference wave. The propagation of the object wave is completely determined by is amplitude and phase distribution in any plane of the optical setup. It is therefore possible to reconstruct the object by optical or numerical methods from a hologram recorded in a lens-less scheme, thus eliminating at all the need to use electron lenses afflicted with aberration. However, holography needs a high degree of coherence of the electron waves involved, a prerequisite that was not given with the electron sources available at that time.

Another approach to improve the resolution in electron microscopy involves the use of electron lenses that avoid one or more of the constraints of the Scherzer theorem [6]. The implementation of multipole correctors in the 1990s to compensate for spherical aberration finally allowed for atomic resolution in transmission electron microscopes and such correctors are now commercially available in state-of-the-art instruments [7].

Despite the tremendous progress in electron optics, conventional electron microscopy operating typically at beam energies in the order of 100 keV faces severe limitations when it comes to study low-atomic-number materials. Imaging at a reasonable contrast is difficult, as the scattering cross-sections of light atoms are very small for high energy electrons. Furthermore, the high-energy electrons likely deteriorate the sample by radiation damage.

This lead to a recent trend in aberration-corrected electron microscopy towards lower beam energy [8, 9] and atomic resolution was achieved with transmission microscopes operating at electron energies as low as 15 to 40 keV [10–12].

However, even at such relatively low beam energies (compared to traditional TEMs), radiation damage is the limiting factor in terms of resolution when it comes to study sensitive matter as for example biological molecules. Such fragile structures are destroyed by electron beam illumination even at a few keV due to inelastic processes long before the necessary dose for a decent image quality is reached [13–15].

Damage-free imaging of a biomolecule is only possible at much lower electron energy: It was shown that DNA molecules can be irradiated for an extended time by electrons with energies in the range of 30 to 250 eV with no detectable radiation damage [16]. As such low-energy electrons still have wavelengths in the Ångstrom range, they offer the potential for imaging individual biological molecules at atomic resolution.

Aberration correction techniques become extremely challenging and complicated for beam energies below 10 keV and it is foreseeable that future TEMs will not reach electron energies as low as a few 100 eV [17]. It is therefore necessary to pursue the development of alternative techniques as for example those presented in the next section.

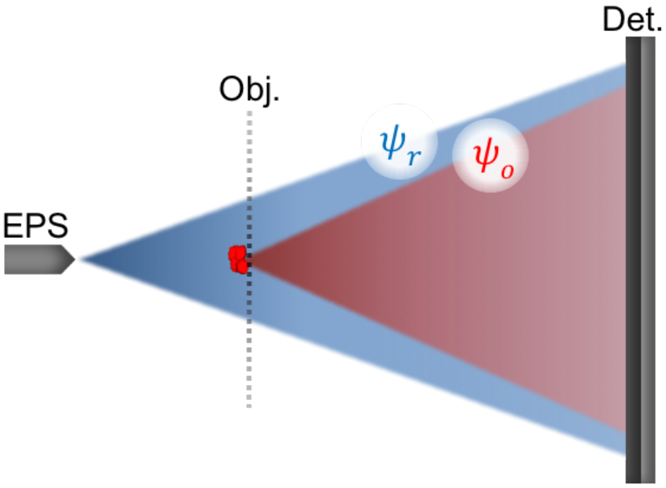

Figure 1.1: Scheme of in-line holography in the LEEPS microscope. A divergent beam of low-energy electrons is emitted by an electron point source **(EPS)**. Part of the beam is scattered by the object **(Obj.)** and forms the object wave (ψ_o). The part that passes the object without scattering forms the reference wave (ψ_r). The superimposed waves are recorded as the hologram at the detector **(Det.)**.

1.2 Imaging with Coherent Low-Energy Electrons

The main goal of the research activity of Prof. Hans-Werner Fink's group at the University of Zürich is the development of the methodology and technology to study individual biomolecules at atomic resolution. Two techniques are experimentally explored to reach this goal: Low-energy electron holography and coherent diffraction microscopy (CDI). These methods are briefly introduced in the next two sub-sections to provide the scientific background for the thesis presented here.

Both techniques combine two tremendous advantages over conventional electron microscopy techniques. First, as no lenses are employed between object and detector, the resolution is not affected by lens aberrations. Second, the object information is gathered by low-energy electrons, the only known radiation with sub-atomic wavelength that allows for damage-free illumination of biological molecules.

As the techniques are based on the detection of an interference pattern, a highly coherent ensemble of low-energy electrons is required to probe the object. Such an ensemble is created by field emission from an ultra-sharp metal tip with one or a few atoms at its apex – a so-called electron point source (EPS) [18]. The spatial coherence is ensured by the small virtual source size of atomic dimension [19] and the temporal coherence is ensured by the low energy spread inherent to an electron ensemble created by field emission in a Fowler-Nordheim tunneling process [20,21].

1.2.1 Holography in the Low-Energy Electron Point Source Microscope

With the advent of highly coherent field emission electron sources and the invention of the low-energy electron point source (LEEPS) microscope shortly thereafter [22], Gabor's original idea of in-line holography finally became feasible.

The basic scheme of holography in the LEEPS microscope is presented in Fig. 1.1. A divergent beam of low-energy electrons emitted by an electron point source is used to illuminate an object placed in a close distance and its projection image is recorded at a distant detector. The magnification of such an imaging setup is simply given by the ratio of source-detector and source-sample distances and easily reaches 1 million for the distances typically involved. Due to the wave nature of the low-energy electrons, not a simple shadow image is formed but the interference of an object wave and a reference wave leads to the formation of a hologram.

The object wave ψ_o is formed by the part of the incident wave that is elastically scattered by the object whereas the undisturbed part of the incident wave that passes the object without scattering forms the reference wave ψ_r. In the detector plane (x_d, y_d) the intensity of the two superimposed waves is detected as the hologram $\mathcal{H}(x_d, y_d)$:

$$\mathcal{H}(x_d, y_d) = |\psi_r(x_d, y_d)|^2 + |\psi_o(x_d, y_d)|^2 + \psi_r(x_d, y_d)\psi_o^*(x_d, y_d) + \psi_r^*(x_d, y_d)\psi_o(x_d, y_d), \quad (1.1)$$

The last two terms of the equation are responsible for the interference pattern created by the interference of the reference and object waves and contain amplitude and phase information of the waves. The first term is a background from the reference wave alone and can easily be subtracted, and the second term is usually small enough to be neglected. The amplitude and phase information of the object can be retrieved from the hologram if the reference wave is known. This is usually done numerically, by multiplication with the reference wave and back-propagation to the object plane [23].

LEEPS microscopy has for example been employed to image carbon fibers [24–26], carbon nanotubes [27,28], tungsten tips [29,30], MgO crystallites [29], as well as biological entities such as DNA [31–33], phthalocyaninato polysiloxane [34], tobacco mosaic viruses [35,36], individual filamentous phage [37] and ferritin [38].

1.2.2 Coherent Diffraction Imaging with Low-Energy Electrons

Coherent diffraction imaging constitutes an alternative approach to holography. Here, the object is illuminated with a plane wave and the far-field diffraction pattern is recorded. The

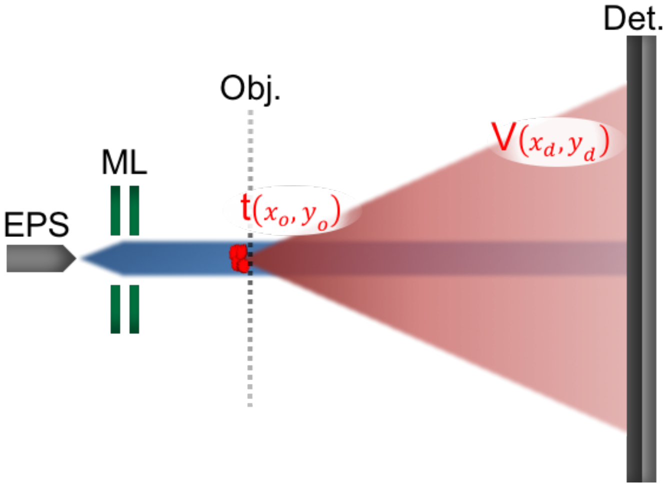

Figure 1.2: Scheme of coherent diffraction imaging with low-energy electrons. A divergent beam of low-energy electrons emitted by an electron point source **(EPS)** is collimated into a parallel beam by a micro-lens **(ML)** and directed towards the object **(Obj.)**. The diffracted wave in the far-field **($V(x_d, y_d)$)** corresponds to the Fourier transform of the object transmission function **($t(x_d, y_d)$)**, and its intensity is recorded at the detector **(Det.)**.

experimental scheme of CDI with low-energy electrons is rather similar to the scheme of in-line holography, but the divergent beam of the electron point source is collimated into a parallel beam by a lens between source and object, as sketched in Fig. 1.2.

As the scattered wave in the far-field $V(x_d, y_d)$ is given by the Fourier transform of the object transmission function $t(x_o, y_o)$, knowledge of the latter would allow to simply reconstruct the object by inverse Fourier transformation $t(x_o, y_o) = \mathcal{F}^{-1}(V(x_d, y_d))$. However, as only the intensity $I(x_d, y_d) = |V(x_d, y_d)|^2$ can be recorded in the experiment, the phase of the scattered wave is unknown. This is known as the so-called phase problem.

In the pioneering work of Sayre [39], Gerchberg and Saxton [40] and Fienup [41], it was recognized and demonstrated that the phase can be recovered from a diffraction pattern alone, if the pattern is sampled with at least double the Nyqvist frequency. The phase recovery is based on iterative algorithms involving the back and forth propagation of the wave between detector and object plane. In the beginning, usually a random phase is assigned to the wavefront. In every iteration step, constraints on the amplitude or phase distribution of the wave are applied in the object or detector plane and the amplitude in the detector plane is replaced by the square root of the intensity of the experimental diffraction pattern. Typical constraints are to impose restrictions on the object localization or that there is only non-negative absorption.

As a plane wave is required for CDI, the divergent electron beam from the electron point source has to be shaped into a parallel beam. In our laboratory this is realized up to now in the CDI setup by a micro-lens – an electrostatic lens made up of two electrodes with an aperture diameter as low as 1 µm. As the aberrations of an electron lens are proportional to the lens dimension, such a small lens allows to converge the divergent beam into an almost parallel beam with a residual beam divergence angle of only a few mrad [42]. A micro-lens was used to record coherent low-energy electron diffraction patterns of a nanotube bundle [43], individual carbon nanotubes [44] and a freestanding graphene sheet of 210 nm in diameter [45]. The latter was reconstructed with almost atomic resolution of 2 Ångstrom revealing about 660’000 graphene unit cells from a single diffraction record which shows the high potential of CDI with low-energy electrons.

1.3 Scope of this Thesis

The first part of the thesis describes the development of an improved electron optical system in which instead of using a single micro-lens to form a parallel electron beam, an entire miniaturized electron column consisting of a two electrode micro-lens and a mini-lens is used. The mini-lens consists of three electrodes with aperture diameters of slightly larger dimensions than the micro-lens apertures. The main idea behind this approach was to prefocus the divergent beam with the micro-lens and subsequently use the mini-lens to form the quasi-parallel beam. The apertures of the lens were milled in a focused ion beam system in a two step process to ensure a good alignment of the two lens components. This allowed to fabricate a miniaturized electron column with aperture diameters ranging from 1 to 50 µm and an overall length of only 700 µm.

The electron optical performance of the column was tested experimentally and a nearly parallel beam with a residual half divergence angle of 2 mrad was demonstrated. First experimental tests in illuminating a sample with the parallel beam from the miniaturized column in a CDI like setup showed that it is very difficult to position the parallel beam at the desired sample region. The work concerning the miniaturized electron column is presented in chapter 2.

The second part the thesis describes the redesign of a LEEPS microscope. Not only was it optimized to work at small tip-to-sample distances but also its functionality was extended to perform scanning probe microscopy (SPM). The new experimental setup is employed to study freestanding graphene samples. This sample was chosen for its high transparency to low-energy electrons, making it an optimal substrate for LEEPS imaging [46, 47]. The LEEPS/SPM setup and proof-of-principle results are presented in chapter 3, including a novel type of scanning probe microscopy, in which the sample is probed with a beam of field-emitted electrons and the current absorbed by the sample is employed as a contrast signal.

The combined LEEPS/SPM system moreover allows to acquire angle-resolved transmission measurements on freestanding graphene for electron energies down to 18 eV. This allowed to map unoccupied states in the electronic structure of freestanding graphene for the first time, as described in chapter 4.

In chapter 5 the high sensitivity of low-energy electrons to local electric fields is employed to directly visualize charge distributions with a sensitivity of a fraction of an elementary charge.

CHAPTER 2

Design and Implementation of a Micron-Sized Electron Column Fabricated by Focused Ion Beam Milling

The following chapter contains a modified version of a manuscript published in Ultramicroscopy:

F. Wicki, J.-N. Longchamp, C. Escher, H.-W. Fink, *Design and Implementation of a Micron-Sized Electron Column Fabricated by Focused Ion Beam Milling*, Ultramicroscopy **160**, 74-79, 2016.

Abstract

We have designed, fabricated and tested a micron-sized electron column with an overall length of about 700 microns comprising two electron lenses; a micro-lens with a minimal bore of 1 micron followed by a second lens with a bore of up to 50 microns in diameter to shape a coherent low-energy electron wave front. The design criteria follow the notion of scaling down source size, lens-dimensions and kinetic electron energy for minimizing spherical aberrations to ensure a parallel coherent electron wave front. All lens apertures have been milled employing a focused ion beam and could thus be precisely aligned within a tolerance of about 300 nm from the optical axis. Experimentally, the final column shapes a quasi-planar wave front with a minimal full divergence angle of 4 mrad and electron energies as low as 100 eV.

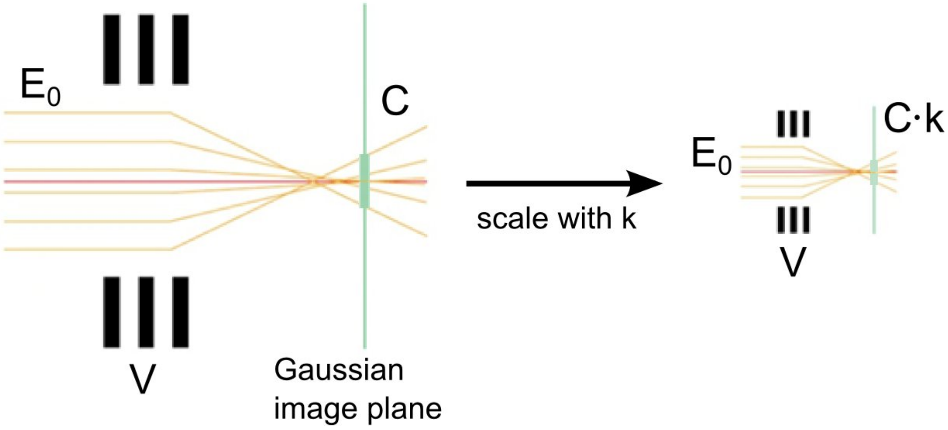

Figure 2.1: Downsizing approach for low aberrations in electrostatic electron lenses. When scaling down the size of a lens by a factor k, the geometrical aberrations are reduced by that same factor, provided that the ratio of the electron energy E_0 to the electrode potential V is preserved. C denotes the transversal spherical aberration of the lens.

2.1 Introduction

In past decades, electron microscopy has made significant progress, in particular by the realization and implementation of aberration correcting elements [48,49]. This has led to commercial transmission electron microscopes that routinely deliver atomic resolution in material science research. A current trend is to reduce beam energies from 100 keV, a typical value 10 years ago, down to energies in the several 10 keV regime [50,51]. The goal is to minimize knock-out damage and thus tolerate a reasonably high electron dose to achieve good signal to noise ratios and to even envision acquiring spectroscopic data on a single atom level.

Even lower energies in the 100 keV range are employed to operate microscopes with high surface sensitivity which has led to the impressive technology of LEEM pioneered by Telieps and Bauer some 30 years ago [52]. Recent versions of these surface sensitive tools are also equipped with aberration correctors to push the lateral resolution limit to or even below the nanometer range [53,54]. Related devices, also using a cathode lens close to the sample to decelerate the electron beam, are lately used in the SEM and STEM modes [55,56].

Comparably few efforts have been made in the development of electron microscopes operating in the 100 eV regime by which the electron energy is kept low throughout the entire electron column [57–60] instead of decelerating the beam just where the low energy is needed, close to the sample. Such efforts require scaled down electron lenses and enable technologies like coherent diffraction with low-energy electrons which has recently entered

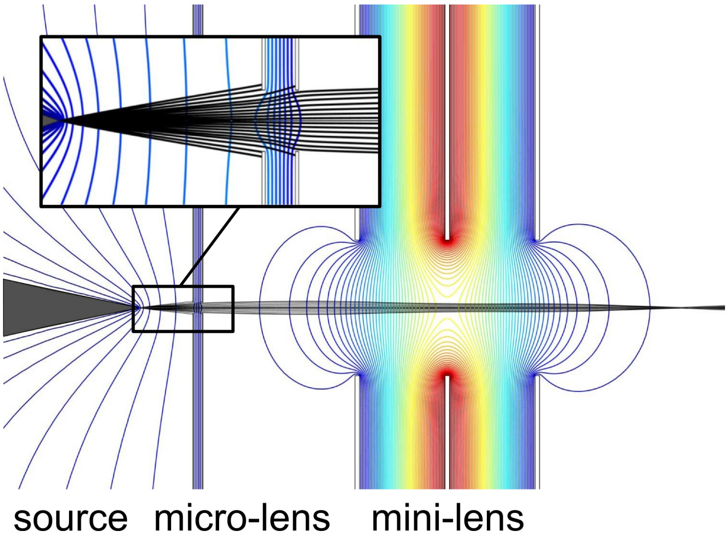

Figure 2.2: Schematic of the working principle of the micro-column, not drawn to scale. Potential differences applied between the two micro-lens electrodes and between the middle and outer mini-lens electrodes create an electrostatic field distribution which has a focusing effect on the divergent electron beam emitted by the field emission source. The inset shows an enlarged view of the micro-lens apertures.

the 2 Ångstrom resolution regime in imaging freestanding graphene [45]. Scaling down lens dimensions while maintaining atomic source size [18] and low emission voltages right at the field emission tip level leads to reduced lens aberrations. This concept is illustrated in Fig. 2.1. For reaching a scaling factor of 1000 or more, lenses need to be machined with sub-micron precision.

If the geometrical dimensions of a given electrostatic electron lens are scaled down by a constant factor k while the ratio of the electrode potentials to the beam energy remains unchanged, the run of the electron trajectories is scaled down by the same factor k. The geometrical aberrations given as deviations of the ray trajectories from the optical axis in the Gaussian image plane thus scale with k as well.

2.2 Concept

In coherent diffraction imaging (CDI), micro-fabricated electron lenses have proven to be a suitable tool to shape a spherical wave front emitted from a field emission tip into a nearly parallel one [42, 43]. A micron-sized two electrode electron lens (micro-lens) has already been successfully employed in CDI experiments [45]. To get more control over the beam properties, we took the effort to incorporate a second electron optical element placed behind such a micro-lens. Sticking to the downsizing approach, an electrostatic three electrode lens (mini-lens) with small dimensions was chosen as the second element to keep the aberrations low.

The setup of this five electrode electron optical column (micro-column) is illustrated in Fig. 2.2. It consists of a micro-lens with aperture diameters in the range of 1 to 5 µm, followed by a mini-lens with a maximum aperture diameter of 50 µm. The micro-lens acts as both, beam limiting aperture and extractor for field electron emission. If a potential difference between the two electrodes is applied, an electrostatic field distribution around the apertures is formed, which has a focusing effect on a penetrating electron beam. Pre-shaped like this, the electron beam subsequently enters the mini-lens. The outer electrodes of the latter are usually kept at ground potential and either a negative (retarding mode) or a positive voltage (accelerating mode) is applied to the middle electrode. In either mode, the electrons experience a net acceleration towards the optical axis and provided that the voltage relative to the electron energy is high enough, the electron beam converges.

In order to control the beam energy throughout the column, the electron emitter as well as the micro-lens can be biased with respect to the mini-lens. This is of particular relevance for diffraction experiments in view of tuning the wavelength of the electrons.

2.3 Micro-Column Fabrication Procedure

The building blocks for the micro-column fabrication are commercially available 100 nm thick silicon nitride membranes covering a 250x250 μm^2 window in a 100 µm thick silicon substrate. According to the number of electrodes, the micro-lens and the mini-lens are pre-assembled to stacks of two and three building blocks respectively, using vacuum compatible epoxy. The fabrication procedure is summarized in Fig. 2.3.

2.3.1 Mini-Lens

For the electrode fabrication of the mini-lens, all three building blocks are first coated with gold on both sides. In order to electrically insulate the individual electrodes within the stack, they are separated by a 75 µm thick polyimide foil leading to a total membrane to membrane spacing of about 200 µm. The polyimide spacers are gold coated on one side and hence allow for electrically contacting the electrodes. Once such stack of spacers and membranes is assembled, all three apertures are ion milled through the membranes along the stack axis in a single run (see Fig. 2.3 (a) and (b)). After milling, the silicon nitride rims of the apertures need sputter coating in order to prevent charging during operation (see Fig. 2.3 (c)). SEM and scanning ion microscopy images of the mini-lens are shown in Fig. 2.4.

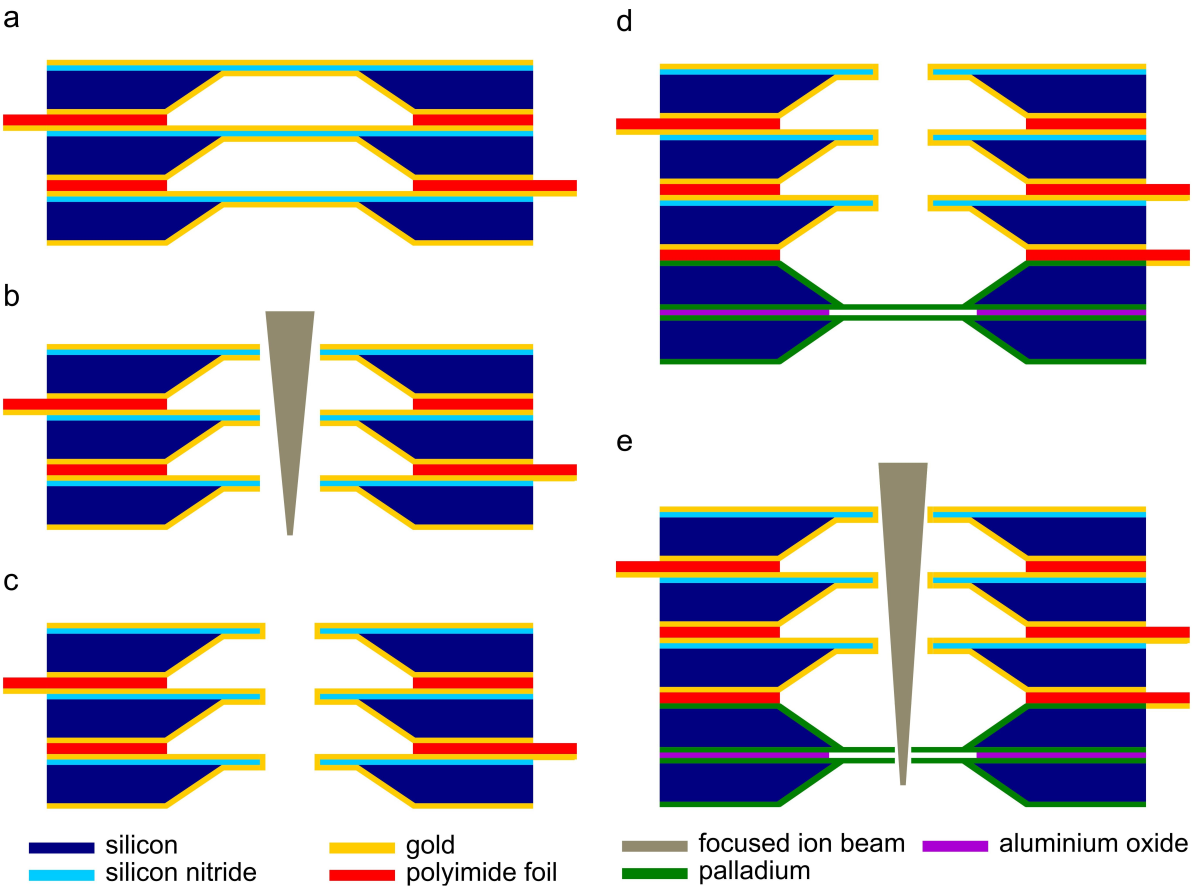

Figure 2.3: Illustration of the micro-column fabrication procedure. **(a)** Three silicon chips are stacked for the mini-lens fabrication. **(b)** The apertures of the mini-lens are milled using a focused gallium ion beam. **(c)** The apertures are sputter coated with gold to cover the silicon nitride revealed during milling. **(d)** The micro-lens stack is bonded to the mini-lens. **(e)** Finally the micro-lens apertures are milled via the mini-lens apertures.

2.3.2 Micro-Lens

For the pre-assembly of the micro-lens electrodes, two building blocks are first coated with a 200 nm thick palladium layer on the upper surface only. Thereafter, the supporting silicon nitride windows are removed by reactive ion etching leaving freestanding palladium membranes behind. For subsequently contacting the electrodes, the building blocks are now additionally palladium coated on the bottom surface. Finally, a 1 µm thick aluminum oxide frame is electron beam evaporated around the palladium membrane on the upper side for electrical insulation. Prepared like this, the two building blocks are assembled with the aluminum oxide layers facing each other. This leads to a total membrane to membrane spacing

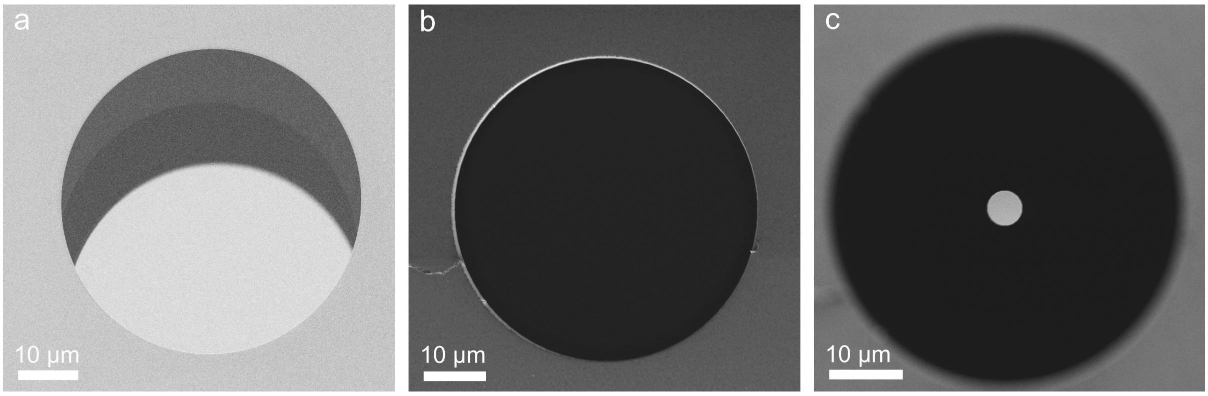

Figure 2.4: Scanning electron and ion microscopy images of the micro-column elements. **(a)** SEM image recorded with the sample tilted to display the three mini- lens apertures. **(b)** Scanning ion microscopy image of the mini-lens exit aperture, illustrating its high circularity. **(c)** Scanning ion microscopy image of a micro-lens aperture with 5 µm in diameter viewed through the mini-lens revealing accurate alignment of the two lenses. The focus is adjusted to the micro-lens.

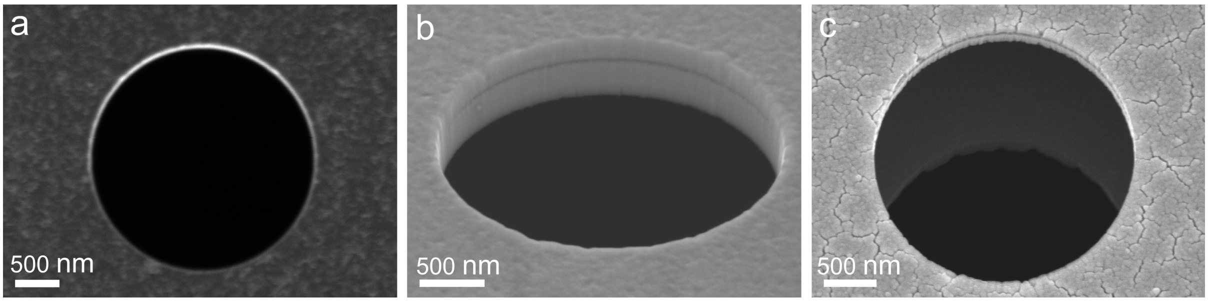

Figure 2.5: Scanning electron and ion microscopy images of the micro-lens. **(a)** Scanning ion microscopy image of a 2.5 µm aperture in a freestanding palladium membrane, recorded right after milling. **(b)** SEM image of the aperture recorded under an angle of 54°. **(c)** SEM image of a micro-lens recorded under an angle of 23° presenting both apertures.

of approximately 5 µm. SEM and scanning ion microscopy images of micro-lens apertures are shown in Fig. 2.5.

2.3.3 Micro-Column

In order to build a micro-column, the micro-lens pre-assembly is attached onto the mini-lens (see Fig. 2.3 (d)). Again, the two lenses are insulated by a polyimide foil, gold coated on one side to provide electrical contact to the exit electrode of the micro-lens. The electrode

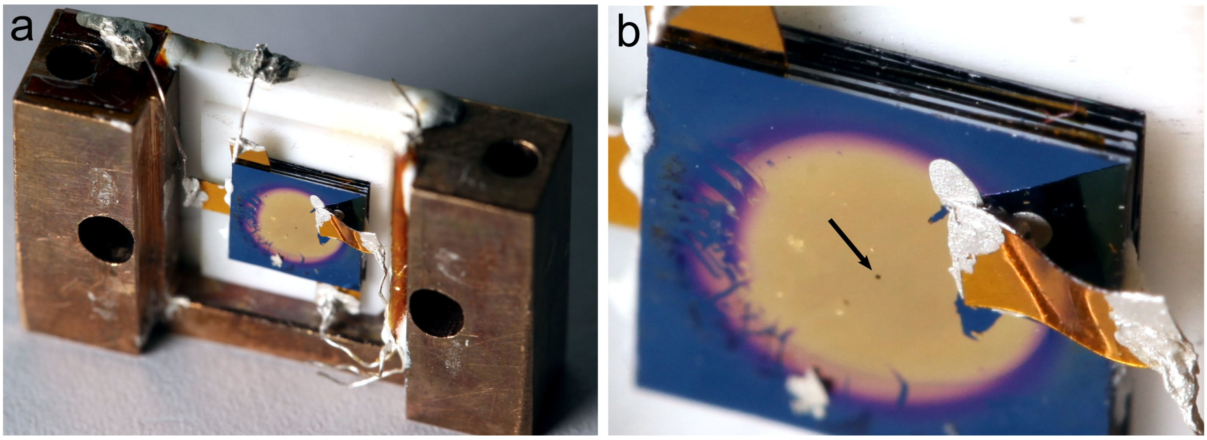

Figure 2.6: Photographs of the mounted micro-column. **(a)** The micro-column is mounted on a sample holder for testing in an UHV system. The overall sample holder width amounts to 19 mm. The view is towards the exit side of the column. **(b)** Close up view of the column. The arrow points to the last 50 µm diameter mini-lens aperture.

spacing between exit of the micro-lens and inlet of the mini-lens adds up to about 300 µm. The apertures in the palladium membranes of the micro-lens are finally milled from the exit of the column via the apertures of the mini-lens (see Fig. 2.3 (e)). In this way an alignment of both lenses within less than 300 nm can be attained (see Fig. 2.4 (c)). As estimated from SEM images, the micro-lens aperture roundness can be milled with an accuracy better than 20 nm concerning bore radius variation. The corrugation of the palladium coat at the rim of the bore may aggregate up to 50nm.

2.4 Experimental Characterization

Prior to experimental tests under UHV conditions, at a pressure lower than 1×10^{-9} mbar, the micro-column is mounted on a sample holder. In doing so, the electrodes are contacted using silver paint (see Fig. 2.6). During operation of the micro-column no increase in pressure is observed.

An electrochemically etched W(111) field emission tip is used as source of a divergent coherent low-energy electron beam. The field emitter is mounted on a 3-axis piezo-positioner and can thus be precisely positioned in front of the micro-lens. In order to optimize its performance, the electron source is annealed before operation.

For monitoring the performance of the micro-column, a detector unit featuring a microchannel plate followed by a phosphor screen is placed at a distance of 70mm beyond the micro-column. The entrance of the microchannel plate is on ground potential to establish a field free

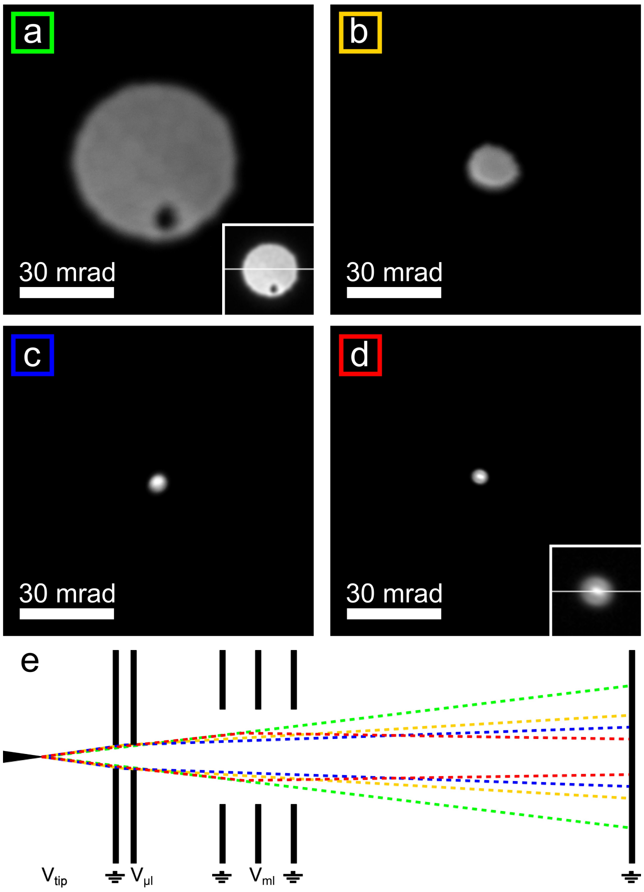

Figure 2.7: Performance of a micro-column consisting of a micro-lens with 2.5 µm apertures and a mini-lens with 50 µm apertures. **(a)-(d)** Beam spots recorded for different voltages $V_{\mu l}$ on the second micro-lens aperture and V_{ml} on the middle mini-lens aperture. All the other lens electrodes are at ground potential while the tip potential is kept at $V_{tip} = -100$ V. **(a)** Projection image of the second lens aperture ($V_{\mu l} = 0$ V, $V_{ml} = 0$ V). The black spot visible inside the projection image is due to a defect on the detector. **(b)** The divergence angle of the electron beam is reduced by the micro-lens ($V_{\mu l} = -40$ V, $V_{ml} = 0$ V). The deviation from rotational symmetry of the recorded spot may arise from a slight misalignment of the optical elements as well as from work function variations caused by adsorbates on the rim of the second micro-lens aperture detracting the trajectories of the 60 eV electrons. **(c)** Minimal beam spot in case solely the micro-lens is used to shape the beam ($V_{\mu l} = -53$ V, $V_{ml} = 0$ V). **(d)** Minimal beam spot experimentally attained when micro- and mini-lens are operated in combination ($V_{\mu l} = -40$ V, $V_{ml} = 160$ V). **(e)** Sketch of the micro-column and the beam envelope for the different conditions discussed above: green corresponds to the condition shown in (a), orange (b), blue (c) and red (d).

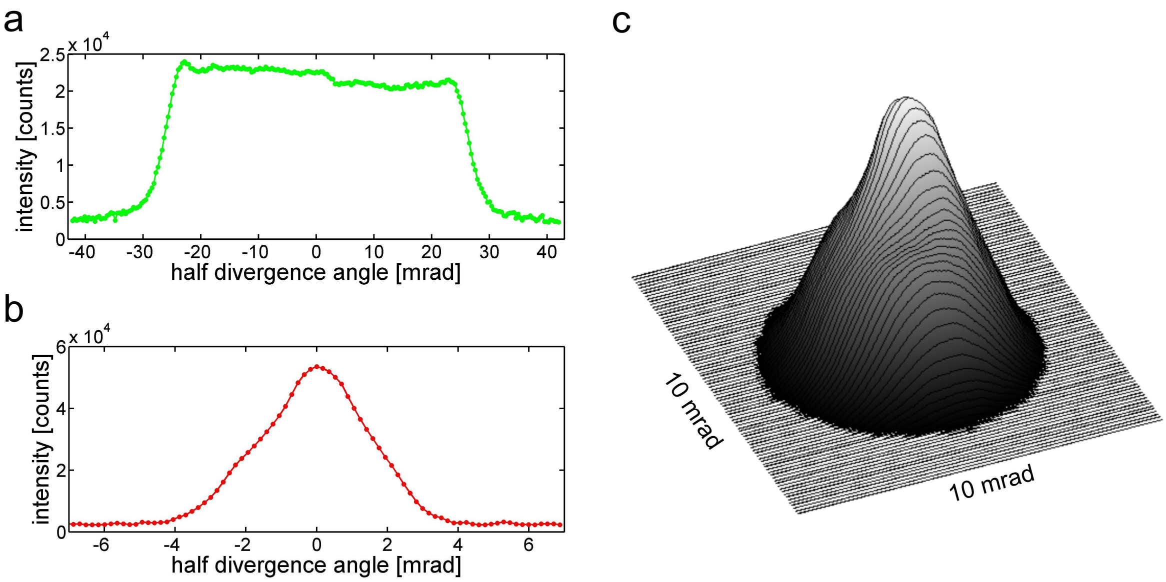

Figure 2.8: **(a)** Intensity profile along the line shown in the inset in Fig. 2.7 (a). The intensity variation reflects the non uniform field emission current density within the emission angle forming the projection image. **(d)** Intensity profile along the line shown in the inset in Fig. 2.7 (d). **(c)** 3-dimensional representation of the beam intensity profile from the spot in Fig. 2.7 (d).

region between the micro-column and the detector unit. The signal on the screen is captured by a CCD camera with 6000x8000 pixels and 16 bit dynamic range.

When all the micro-column electrodes are kept at ground potential, a projection image of the second micro-lens electrode aperture is recorded on the detector screen (see Fig. 2.7 (a)). Since this is the beam limiting aperture of the system, the projection image implies the maximum acceptance angle of the micro-column. Due to the large distance of the detector from the micro- column compared to the maximum beam diameter inside the column, a minimal spot is recorded when the beam leaves the micro-column almost parallel. We estimate the divergence angle of the nearly parallel beam as the ratio of the spot size of the beam in the detector plane and the distance to the micro-column. This is also how the scale bar in Fig. 2.7 (a)-(d) is calibrated, 30 mrad correspond to 2.1 mm on the detector. The divergence angle of the nearly parallel beam and the beam profile characterize the electron optical performance of the column.

Fig. 2.7 illustrates the performance of a micro-column consisting of a micro-lens with 2.5 µm apertures and a mini-lens with 50 µm apertures. During the test series the field emitter is kept aligned at a certain distance in front of the micro-lens. The extraction voltage is set to

-100 V.

The size of the projection image of the beam limiting aperture shown in Fig. 2.7 (a) provides the acceptance angle of the micro-column. Reading out the FWHM of the linescan depicted in Fig. 2.8 (a) results in a full divergence angle of 54 mrad, which corresponds to a distance between tip and beam limiting aperture of 46 µm.

The divergence angle of the beam is reduced when a potential of -40 V is applied to the second micro-lens electrode (see Fig. 2.7 (b)), and as long as the micro-lens alone is in operation, a minimal spot is formed on the detector for a potential of -53 V, as shown in Fig. 2.7 (c). The spot size on the detector can be further reduced, when micro-lens and mini-lens are both in operation. The divergence angle of the beam is first reduced with the micro-lens, and the mini-lens subsequently shapes the beam in the accelerating mode with a potential of $+160$ V on the middle electrode to the spot shown in Fig. 2.7 (d). A linescan through the intensity distribution of the spot and a 3-dimensional representation are shown in Fig. 2.8 (b) and (c). The FWHM of the linescan corresponds to a full divergence angle of 4 mrad.

2.5 Conclusions

Using a gallium ion beam to successively mill apertures through stacks of membrane electrodes allows assembling a dual lens electron optical column featuring micron-sized apertures of high circularity on a well defined optical axis.

Adjusted accordingly, the electron column provides a nearly parallel beam with a residual minimal half divergence angle of 2 mrad. Most notably, the dual lens system allows accelerating and decelerating the electrons within the column by biasing the tip/micro-lens ensemble with respect to the sample potential and adjusting the focusing potential on the mini-lens accordingly. For beam energies above 200 eV, the mini-lens is operated in the retarding mode to avoid potential differences of more than 1 kV between adjacent electrodes. Consequently, for a given focal length electron energies can be selected from a range between a few eV up to more than 1 keV. This aspect again is very beneficial for coherent diffraction imaging applications: a coherent parallel electron beam of tuneable energy allows adjusting the spatial resolution contained in the diffraction record without reconditioning the acceptance angle of the detector unit.

CHAPTER 3

Merging LEEPS and SPM

This chapter describes the merging of LEEPS microscopy and SPM in one dedicated system, with the aim to study freestanding graphene and adsorbates thereon. First, the basic principles of scanning probe microscopy will be introduced and the overall concept of merging the two technologies will be explained. To achieve this goal, major modifications to an old LEEPS microscope have been carried out and the new experimental setup is described. At the end of the chapter some so far unpublished results acquired with this setup are presented. Other results that are in the process of being published are presented in the following two chapters.

3.1 Introduction to Scanning Probe Microscopy

Scanning probe microscopy (SPM) is an umbrella term describing a wide variety of microscopy techniques sharing the concept of scanning a small physical probe across the surface of a sample while measuring a signal of the probe-sample interaction. The scanning tunneling microscope (STM) was invented in 1981 by Binnig and Rohrer at IBM Zurich, and shortly thereafter atomic resolution imaging of a surface was demonstrated for the first time by revealing in real space the 7×7 surface reconstruction of the Si(111) surface [61, 62]. This triggered a tremendous growth of research activity in the field of SPM and the invention of the STM was rewarded a Nobel Prize in 1986. A multitude of SPM techniques has been developed since then, as for example atomic force microscopy or near-field scanning optical microscopy [63,64].

In scanning tunneling microscopy a sharp metal tip is brought in very close proximity to the sample, see Fig. 3.1. Although the electrons in the tip and sample are still separated by a vacuum potential barrier, at a separation d of only a few Ångstroms, the electron wave functions in the tip and sample start to overlap. This allows electron transmission through

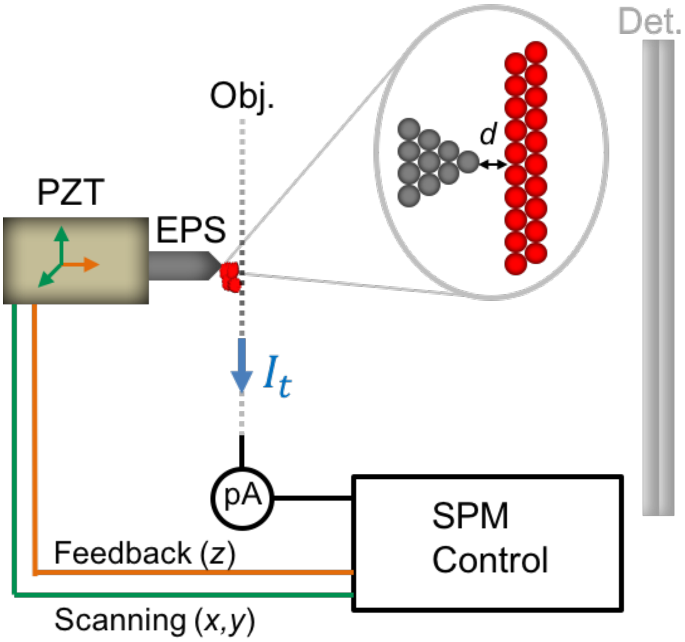

Figure 3.1: Scheme of scanning tunneling microscopy STM . The electron point source **(EPS)** is kept at a moderate bias voltage ($|V_{bias}| < 1$ V) and distance $\boldsymbol{d}$ of few Ångstroms to the grounded sample **(Obj.)**. In this regime, electrons tunnel directly through the potential barrier between the very end of the electron point source tip apex and the sample. The minute tunneling current $\boldsymbol{I_t}$ (in the order of 1 nA) is amplified and used as the feedback parameter by an SPM control system to regulate the tip-to-sample distance d via the z-motion of a piezo tube scanner **(PZT)**. A constant current STM image is generated by scanning the tip laterally in x- and y-direction across the sample and keeping track of the variations in the z-signal.

the potential barrier via the quantum mechanical tunneling effect. A tunneling current I_t starts to flow, when a bias voltage is applied between the tip and sample.

The tunneling current I_t can be approximated [65,66] as:

$$I_t \propto V_{bias} \cdot \rho_s(E_f, d) \cdot e^{-\kappa d}, \tag{3.1}$$

with the bias voltage V_{bias}, the density of states of the sample $\rho_s(E_f, d)$ at the Fermi level E_f and tip position d above the sample. The decay constant κ is described as:

$$\kappa = \sqrt{\frac{2m_e\Phi}{\hbar^2}}, \tag{3.2}$$

where Φ represents the effective local potential barrier height, which is typically in the order of 4 to 5 eV. The decay constant thus amounts to approximately 1 Å^{-1}, which means that a change of the tip-to-sample distance of 1 Å causes a change of nearly one order of magnitude in the tunneling current.

In the scanning tunneling microscope the tip position is usually controlled by a piezo tube scanner which provides motion in x-, y- and z-directions. A SPM control system records the (amplified) tunneling current and provides the voltages to displace the scanner. The tip-to-sample distance d (along the z-direction) is typically adjusted by a feedback loop in order to keep the tunneling current constant, while the tip is scanned over the sample surface in x- and y-directions. The variations in the tip-to-sample distance are then recorded as a function of the scanning position to obtain a so-called constant current STM image. Under the premise that the effective potential barrier Φ does not change, such an image reflects not directly the topography of the sample but rather a surface of constant charge density. Atomic resolution is readily achieved in STM imaging as only the outermost atom of a properly prepared tip is involved in the tunneling process and due to the high z-sensitivity of the tunneling current.

Other kind of scanning probe microscopes employ a field emission current signal instead of a tunneling current signal for feedback control [18, 67]. In such field emission mode SPMs, the tip is kept at a larger (negative) bias voltage and at larger tip-to-sample distance than in STM. The sample is then probed by an electron beam whose diameter depends on the angular spread of the field emitted electrons and the tip-to-sample distance. In such a setup not only the variation in the z-signal can be used to form an image, but also an imaging mode which is conceptually similar to that of scanning electron microscopy is possible: Secondary electrons generated by the impact of the field-emitted electrons are collected by an electron multiplier and the secondary electron yield is recorded as a function of the scanning position. Although limited in resolution compared to STM, such field emission SPM offer different imaging contrast. More recent versions of field emission based SPMs are operated in constant height mode, in which the tip-to-sample distance is not under feedback control. In this so-called near field emission scanning electron microscope (NFESEM), images are generated by keeping track of the variations in the field emission current and the secondary electron yield [68]. Lately, such an NFESEM has been combined with a detector to analyze the energy distribution of the secondary electrons and efforts towards the implementation of a spin-polarization analyzer are made [69].

3.2 Overall Concept of Merging LEEPS Microscopy and SPM

In the course of this PhD project, LEEPS microscopy has been merged with scanning probe microscopy in a single instrument, with the aim to study freestanding graphene and adsorbates thereon with electrons of a large energy range. Both techniques share crucial hardware requirements: (1) An ultra-sharp metal tip, that can be biased with respect to the sample, (2) a positioning device with Ångstrom accuracy and (3) high mechanical stability of the setup.

If the tip is operated in field emission mode, the sample can be probed with electron energies ranging from a few hundred eV all the way down to a few eV before entering the direct tip-to-sample tunneling regime. At a tip-to-sample distance of a few tens of nanometers and more, the microscope is operated in the LEEPS mode, meaning that the sample is probed by a spherical electron wavefront and a projection image is captured at a distant electron detector. Imaging in the LEEPS mode is performed with electron energies ranging from about 20 eV up to a few hundred eV. If the tip-to-sample distance is lowered to a few nanometers only, the field of view for imaging in the LEEPS mode gets extremely small and the magnification becomes excessive.

For such small tip-to-sample distances, the microscope is operated in field emission SPM mode (FESPM), where the current absorbed by the sample is measured and the tip-to-sample distance is regulated by a feedback loop. In an improved FESPM mode termed absorption contrast FESPM (AC-FESPM), additionally the field emission current is recorded, and the relative electron absorption of the sample is used as a contrast signal. Imaging in the FESPM modes is performed with electron energies in the range of 10 eV to 30 eV.

The combined LEEPS microscopy and SPM instrument not only allows imaging of the same sample region subsequently with different high resolution techniques but also benefits from complementary properties of the imaging techniques. LEEPS microscopy is a very fast technique to image a large freestanding sample area – the field of view and magnification can simply be altered by changing the tip-to-sample distance. This allows finding an object of interest rather quickly, and it can then be approached further to make measurements in the SPM mode. No auto-approach procedure to bring the tip in close proximity to the sample is required as in common SPM techniques. Moreover, the feedback control also helps to avoid tip crashes in the LEEPS mode at small tip-to-sample distances. This allowed to measure the transmission through freestanding graphene at very low-electron energies down to 10 eV.

The LEEPS/SPM instrument shall eventually also allow to perform imaging in the STM mode on the freestanding graphene samples, giving access to electron energies below the work function of the sample and possibly atomic resolution. First STM measurements were performed on rigid substrates, but additional improvements of the experimental setup will be needed to study freestanding graphene.

3.3 Experimental Setup

The LEEPS/SPM setup was built on the basis of an old LEEPS microscope. For the new experimental setup the concept of supporting the tip, the sample and the positioning device on a stage (the LEEPS platform) that is transferable as a whole in and out of the vacuum chamber was adopted from the previous design. The LEEPS platform is supported on a damping stage that could be reused from the previous setup. The main challenge to enable SPM imaging was the implementation of a scan head based on a piezo tube scanner for fine positioning of the tip and a suitable SPM control system for scanning signal generating, data acquisition and feedback loop control. Moreover, the LEEPS detector system and the pumping scheme to establish vacuum conditions were rebuilt and the mechanical stability was improved.

3.3.1 LEEPS platform

The heart of the microscope is the LEEPS platform containing the field emission electron source and the sample, together with a dedicated piezo positioner system for the accurate positioning of the source with respect to the sample, see Fig. 3.2. During the operation of the microscope, the LEEPS platform is supported by a damping stage inside the main chamber of the vacuum system to decouple it from external mechanical vibrations. For the exchange of the tip or the sample, the whole LEEPS platform can be lifted from the damping stage with a linear transfer stick and brought into the transfer chamber. After venting of the transfer chamber, the flange with the transfer stick is opened and the LEEPS platform can be placed at a test stage for convenient handling.

The two main components of the LEEPS platform are the tip tower and the sample tower. The tip is mounted to a piezo tube scanning head for the fine positioning, on top of a z-direction linear piezo motor (C_z) enabling the coarse regulation of the tip-to-sample distance. The sample is placed in a sample holder on top of a stack made up from two individual x- and y-direction linear piezo motors (C_x and C_y). All wires for the electrical connections to the piezo-elements, tip and sample are gathered at three plug connectors on the side of the LEEPS platform base plate. When the LEEPS platform is positioned in the main chamber, the plug connectors make contact with their counterparts on the damping stage.

Coarse positioning

Three individual linear piezo motors are used for the coarse positioning of the tip to the sample. We use commercially available stick-slip type motors with piezo-electric actuators

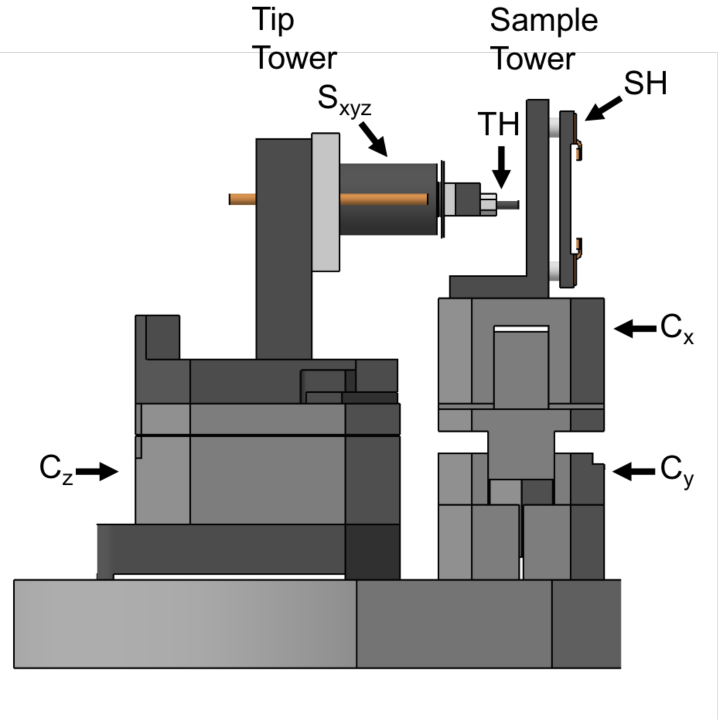

Figure 3.2: CAD rendering depicting the most relevant elements of the LEEPS platform. The tip tower is built up by a piezo motor for coarse positioning in z-direction **(C_z)**, the scanning head for the fine positioning in x-, y- and z-direction **(S_{xyz})** and the tip holder **(TH)** to carry the electron point source. The sample tower consists of a piezo motor for coarse positioning in y-direction **(C_y)**, a piezo motor for coarse positioning in x-direction **(C_x)** and the sample holder **(SH)**.

from the company Attocube[1]. The model ANPx101 is used to drive the tip in z-direction (C_z), the models ANPx50 (C_x) and ANPz51 (C_y) are used to move the sample in x- and y-direction.

The working principle of an Attocube motor is shown in Fig. 3.3. The motor is moved in stepping mode by applying a sawtooth shaped voltage pulse to the piezo-electric actuator. The piezo-electric actuator expands during the slow pulse rise time. The clamped table moves accordingly due to the friction between the table and the guiding rod (stick phase of the process). The sudden drop of the voltage is associated with a rapid contraction of the piezo-electric actuator. Due to the moment of inertia of the clamped table the friction is overcome in this rapid process, and the table sits nearly still (slip phase of the process). In this stick-slip process, the table moved one step forward. To move the table in the backward direction, the sawtooth pulse is reversed, meaning the voltage is suddenly increased and slowly ramped

---

[1] Attocube Systems AG, www.attocube.com.

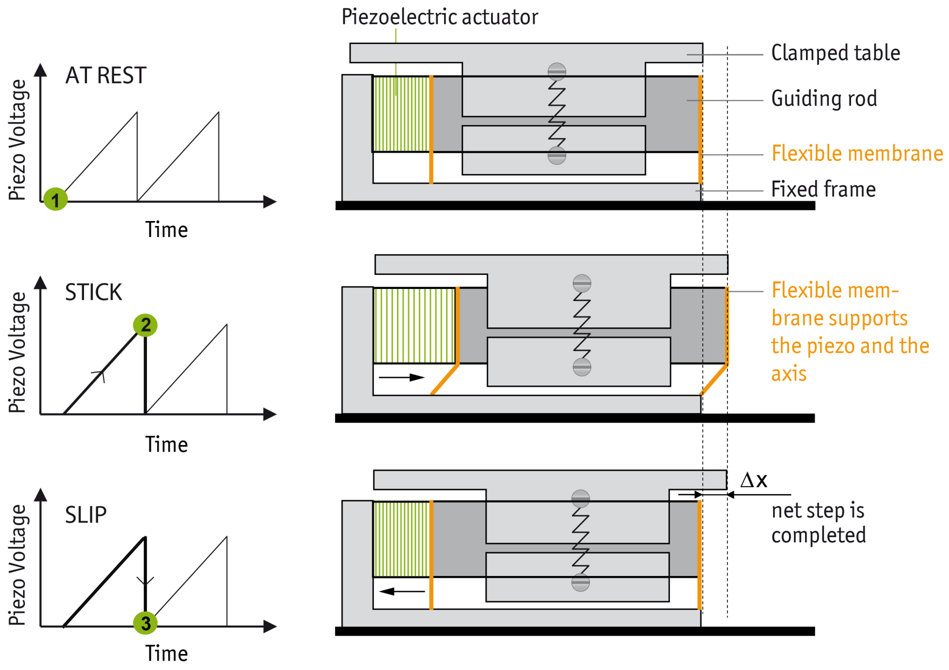

Figure 3.3: Working principle of the Attocube motors. The figure is reprinted with the permission from Attocube systems AG.

down afterwards.

The Attocube motors are made from non-magnetic components. This is crucial for the proper operation of the LEEPS microscope, because due to the low energy of the electrons even small magnetic stray fields distort the well-defined wavefront needed for successful reconstruction of in-line holograms [70].

Fine positioning

For the fine positioning of the tip a scan head based on a piezo electric tube was designed and implemented. The main challenges in the design of the scan head were the need to withstand high bias voltages of up to 3 kV applied to the tip and allowing resistive heating of the tip with currents up to 2 A, while keeping the design compact to fit the limited space on the LEEPS platform. All metal parts are made from titanium to keep the mass as small as possible. The insulating parts are made from Macor [2], a machinable ceramic, to ensure high vacuum compatibility.

The most important part of the scan head is a hollow tube of a piezo-electric material with radial polarization. The tube features gold plated electrodes on the inside and the outside.

---

[2] Corning Inc., www.corning.com.

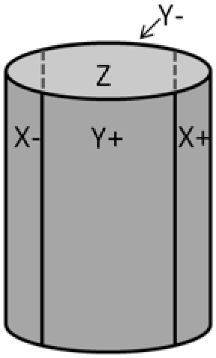

Figure 3.4: Working principle of the piezo tube scanner. The tube is elongated or contracted by changing the bias on the inner electrode **(Z)**. A voltage of equal magnitude but opposite sign is applied to opposite electrodes on the outside of the tube for lateral deflection (e.g. electrodes **(X+)**, **(X-)** for deflection in x-direction).

While the inner electrode is continuous, the electrode on the outside is axially divided into four equally sized segments, denoted with X+, X−, Y+, Y−in Fig. 3.4. For the lateral displacement of the tube an equal but opposite voltage is applied on opposite segments of the outer electrode (e.g. on segments X+, X−for movement in x-direction). To contract or expand the tube along the axial direction, a negative respectively positive potential is applied to the inner electrode, denoted with Z in Fig. 3.4. The piezo tube employed here is of the type EBL #2 from EBL Products Inc.[3], the total length of the tube is 10 mm and the electrodes are removed from both ends at a length of 0.5 mm. The outer diameter is 3.2 mm and the tube thickness is 0.5 mm.

A cross-sectional view of the scan head is shown in Fig. 3.5. The piezo tube is glued on the Macor base plate using electrically insulating vacuum compatible epoxy[4]. The voltages applied to the tube can be as high as 400 V. Thus, to avoid electric stray fields which could distort the electron wave in LEEPS imaging, the tube has to be electrically shielded. The first part of the shielding is a tube made from titanium placed around the piezo tube. The second part of the shielding is a disk attached to the front of the piezo tube. The shielding tube and disk are both held at ground potential.

Two titanium blocks separated from the shielding disk by a Macor spacer constitute the tip receiver. The pins on the piezo tube side of the tip holder are inserted into two bores in the tip receiver, and secured by screws inside threaded holes oriented perpendicular to the bores. The Z-electrode of the piezo tube is connected by a wire running through a hole in the

---

[3] *EBL #2*, EBL Products Inc., www.eblproducts.com.

[4] *EPO-TEK H70E-2*, Epoxy Technology Inc., www.epotek.com.

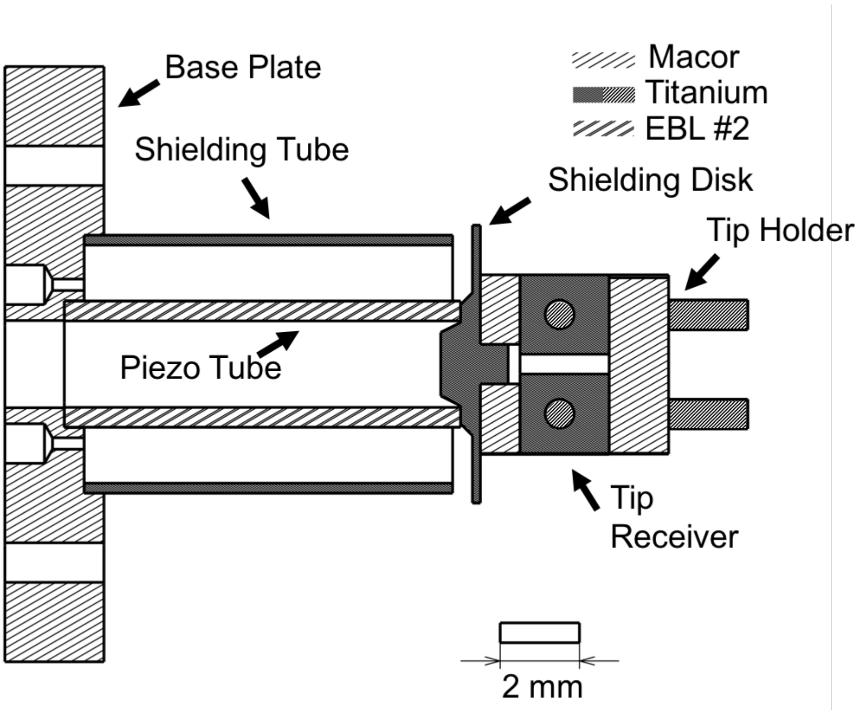

Figure 3.5: Cross-sectional view of the scanning head

middle of the Macor base plate, the outer electrodes are connected with wires going through four small holes in the base plate between the piezo tube and the shielding tube. Electrically conductive vacuum compatible epoxy[5] is used to connect the wires and the electrodes.

The lateral displacement of the scanner (x- and y-direction) was calibrated by scanning in the LEEPS mode across a structure of known size, which was fabricated in a freestanding Pd coated SiN membrane by focused ion beam milling. The axial displacement (z-direction) was calibrated by comparison against the scan range of the coarse z-direction Attocube motor. The displacement per voltage of the tip is calibrated to 31.5 ± 3.0 nm/V for the x- and y-direction and to 4.0 ± 0.6 nm/V along the z-direction.

Sample holder

The sample holder features copper springs to keep the sample plate fixed once it is put in place. This helps to make fast transfer of the graphene samples in order to keep them clean. The holder is fixed to the sample tower with Macor spacers to ensure electrical insulation. The sample holder is electrically connected with a coaxial cable to allow low noise measurements

---

[5] *EPO-TEK H20E*, Epoxy Technology Inc., www.epotek.com.

of the current absorbed by the sample.

3.3.2 Vibration Isolation

To acquire high quality data both with LEEPS microscopy and SPM techniques it is necessary to avoid any uncontrolled relative motion between the tip and the sample. Such uncontrolled motion can be provoked by mechanical vibrations from the laboratory environment coupling to the microscope through the floor or through acoustic waves. It is therefore essential to effectively damp the transmission of such mechanical vibrations to the LEEPS platform.

An effective approach is the use of multiple isolation stages [71,72]. This allows for the suppression of the resonance of one stage by the others, and as a consequence the suppression of vibration transmission over a large frequency range. The LEEPS/SPM microscope is located in a laboratory building that was specifically built for noise-sensitive experiments. The lab provides working spaces on a massive concrete block immersed in a sand basin. The microscope is furthermore placed on an air-damped workstation. These two measures efficiently suppress the transmission of low-frequency vibrations coupling to the microscope through the floor.

A damping stage inside the vacuum chamber is used for the suppression of the remaining vibrations, namely higher frequency vibrations not efficiently blocked by the air-damping and vibrations coupling to the microscope acoustically through the air. The damping stage consists of five platforms separated by damping elements: metal springs of different length between the lowest three platforms and small pieces of Viton[6] between the topmost three platforms. A pendulum weight is attached to the topmost platform providing an increased mass to the LEEPS platform and effectively lowering its centre of gravity. Such construction provides an effective damping over a large frequency range.

To avoid the transmission of vibrational noise through the wire connections, all wires running to the LEEPS platform are clamped at least 3 times between Viton pieces attached to the damping stage. Additional Viton damping stages are located on the LEEPS platform itself. Furthermore, the wires were carefully chosen as thin as possible regarding wire and isolation thickness.

3.3.3 Vacuum System

The LEEPS/SPM microscope is hosted in a vacuum chamber which is divided into two parts by a plate valve – the transfer and the main chamber. A scheme how the two chambers are pumped to establish high vacuum conditions is shown in Fig. 3.6. The chamber is pumped

---

[6] *Viton*, The Chemours Company, www.chemours.com.

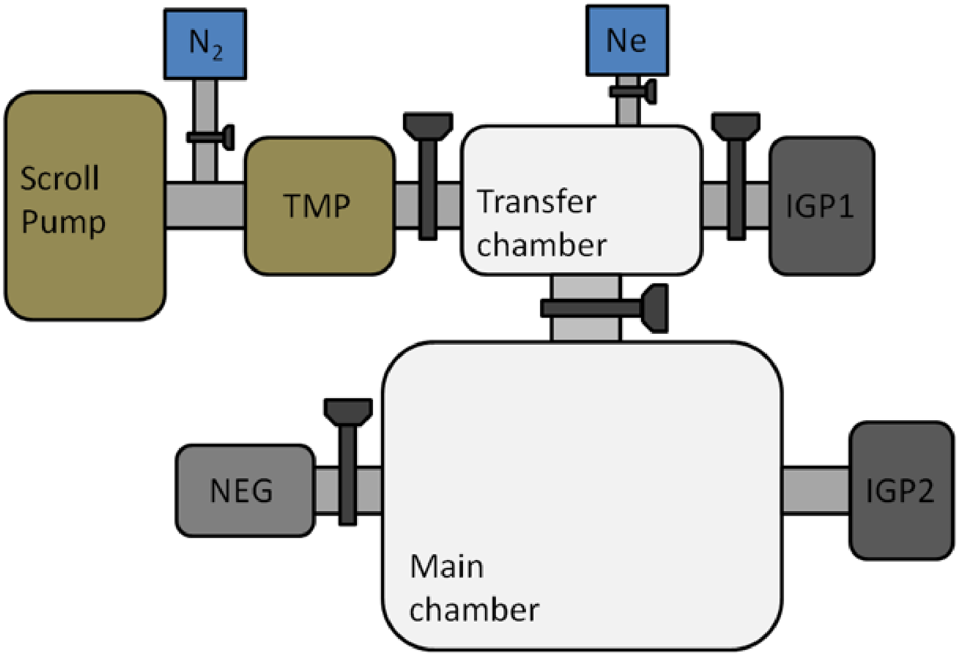

Figure 3.6: Scheme of the vacuum system.

by a scroll pump and a turbo molecular pump (TMP) connected to the transfer chamber to a pressure of about 1×10^{-7} mbar. The transfer chamber is additionally connected to an ion getter pump (IGP1). The main chamber contains all important parts needed for the experiments, as the LEEPS platform and the detector. An ion getter pump (IGP2) and a non-evaporable getter pump (NEG) are connected to the main chamber. After bake-out of the system and with the plate valve between the two chamber closed a pressure down to 1×10^{-9} mbar is reached in the main chamber.

To allow for an easy and efficient bake-out of the microscope a bake-out tent was implemented in the course of the PhD project. The tent is heated by a heater fan and the temperature is controlled using a PID-controller. The bake-out temperature is limited to 120° Celsius – the maximum temperature specified for the electron detector.

To transfer a sample, the LEEPS platform is placed in the transfer chamber with the help of a linear transfer stick, and the plate valves to the main chamber and the first ion getter pump (IGP1) are closed. The transfer chamber is then vented with dry nitrogen introduced on the low vacuum side of the turbo molecular pump and the flange with the linear transfer stick is opened. The LEEPS platform is lifted and the sample plate is pushed into the springs of the sample holder with the help of tweezers. The flange is closed again as fast as possible and the transfer chamber is pumped by the scroll pump and turbo molecular pump subsequently. As soon as a pressure of 1×10^{-5} mbar is reached, the valve to the first ion getter pump (IGP1) is opened, which lowers the pressure to about 1×10^{-6} mbar within one minute. Then the valve between transfer chamber and main chamber is opened and the LEEPS platform is placed on the damping stage. After closing the valve between the two chambers, the valve to the NEG pump is opened. To keep graphene samples clean, they should only be studied with LEEPS microscopy after a pressure below 2×10^{-8} mbar is reached, as an increased adsorption of contaminants from the rest gas under low-energy electron exposure was observed at higher pressure. A frequent bake-out of the system is needed, as the minimal achievable pressure increases every time a sample is transferred, as the LEEPS platform is exposed to air for a short time.

3.3.4 Preparation of Graphene Samples

The freestanding graphene samples were prepared using the platinum-metal catalysis method [45]. Commercially available graphene grown by chemical vapor deposition (CVD) on a polycrystalline copper substrate[7] is covered by a polymethyl methacrylate (PMMA) layer of about 100 nm in thickness using a spin coater. A flake of about 2×2 mm^2 in size is deposited with the copper side facing down on the surface of a ferric chloride (Fe_2Cl_3) solution to etch away the copper substrate. The remaining PMMA covered graphene flake is rinsed several times with ultra highly purified water (uhp-H_2O) to wash off the etching solution before it is transferred to a dedicated sample substrate.

The sample substrate is made from commercially available 100 nm thick silicon nitride membranes covering a 250×250 µm^2 window in a 100 µm thick silicon chip. Using a focused ion beam an array of holes of typically 200 nm up to 2 µm in diameter is milled through the silicon nitride membrane, which was previously sputter coated with a 25 nm thick palladium layer. After milling, the chip is sputter coated again from both sides to prevent charging during low-energy electrons exposure.

After the picking up of the PMMA covered graphene flake, the chip is fixed on a sample plate by a metal spring. The sample is then heated on a conventional laboratory heating plate to a temperature of 300 to 350° Celsius which leads to a complete removal of the PMMA layer. While still hot, the sample is transferred as fast as possible into the vacuum system to avoid contamination by air exposure.

The freestanding graphene samples feature mostly single-layer graphene, but also regions of multi-layer graphene are present. Individual adsorbates and nanometer-sized clusters of adsorbates are occasionally observed between ultra-clean regions. The adsorbates, most likely stemming from contamination, are observed to aggregate on domain boundaries or the edge between graphene layers of different thickness.

---

[7] *Graphene on copper foil*, ACS Material LLC, www.acsmaterial.com.

3.3.5 Preparation of Field Emission Tips

Etching

To be used as the electron point source in the LEEPS/SPM setup, ultra sharp tungsten tips are fabricated by electrochemical etching in a NaOH electrolyte: A tungsten wire is partially immersed into the electrolyte and the surface tension of the solution causes a meniscus around the wire. Tungsten atoms from the wire are oxidized and dissolve as a positive voltage is applied to the wire with respect to a counter electrode immersed in the solution. The etching is the most effective in the meniscus which leads to a cusp shaped thinning of the wire. This wire necking mechanism can be understood by complex surface and bulk effects [73–76]. Finally, the wire breaks when it becomes too thin to hold the weight of the lower part. The accompanied drop in the etching current is detected in the electronic circuit of the power supply which then immediately shuts off the voltage output to stop the etching procedure.

W(111) wires with a diameter of 0.1 mm are used as the starting material for the tip fabrication. A 20 % aqueous sodium hydroxide (NaOH) solution is used as the etchant and a DC voltage of 10 V. A piece of the tungsten wire with a length of about 5 mm is spot welded to a loop across the two pins of the tip holder and afterwards cleaned by rinsing with acetone and uhp-H_2O. The tip is immersed with about 3 mm into the solution and quickly polished by turning on the etching voltage for only a few seconds. This is done to remove the oxidized layer on the wire surface and afterwards the wire is cleaned once again with uhp-H_2O. Subsequently, the wire is dipped into the solution about 0.3 mm deep and the etching process is started again until the wire breaks. This results in tip apex diameters of typically 50 nm down to 20 nm.

After the etching procedure the tip is cleaned once again using acetone and uhp-H_2O and then inspected under an optical microscope. If it shows the desired conical shape of a well etched tip, the tip holder is inserted into the tip receiver on the LEEPS platform and secured with screws.

The LEEPS platform is transferred into the main chamber and once a good vacuum pressure is established, the tip is resistively heated by passing a current through the loop in order to clean it from any remaining adsorbates or oxide layers. A tip that is well etched should show field emission with a current of 50 nA at a bias voltage of -300 to -400 V when fully retracted by the coarse piezo motor to an approximate distance of 4 mm from the sample.

Sputtering

An in-situ neon self sputtering procedure can be applied to further reduce the apex diameter of a freshly prepared tip or to re-sharpen a tip that got blunt from excessive heating [77,78].

Before the procedure is started the valves in front of the NEG pump and the transfer chamber ion getter pump are closed and the ion getter pump of the main chamber is turned off. The valve separating the two chambers is opened – the vacuum system is now pumped by the turbo molecular pump and scroll pump solely. Neon with a purity of 99.999% is inserted through a leak valve attached to the transfer chamber (see Fig. 3.6) until a stable pressure of 3×10^{-4} mbar is established. The tip is connected to a power supply operated in constant current mode and the negative bias voltage is slowly increased until the set current of 10 µA is drawn from the tip. Neon atoms are ionized by collision with field emitted electrons. The ions are then accelerated towards the tip apex and knock out tungsten atoms. Due to their higher mass, the neon ions do not follow the same trajectory as the field emitted electrons, but hit the tip at a larger distance from the centre of the apex. This leads to a gradual reduction of tip radius down to about 10 nm.

In the beginning of the sputtering procedure the tip should typically start to emit at a bias voltage between -1 to -2 kV. The cables can support a maximum voltage of 3 kV and if the tip does not start to emit at such a bias, it has to be replaced by a newly etched one. During the neon sputtering procedure the voltage on the power supply decreases with increasing tip sharpness as the power supply is operated in constant current mode. Once a stable minimum of the voltage is reached, the power supply is turned off. The tip is afterwards gently annealed to heal out any possible defects from the neon bombardment.

After a successful neon sputtering procedure the tip typically emits a current of 50 nA at a bias voltage of -200 to -250 V when fully retracted. If this is not the case, the tip is blunted by resistive heating to about 2000 K and the neon sputter procedure needs to be repeated.

3.3.6 SPM Control System and Electronics

In this section the crucial electronic hardware components and the software to operate the microscope in the SPM mode are described. The SPM control system is based on a SPM controller which works on the basis of ± 10 V input and output signals, and runs all important tasks like data acquisition, scanning signal generation and feedback loop operation in real time. An open source SPM software is used to control the SPM controller and for data processing and visualization. To make the SPM current signals which are typically in the order of one nA accessible to the controller, they are amplified and converted to voltage signals by dedicated current-to-voltage amplifiers. The output signals of the controller are amplified by a low-noise high voltage amplifier to reach the necessary voltages to drive the piezo tube scanner. A scheme of the SPM control system is shown in Fig. 3.7.

High voltage amplifiers for coarse and fine positioning

To control the coarse piezo motors the controller "ANC 150" from Attocube is used, providing individual output channels for each of the three axes. It generates the sawtooth voltage pulses necessary to drive the motors. The amplitude and frequency of the sawtooth pulses are set manually and the output is controlled for either a single step or a continuous series of steps. Unfortunately, the ANC 150 is a source of serious electrical noise which translates into a physical shacking of the tip with respect to the sample. For this reason, the connections to the Attocube coarse piezo motors have to be grounded during LEEPS or SPM measurements.

The piezo tube scanner is driven by the high voltage amplifier "Smart Piezo Drive, Model MK3-HV1" from SoftdB[8], which amplifies the ± 10 V control signals from the SPM controller. This low noise (≤ 120 $\mathrm{V_{rms}}$) and low drift high voltage amplifier features three channels (for x-, y-, and z-direction) with three independent main signal inputs of variable gain (1x, 2x, 5x, 10x, 20x) and adjustable bandwidth (1 kHz, 10 kHz, 50 kHz) and three auxiliary inputs of fixed gain (1x) and bandwidth (50 kHz). Every channel has one output for the amplified signals ($X+, Y+, Z+$) and one output for the inverted and amplified signals ($X-, Y-, Z-$) with maximum output voltages of ± 200 V. The $X+/X-$ and the $Y+/Y-$ output signals are used for the lateral motion of the piezo tube scanner and the $Z+$ output is used for its longitudinal expansion and contraction.

The Smart Piezo Drive features a USB link to connect to a PC and a software control interface to set various parameters like gain, bandwidth etc. and to monitor the output voltage history on all channels. The Smart Piezo Drive software interface moreover allows to set an offset voltage (O_x, O_y, O_z) to any of the channels. This function is used to position the tip during the LEEPS mode operation of our microscope and if large offsets in the SPM mode are desired.

Current-to-voltage amplifiers

As current-to-voltage amplifier (IV1) to measure the sample current, the commercially available model "DLPCA-200"[9] is used. The amplifier converts the current input signal to a ± 10 V output signal, which can then be read by the SPM controller. For STM measurements, a gain of 10^9 V/A is used, corresponding to a current measurement range of ± 10 nA and for measurements in field emission mode a gain of 10^8 V/A is used, corresponding to a current measurement range of ± 100 nA.

First STM and FESPM experiments have been performed with the sample current-to-voltage amplifier (IV1) alone. Later on, a second current-to-voltage amplifier (IV2) was installed to simultaneously measure the tip current as well. This amplifier was developed and built by

---

[8] *Smart Piezo Drive Model Mk3-HV1*, SoftdB, www.softdb.com.

[9] '*Variable Gain Low Noise Current Amplifier DLPCA-200*, FEMTO Messtechnik GmbH, www.femto.de.

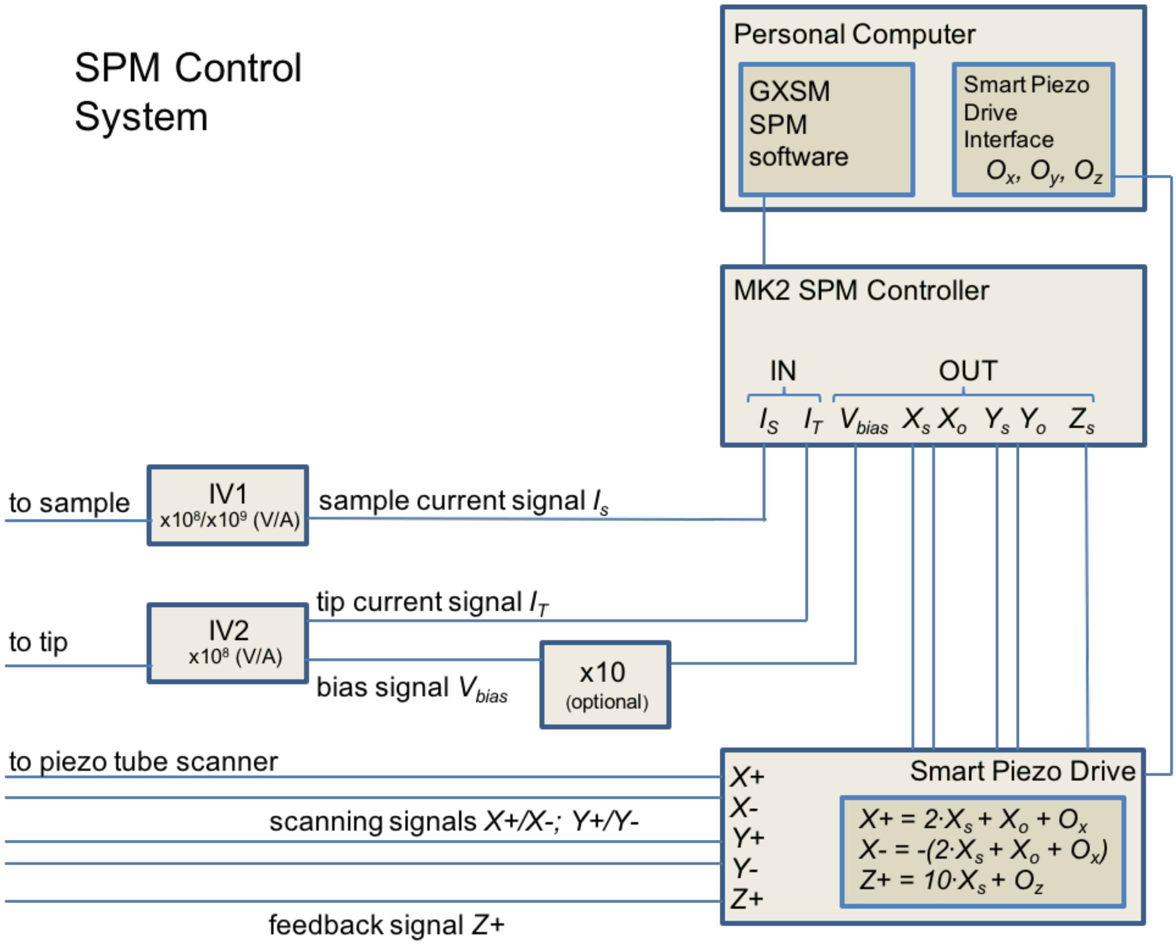

Figure 3.7: Scheme of the SPM control system.

Thomas Bähler, technical assistant in the group of Professor Danilo Pescia at the ETH Zurich. The amplifier is based on the use of linear optocouplers for galvanic isolation of the current signal line. The bias voltage on the signal line is defined by a voltage input signal either directly taken from the ± 10 V bias output of the SPM controller for STM measurements, or first amplified by an analog voltage amplifier with a gain of 10x for measurements in field emission mode. The measured current is amplified with a gain of 10^8 V/A to a ± 5 V output signal, corresponding to a current measurement range of ± 50 nA.

SPM control system

SPM functionality was implemented on the basis of the open source software package GXSM [79–81] and a dedicated, commercially available SPM controller from SoftdB[10]. The digital

---

[10] *Signal Ranger MK2 with Analog810 module*, SoftdB, www.softdb.com.

signal processor board (DSP) "Signal Ranger MK2-A810" of the SPM controller runs all the real time tasks like data acquisition, scanning signal generation and feedback loop operation. The controller provides a digital-to-analog (DAC) and analog-to-digital (ADC) conversion to interface the analog hardware and a USB 2.0 interface to connect to a Linux based PC.

Parameters like scanning range, offsets, scanning speed, the factors for the proportional and integral part of the feedback loop, set current and bias voltage are set in the graphical user interface of GXSM prior to a SPM measurement. The scanning output signals X_s and Y_s from the MK2-A810 are fed to the main inputs of the Smart Piezo Drive, and typically a gain g of 2x and a bandwidth of 10 kHz is chosen. This corresponds to a maximum directly accessible scan range of 1.26×1.26 µm^2. A small offset up to 630 nm in x- and y-direction is provided by the offset signal outputs X_o and Y_o of the MK2-A810, which is connected to the auxiliary inputs (gain 1x) of the Smart Piezo Drive. To access larger offsets, the Smart Piezo Drive software interface is used, allowing to access the full scan range of 12.6×12.6 µm^2 of the piezo tube scanner. The scanning signals are amplified by the Smart Piezo Drive and sent to the piezo tube scanner as $X+ = g \cdot X_s + X_o + O_x$ and $X- = -X+$, and accordingly for $Y+$ and $Y-$.

The bias output signal V_{bias} ranging from -10 to $+10$ V is either directly connected to the tip current-to-voltage amplifier (IV2) bias input for STM measurements or first amplified with a gain of 10x for field emission mode operation.

The output signals of the current-to-voltage amplifiers I_T and I_S (in volt) are acquired by the MK2-A810. It is possible to chose either of the two signals to be processed by the feedback loop. Usually a logarithmic transform is applied to the signal and the z-signal adjustment is then calculated by a proportional integral feedback algorithm.

The z-signal output Z_s from the MK2-A810 is usually amplified with a gain of 10x by the Smart Piezo Drive, which correspond to a z-range of 800 nm of the piezo tube scanner. The signal $Z+$ sent to the piezo tube scanner is then given by $Z+ = 10 \cdot Z_s + O_z$. The offset signal O_z controlled by the Smart Piezo Drive software interface is used to access the full z-scan range of 1.2 µm and to adjust the tip height if the feedback is turned off, for example in order to acquire images in the LEEPS mode.

SPM images are generated in GXSM from the current signals and z-signal data received by the MK2-A810. Post-processing of the SPM data like image correction or pixel-wise calculation of the relative absorption are done with the open-source software Gwyddion[11].

---

[11] Gwyddion, www.gwyddion.net.

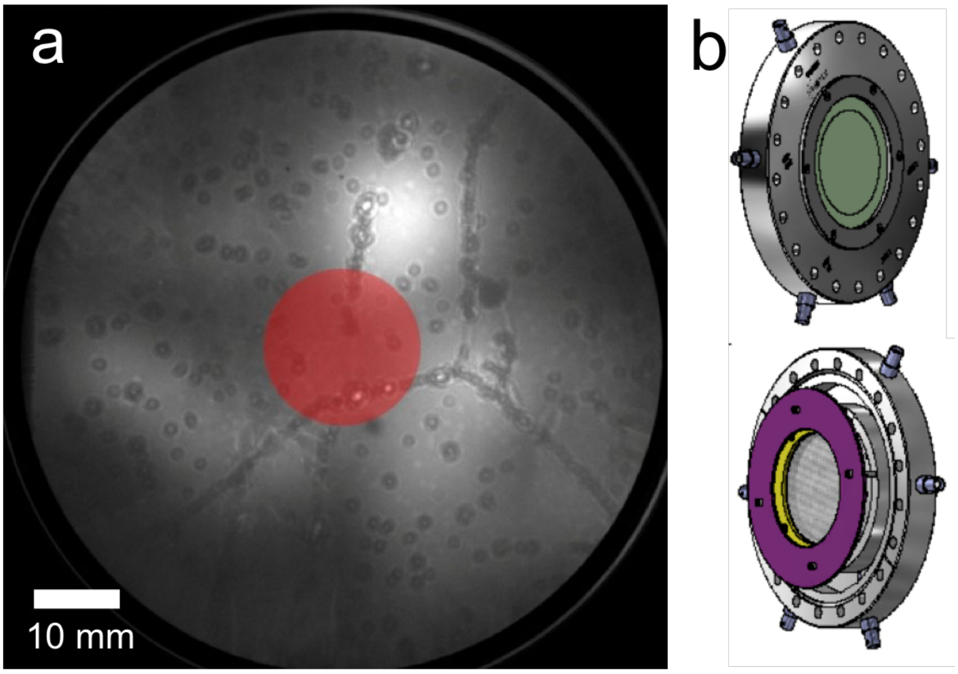

Figure 3.8: (a) LEEPS micrograph of a freestanding graphene sheet with adsorbates recorded with the new detector system at an electron energy of 90 eV and a source-to-sample distance of about 700 nm. The increase of the numerical aperture is apparent when compared to the previous detector design whose acceptance angle is illustrated by the red disk. **(b)** Illustration of the detector "model VID175/P43/GL". Top: View from the air side. Bottom: View from the vacuum side.

3.3.7 LEEPS Image Detector

During the course of this thesis a new high-resolution spatial electron detector has been implemented[12]. The detector is based on a micro-channel plate (MCP) with channel pores of 10 micrometer in diameter and a sensitive detector area of 75 mm in diameter. The individual channels of the MCP serve as electron multipliers. An electron impinging on a channel leads to the generation of multiple secondary electrons, which are subsequently accelerated in an electric field created by applying a potential difference of typically 1 kV between the metal plated front and back side of the MCP. The accelerated secondary electrons hit the channel wall multiple times, releasing more and more secondary electrons every time. This avalanche-like effect leads to a multiplication of the electrons with a gain in the order of 10^5. Behind the MCP the electrons are accelerated towards a phosphorous coated screen to a landing energy

---

[12] *Model VID175/P43/GL*, Photek Limited, www.photek.co.uk.

of 5 keV. The high energy electrons lead to the excitation of the electroluminescent coating, converting the electronic signal to an optical signal, which is thereafter detected with a digital camera.

The large detector size of 75 mm in diameter combined with a short source to detector distance of 47 mm, leads to a great enhancement of the acceptance angle compared to the previous detector design (see Fig. 3.8 (a)). The high numerical aperture of $NA = 0.62$ corresponds to an attainable resolution of 1 Ångstrom for 100 eV electrons, on the supposition of coherent emission from the electron source over the full acceptance angle covered by the detector.

3.4 Results

In this section, the scanning probe microscopy functionality of the new setup is demonstrated by field emission based SPM on freestanding graphene samples (FESPM and AC-FESPM). Moreover, a procedure to sharpen field emission tips is presented, which allows to record ultra-low energy electron holograms. Preliminary STM measurements are shown at the end of the section.

3.4.1 Field Emission SPM

The functionality of the FESPM mode could be demonstrated by stable imaging of freestanding graphene and adsorbates thereon. In this measurement mode the tip is kept at a distance of a few nanometers to the sample and a bias voltage V_{bias} in the order of -10 to -30 V is used (see Fig. 3.9). The electrons do not directly tunnel between tip and sample but are field emitted from the tip into vacuum towards the sample. The sample is thus probed by a beam of low-energy electrons, whose spot size depends on the angular spread of the field emitted electrons and the tip-to-sample distance. Some part of the field-emitted electrons is absorbed by the sample and detected as the sample current (absorption current I_A) by the current amplifier. The experiments presented in this subsection were carried out before the current-to-voltage amplifier (IV2) to measure the tip current I_E was installed and thus only the sample current I_A could be measured.

The distance between the tip and the sample is regulated by the feedback loop for a constant absorption current I_A. The variation in the tip-to-sample distance (z-signal) is plotted as a function of the x- and y-coordinates of a scan across the sample to generate a FESPM image. As the adsorbates on the freestanding graphene exhibit a comparably larger relative absorption than the graphene itself, the tip is retracted above the adsorbates to a larger height in order to reduce the emission current for maintaining I_A constant. The z-signal image thus does not simply represent the topography of the sample but rather depends on the

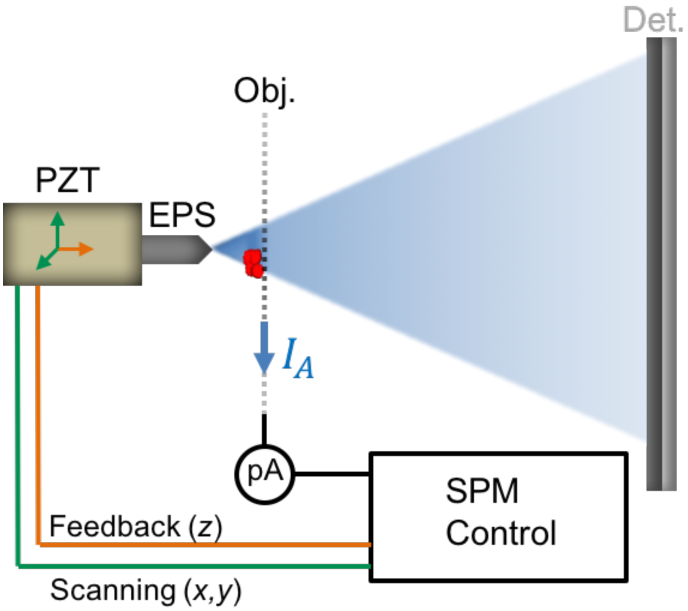

Figure 3.9: Scheme of field emission scanning probe microscopy FESPM. A divergent beam of low-energy electrons is emitted by an electron point source **(EPS)**. Part of the beam is absorbed by the sample **(Obj.)** and measured as the absorption current $\boldsymbol{I_A}$. An SPM control system generates the scanning signals to drive a piezo tube scanner **(PZT)** in order to scan the tip across the sample surface. The source-to-sample distance is feedback-controlled to maintain the absorption current I_A constant. FESPM images are generated by plotting the variations in the source-to-sample distance (z-signal) and the absorption current I_A as a function of x- and y-coordinates of the scan.

topography and the variation of the relative absorption characteristics of the sample. The lateral resolution in the FESPM image is mainly given by the spot size of the field emission electron beam on the sample, and thus depends on the tip-to-sample distance and the angular spread of the beam.

Prior to FESPM measurements the sample region of interest is chosen by imaging the sample in the LEEPS mode. A low-energy electron hologram of clusters of aggregated adsorbates and its reconstruction is shown in Fig. 3.10 (a) and (d). A raw data FESPM images recorded after the hologram acquisition on the same sample region with a bias voltage of $V_{bias} = -14$ V and a set current of $I_A = 1$ nA is shown in Fig. 3.10 (b). Temporal instability of the field emission leads to frequent jumps in the z-signal. The instability is most likely caused by adsorbate diffusion across the tip apex, leading to sudden changes in the local work function of the tip. For better visibility of the significant features, the image is corrected by adjusting the average

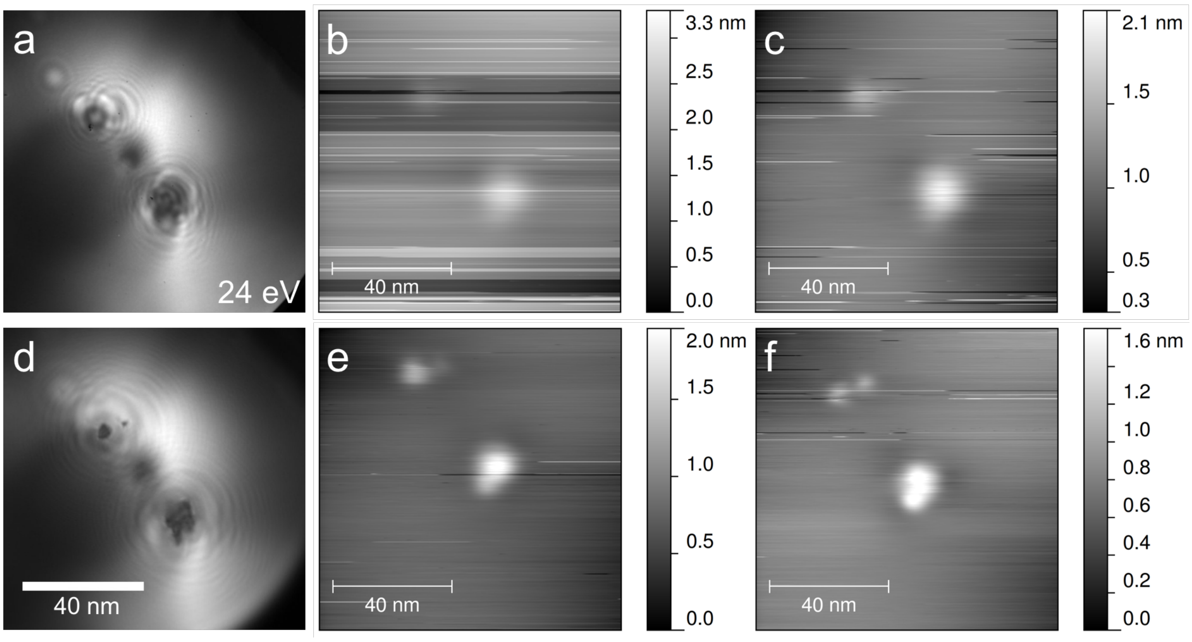

Figure 3.10: LEEPS and FESPM imaging of clusters on freestanding graphene. All FESPM images were recorded with a set current of $I_A = 1$ nA and a scan area of 100×100 nm^2. **(a)** Hologram recorded in LEEPS mode with an electron energy of 24 eV. **(b)** Raw data z-signal FESPM image recorded with a bias voltage of $V_{bias} = -14$ V. Jumps in the z-signal due to unstable field emission are apparent. **(c)** The same data as shown in (b) after correcting for the unstable field emission by adjusting the average z-signal of every scan line to the same level. The jumps are now apparent as black or white horizontal stripes. **(d)** Reconstruction of the hologram shown in (a). **(e)** Corrected z-signal FESPM image recorded at a bias of $V_{bias} = -12$ V. **(f)** Corrected z-signal FESPM image recorded at a bias of $V_{bias} = -11$ V. The two clusters in the top left corner are well resolved as separate features.

z-signal of every scan line to the same level. The resulting image is shown in Fig. 3.10 (c). The individual current jumps due to field emission instability are now distinguishable as horizontal stripes or scars in the image. Corrected FESPM images recorded at lower bias voltages are shown in Fig. 3.10 (e) and (f). An increase of the lateral resolution for lower bias voltage is apparent, as a consequence of the reduction of the overall tip-to-sample distance. In Fig. 3.10 (f), the two clusters in the top left corner of the image are well resolved as separate features in the FESPM image.

If the feedback control is set to operate rather slowly while a rather fast lateral scanning speed is chosen, the tip height is not adjusted fast enough to maintain a constant absorption current. These variations in the absorption current I_A can be used as an additional image channel, as

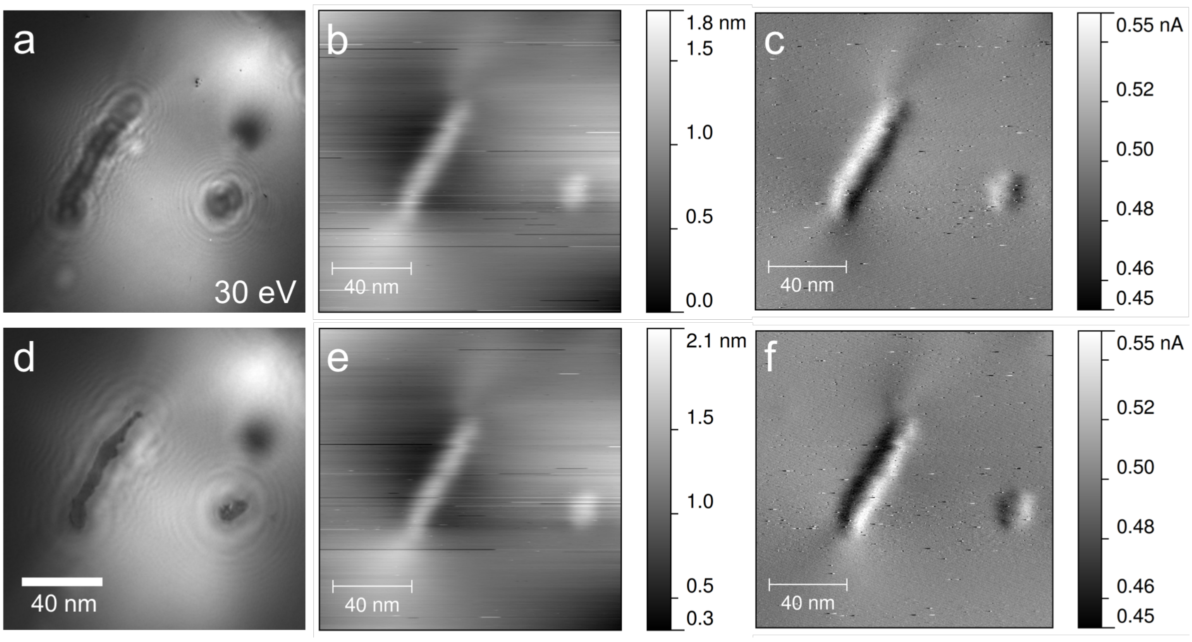

Figure 3.11: LEEPS and FESPM imaging of clusters on freestanding graphene. The FESPM images were recorded with a rather slow feedback control and a set current of $I_A = 0.5$ nA. The scan area is 150×150 nm^2. **(a)** Hologram recorded in LEEPS mode with an electron energy of 30 eV. **(b)** and **(c)** FESPM images recorded with the scan direction from left to right and a bias voltage of $V_{bias} = -14$ V. In (b) the z-signal image is shown and in (c) the absorption current I_A-signal image is shown. **(d)** Reconstruction of the hologram shown in (a). **(e)** and **(f)** FESPM images recorded with the scan direction from right to left and a bias voltage of $V_{bias} = -14$ V. In (e) the z-signal image is shown and in (f) the absorption current I_A-signal image is shown.

shown in Fig. 3.11. When the tip is scanned from left to right across some adsorbate, first an increased absorption current is detected as the tip is not retracted fast enough to keep the current constant, see Fig. 3.11 (c). As the tip does not approach the freestanding graphene fast enough behind the adsorbate, a decreased absorption current is measured. If the scanning direction is from right to left, the contrast in the absorption current is inverted, as illustrated in Fig. 3.11 (f).

3.4.2 Absorption Contrast Field Emission SPM

The implementation of the I-V amplifier (IV2) to measure the emission current I_E emitted by the tip gives access to another signal that can be used as an input for the feedback control and as a contrast mechanism for the imaging. This enables an improved FESPM mode, where the

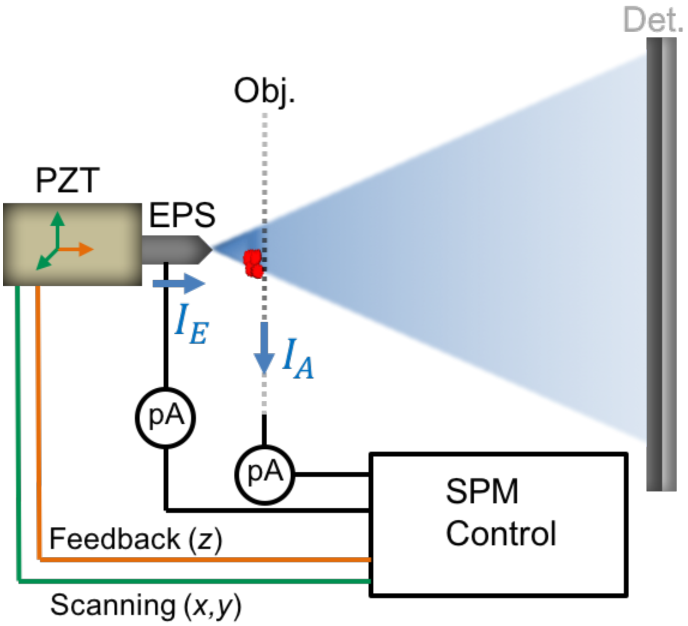

Figure 3.12: Scheme of absorption contrast field emission scanning probe microscopy AC-FESPM. A divergent beam of low-energy electrons is emitted by an electron point source **(EPS)** and the amplified emission current $\boldsymbol{I_E}$ is recorde by the SPM control system. Part of the beam is absorbed by the sample **(Obj.)** and measured as the absorption current $\boldsymbol{I_A}$. An SPM control system generates the scanning signals to drive a piezo tube scanner **(PZT)** in order to scan the tip across the sample surface. The source-to-sample distance is feedback-controlled to maintain either a constant emission current I_E or a constant absorption current I_A. AC-FESPM images are generated by mapping the variations in the source-to-sample distance (z-signal), the emission current I_E, the absorption current I_A, and the relative absorption $A_r = I_A/I_E$ as a function of x- and y-coordinates of the scan.

additional current signal provides a large contrast image channel. This mode is referred to as Absorption Contrast Field Emission SPM (AC-FESPM) mode (see the scheme sketched in Fig. 3.12.

The AC-FESPM mode is demonstrated on a graphene sample prepared freestanding over a 2 micrometer hole in a SiN membrane. Low magnification LEEPS micrographs of the sample are shown in Fig. 3.13. The sample features graphene of different numbers of layers, and clusters of adsorbates are spread across the graphene sheet. As the interference fringes cannot be sufficiently resolved at such low magnification, it is not possible to reconstruct these LEEPS micrographs.

In Fig. 3.14 AC-FESPM measurements conducted on the sample area corresponding approx-

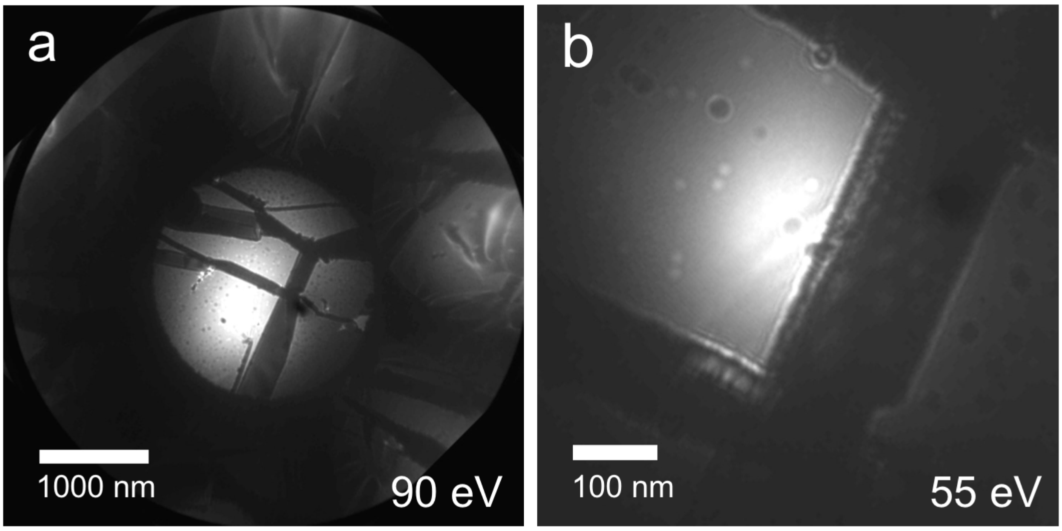

Figure 3.13: Low magnification LEEPS micrographs of the freestanding graphene sample studied with AC-FESPM in subsection 3.4.2.

imately to the one depicted in Fig. 3.13 (b) are presented. Two consecutive scans are shown, both recorded with a bias voltage of $V_{bias} = -28$ V and a slow feedback control. For the top row, the feedback loop is set to regulate the tip height for a constant absorption current $I_A = 0.6$ nA. The z-signal image thus represents the variation in the relative absorption of the sample, rather than the topology, as discussed in subsection 3.4.1. The bottom row is recorded with the emission current I_E as feedback parameter. A set point of $I_E = 1$ nA is chosen, as this corresponds to an absorption current of about 0.6 nA on single layer graphene. In this case, the z-signal image mainly reflects the sample topography. Since the field emission is rather unstable in both scans, a lot of current jumps are observed in the images – horizontal stripes in z-signal images, black and white spots in current images.

The images shown in Fig. 3.14 (a) to (c) demonstrate the benefits of AC-FESPM compared to FESPM with only one current signal. The second current signal, here the emission current I_E, directly reflects the absorption properties of the sample, in a much more quantitative way and with larger contrast than the z-signal image. The higher the relative absorption of the sample, the lower the emission current I_E needed to maintain a constant absorption current I_A. Thus multiple layers of graphene appear darker in Fig. 3.14 (c). In the bottom row, where the emission current I_E is kept constant by the feedback loop, in the absorption current signal I_A shown in Fig. 3.14 (e) the contrast is reversed compared to Fig. 3.14 (c), as expected.

With the AC-FESPM data at hand, the relative absorption of the sample is directly given by $A_r = I_A/I_E$ and can be used as a robust imaging signal. Abrupt changes in the field emis-

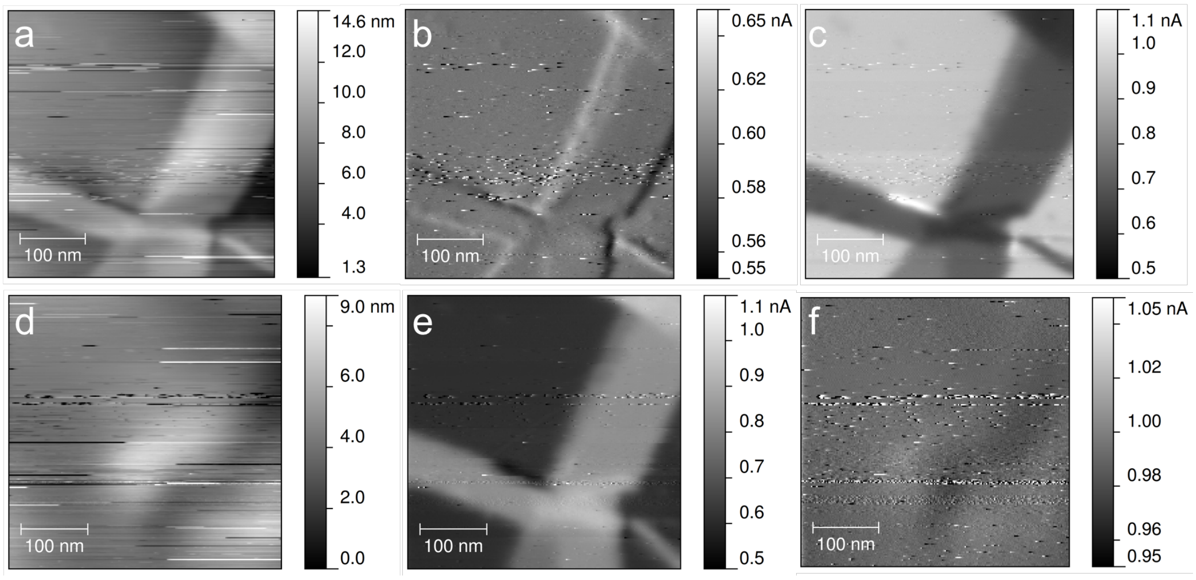

Figure 3.14: AC-FESPM imaging of a freestanding graphene sample with different layer thicknesses. The scan area is 400 × 400 nm^2, the bias voltage is $V_{bias} = -28$ V and a rather slow feedback control is employed. In the top row the tip height is regulated by the feedback loop for a constant absorption current of $I_A = 0.6$ nA. In the bottom row the tip height is regulated for a constant emission current of $I_E = 1$ nA. **(a)** Corrected z-signal image. **(b)** Absorption current I_A-signal image. **(c)** Emission current I_E-signal image. **(d)** Corrected z-signal image. **(e)** Absorption current I_A-signal image. **(f)** Emission current I_E-signal image.

sion performance of the tip, leading to peaks in the measured current signals are effectively corrected in the relative absorption signal A_r images, as demonstrated in Fig. 3.15.

Over the course of a scan, the relative absorption A_r observed for single layer graphene changes between discrete levels within a few percent around 0.6 as shown in the contrast adjusted images in Fig. 3.15 (b) and (e). This is rather surprising at first sight, as a constant absorption may be expected for a constant bias voltage, respectively a constant energy of the probing electrons. The variations of the relative absorption are observed to be correlated with the variations in the field emission characteristics of the tip, as seen when compared to the raw data z-signal images shown in Fig. 3.15 (c) and (f). As the sudden changes in the field emission characteristics of the tip are accompanied with changes of the angular field emission distribution, the variations of the relative absorption can be explained by a dependence on the in-plane momentum of the probing electrons, in consistency with the observations presented in chapter 4.

Another example of AC-FESPM is shown in Fig. 3.16. The scan is recorded with a bias voltage of $V_{bias} = -27$ V and an absorption set current of $I_A = 2$ nA. In the corresponding LEEPS

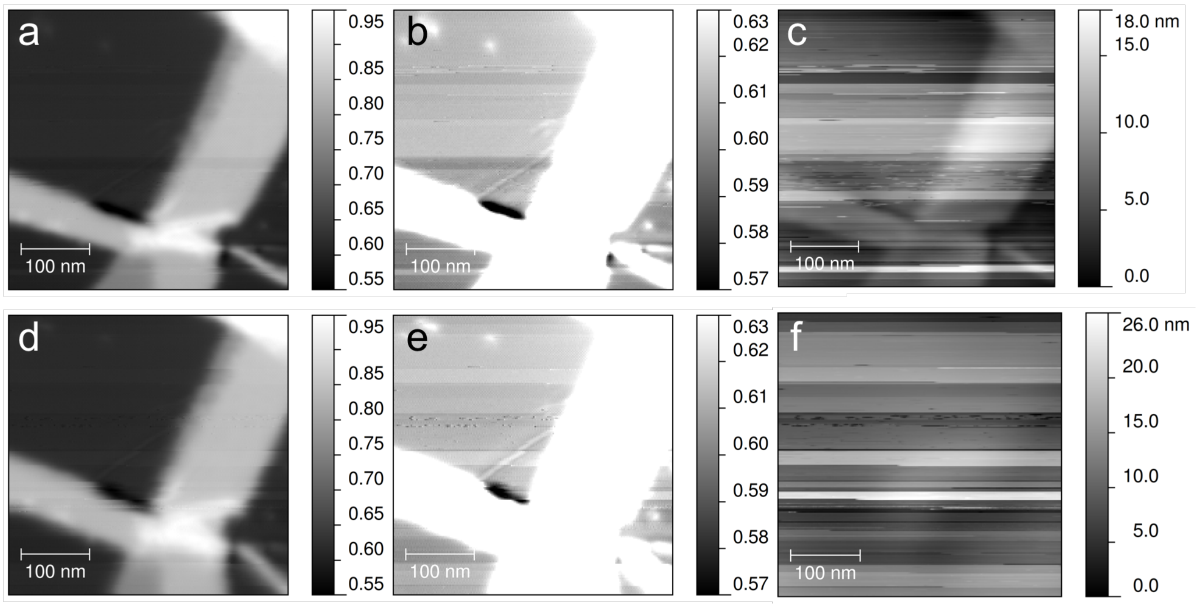

Figure 3.15: The relative absorption A_r as signal in AC-FESPM imaging. The scan area is 400×400 nm^2 and the bias voltage is $V_{bias} = -28$ V. In the top row the data is taken from the measurement shown Fig. 3.14 (a) to (c), recorded with constant absorption current. In the bottom row the data corresponds to Fig. 3.14 (d) to (f), recorded with constant emission current. **(a)** and **(d)** Relative absorption A_r-signal image. **(b)** and **(e)** Relative absorption A_r-signal image with the scale adjusted to the relative absorption of single layer graphene. **(c)** and **(f)** Raw data z-signal image, illustrating the correlation between variations in the relative absorption on single layer graphene and fluctuations in the field emission characteristics of the tip.

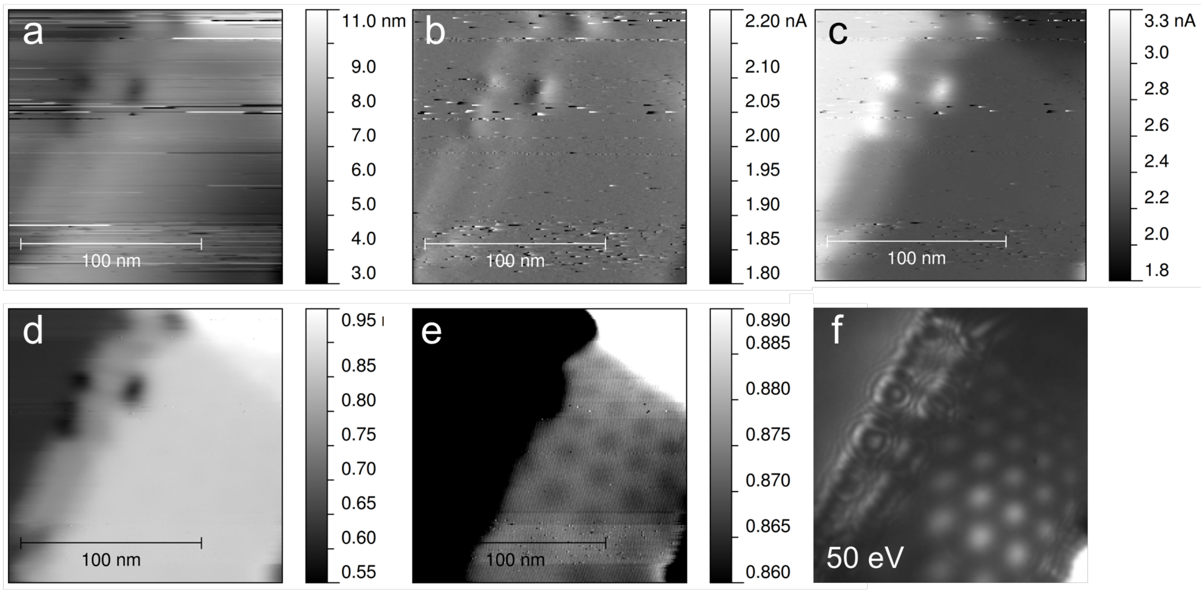

Figure 3.16: AC-FESPM measurement on a scan area of 150×150 nm^2, recorded with a bias voltage of $V_{bias} = -27$ V and an absorption set current of $I_A = 2$ nA. **(a)** Corrected z-signal image. **(b)** Absorption current I_A-signal image. **(c)** Emission current I_E-signal image. **(d)** Relative absorption A_r-signal image. **(e)** Relative absorption A_r-signal image. The scale is adjusted to show the small variations of the relative absorption on the triple layer graphene region, revealing a Moire pattern. **(f)** Leeps micrograph of the same sample region recorded with an electron energy of 50 eV of the same sample region.

micrograph a moiré pattern is observed on the multi-layer graphene. Such moiré patterns have been observed in LEEPS images before, as a result of the Talbot effect for two superimposed graphene layers rotated by a few degrees with respect to each other [47]. A similar moiré pattern is also observed in the AC-FESPM image as a small variation of about 1 % in the relative absorption signal A_r, as shown in Fig. 3.14 (e). Surprisingly, the orientation of the moiré pattern in the LEEPS image differs with about 10 degrees from the orientation of the moiré pattern in the AC-FESPM image. No conclusive explanation for this phenomena could be found so far.

3.4.3 Tip Sharpening by a Feedback-Controlled Crashing Procedure

When reducing the bias voltage to bring the tip closer to the sample in FESPM measurements, at some point the graphene sheet breaks due to some interaction with the tip. After such a “crash”, the graphene sheet suspended over a hole in a SiN membrane is either left behind with a hole or more often completely destroyed. In such crashes in FESPM experiments –

with the tip height regulated for constant absorption current I_A – the tip is usually blunted, and field emission sets in at a much larger bias voltage, for comparable emission current and tip-to-sample distance. However, on rare occasions the tip is modified in such a way that it is effectively sharpened, meaning a lower bias voltage was needed to get the same emission current at the same tip-to-sample distance. Such sharpened tips emit into an increased angular range, and allow to record high magnification holograms at very low electron energy as for example those shown before in Fig. 3.10 (a) and Fig. 3.11 (c).

With the possibility to use the emission current I_E as the feedback signal in the AC-FESPM setup, such tip crashes can be provoked in a controlled way with a high success rate in producing sharpened tips. The bias voltage V_{bias} is continuously reduced in a sweep while the tip-to-sample distance is feedback-controlled for a constant emission current I_E, such that the tip steadily approaches the sample and eventually crashes into it. In case the tip is sharpened during the crash, it is immediately retracted to a safe position by the feedback loop due to the sudden increase of the emission current.

Such a feedback-controlled tip crash procedure is demonstrated in Fig. 3.17 and Fig. 3.18. The initial tip is of high quality in terms of sharpness achievable by the etching and neon sputtering procedures described in subsection 3.3.5. At a distance of 3.5 µm from the sample, a bias voltage of $V_{bias} = -94$ V is needed for an emission current of $I_E = 10$ nA with the initial tip, see Fig. 3.17 (a). The tip's emission angle is not sufficient to illuminate the entire detector. A hologram of two large and one small clusters acquired with this initial tip at a distance of 270 nm and a bias voltage of -55 V is shown in Fig. 3.17 (d). Reducing the distance further with the purpose of producing a hologram of larger magnification would make no sense, as the part of the object wave diffracted under a large angle would not be superimposed by the reference wave.

In the second step of the experiment the tip is subject to a feedback-controlled tip crash procedure. The measurement protocol of the crash is shown in Fig. 3.18 (a). The procedure starts with a bias voltage of -40 V and an emission set current of $I_E = 2$ nA. As the bias voltage is swept down towards -30 V, the piezo extends towards the sample until a crash occurs at a bias voltage of -32.5 V. Here, the tip is blunted during the crash and the emission current suddenly drops to zero. The feedback tries to compensate, by extending the piezo to the limit of the scan range, but even when the bias voltage is raised again to -40 V at the end of the procedure, no emission current is drawn. At the end of the procedure, the tip is in a position pointing through the hole in the graphene, that has been created during the crash. In Fig. 3.17 (b) the blunted tip is retracted to a distance of 1.5 µm from the sample, at which it emits a current of 10 nA at -94 V, the same values as for the initial tip but at less than half the distance. The hole in the graphene created during the crash is visible in the LEEPS micrograph.

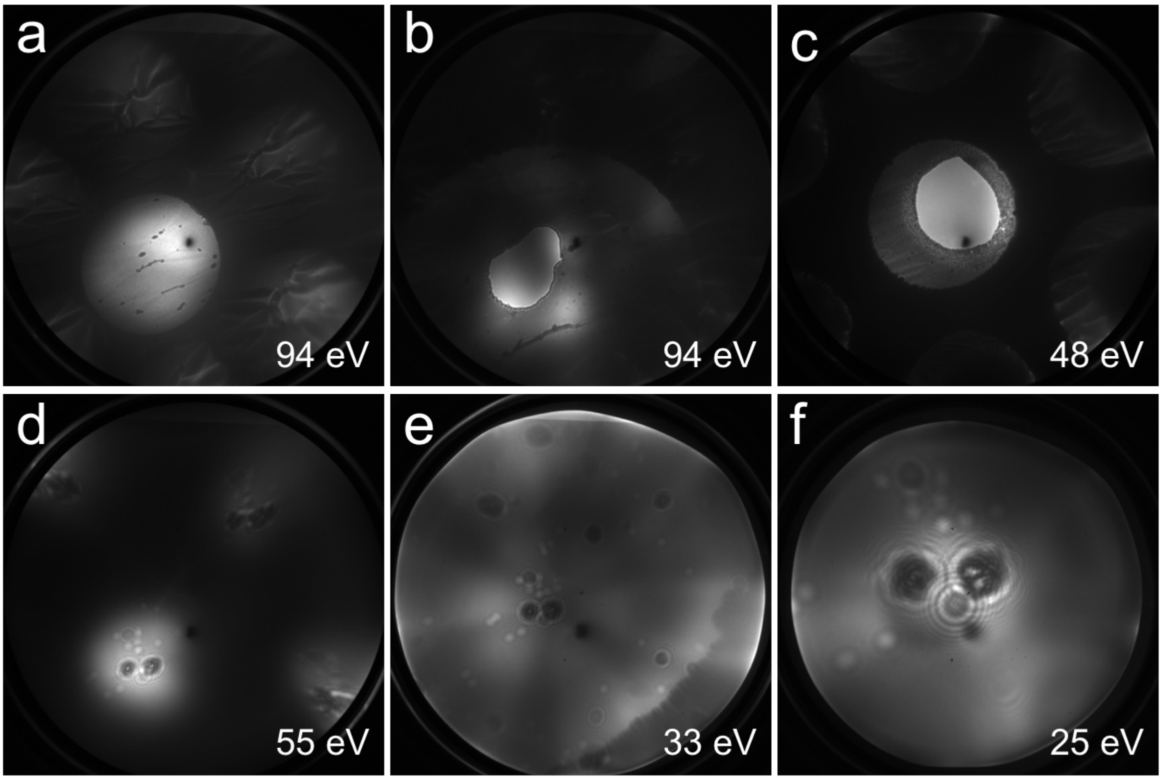

Figure 3.17: LEEPS micrographs recorded before and after feedback-controlled tip crash procedures. **(a)** Recorded at a tip-to-sample distance of 3.5 µm, a bias voltage of −94 V and an emission current of 10 nA with the initial tip. **(b)** Recorded with the blunted tip after the first tip crash procedure (Fig. 3.18 (a)), at a tip-to-sample distance of about 1.5 µm, a bias voltage of −94 V and an emission current of 10 nA. The hole in the graphene sheet due to the tip crash is apparent. **(c)** Recorded with the sharpened tip after the second tip crash procedure (Fig. 3.18 (b)), at a tip-to-sample distance of about 3.4 µm, a bias voltage of −48 V and an emission current of 10 nA. After the second tip crash, a hole of larger size in the graphene sheet is apparent. **(d)** Low-energy electron hologram of clusters recorded with the initial tip at an electron energy of 55 eV and a tip-to-sample distance of 270 nm. **(e)** Low-energy electron hologram of the same sample region as in (d) recorded with the sharpened tip at approximately the same tip-to-sample distance. The electron energy is decreased to 33 eV for the same emission current due to the increased sharpness of the tip. **(f)** High magnification low-energy electron hologram recorded with the sharpened tip at an electron energy of only 25 eV and a tip-to-sample distance of 85 nm.

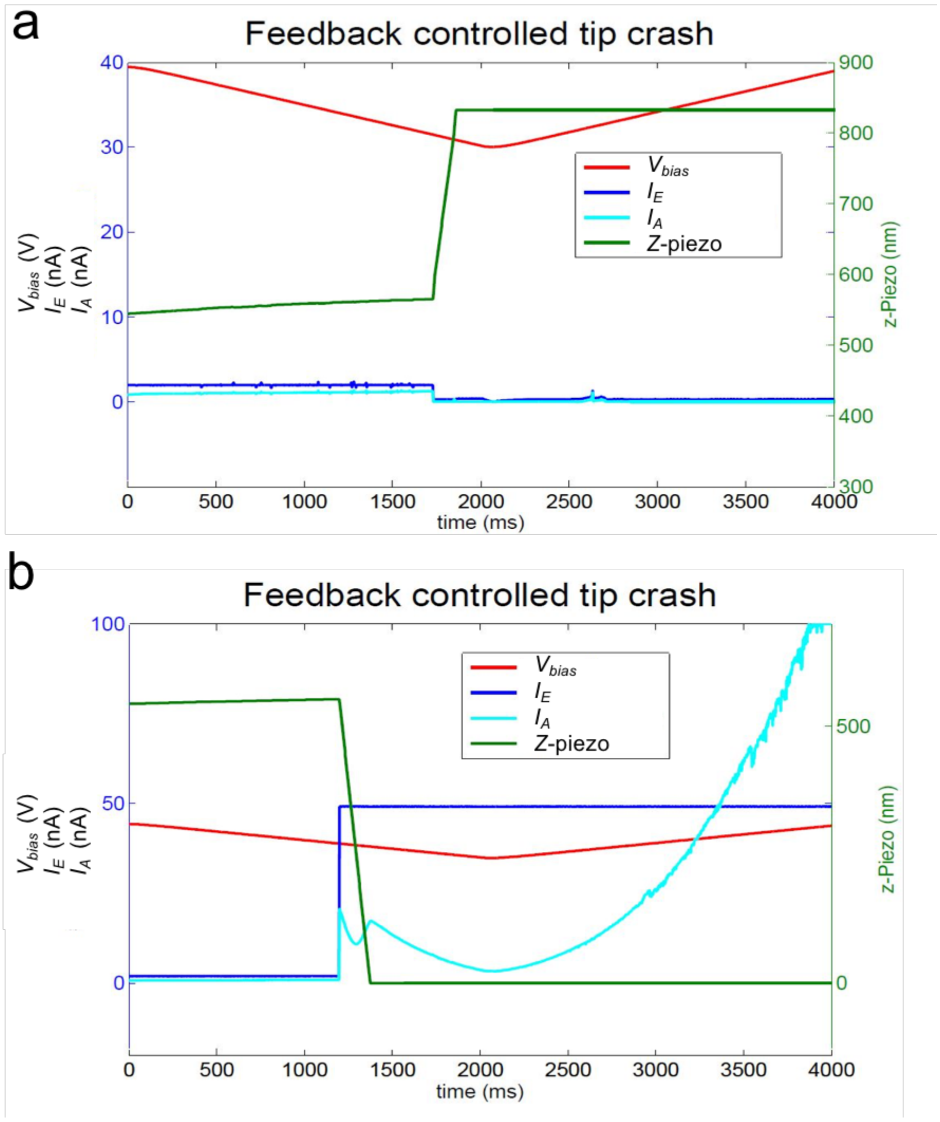

Figure 3.18: Protocols of the feedback-controlled tip crash procedure. The graphs show the bias voltage V_{bias}, the emission current I_E, the absorption current I_A and the extension of the piezo tube in z-direction as a function of time. **(a)** Feedback-controlled tip crash procedure resulting in a blunted tip. **(b)** Feedback-controlled tip crash procedure resulting in a sharpened tip.

The blunted tip is then positioned next to the hole and subject to a second feedback-controlled tip crash procedure, whose measurement protocol is shown in Fig. 3.18 (b). Here the crash occurs at a bias voltage of -38.5 V. The tip is sharpened during the crash, and a high current is immediately drawn, saturating the I-V amplifier, and the tip is retracted by the feedback loop as a consequence. As most of the emitted current passes through the hole in the graphene, only a small part of it is detected as an absorption current I_A by the current-to-voltage amplifier (IV1) connected to the sample. The increase in tip sharpness is demonstrated in Fig. 3.17 (c), where the tip is retracted to approximately the same tip-to-sample distance as in Fig. 3.17 (a). A bias voltage of only $V_{bias} = -48$ V is needed for an emission current $I_E = 10$ nA, much lower compared to the -94 V that were needed with the initial tip. In Fig. 3.17 (e) a hologram of the clusters recorded at approximately the same distance as in Fig. 3.17 (d) is shown – for the same emission current a bias voltage of only -33 V is needed with the sharpened tip instead of -55 V with the initial tip. In Fig. 3.17 (f) the sharpened tip is used to record a hologram at higher magnification and a bias voltage of only -25 V. The higher magnification is possible because the sharpened tip emits under an increased angular range up to the rim of the detector. The holograms shown in Fig. 3.17 (d) to (f) together with their reconstructions are discussed in more detail in subsection 3.4.4.

The exact mechanism leading to the sharpened tips is not understood yet. We speculate that a small graphene flake attaches to the tip apex after the crash and builds a fine elongated protrusion, from which the field emission occurs afterwards. An interesting observation is, that no peak in the current signal is detected during the crash as would be expected if a shortcut between tip and graphene occurs. The graphene flake might break due to electrostatic forces before a physical contact is reached and deposit on the tip afterwards.

3.4.4 Ultra-Low-Energy Electron Holography

Electron holography in the very low energy regime of 20 to 30 eV was investigated in the LEEPS/SPM system. This is at much lower energy, than what is typically employed in LEEPS microscopy (about 50 to 300 eV). Although holography with electron energy of 21 eV [22] and even 7 eV [82] has been reported, those holograms have not been reconstructed. High quality, reconstructable holograms at very low energy and high magnification can be recorded in the LEEPS/SPM system by employing graphene as the sample substrate and a field emission tip sharpened as described in subsection 3.4.3. The objects were numerically reconstructed from the holograms by Tatiana Latychevskaia using her reconstruction software package.

Subsections of the holograms from Fig. 3.17 (d) to (f) that were resized to display the same field of view are shown in Fig. 3.19 (a) to (c) . A stronger interference contrast is apparent for the hologram recorded with 25 eV compared to the holograms recorded at higher energy and larger distance. The object reconstructions of the holograms are shown in Fig. 3.19 (d) to (f). The shape of the clusters changed in between the time the holograms were acquired as a result of adsorbate aggregation due to relatively poor vacuum conditions of 6×10^{-8} mbar during the experiment. The resolution of the reconstructions was determined by analyzing

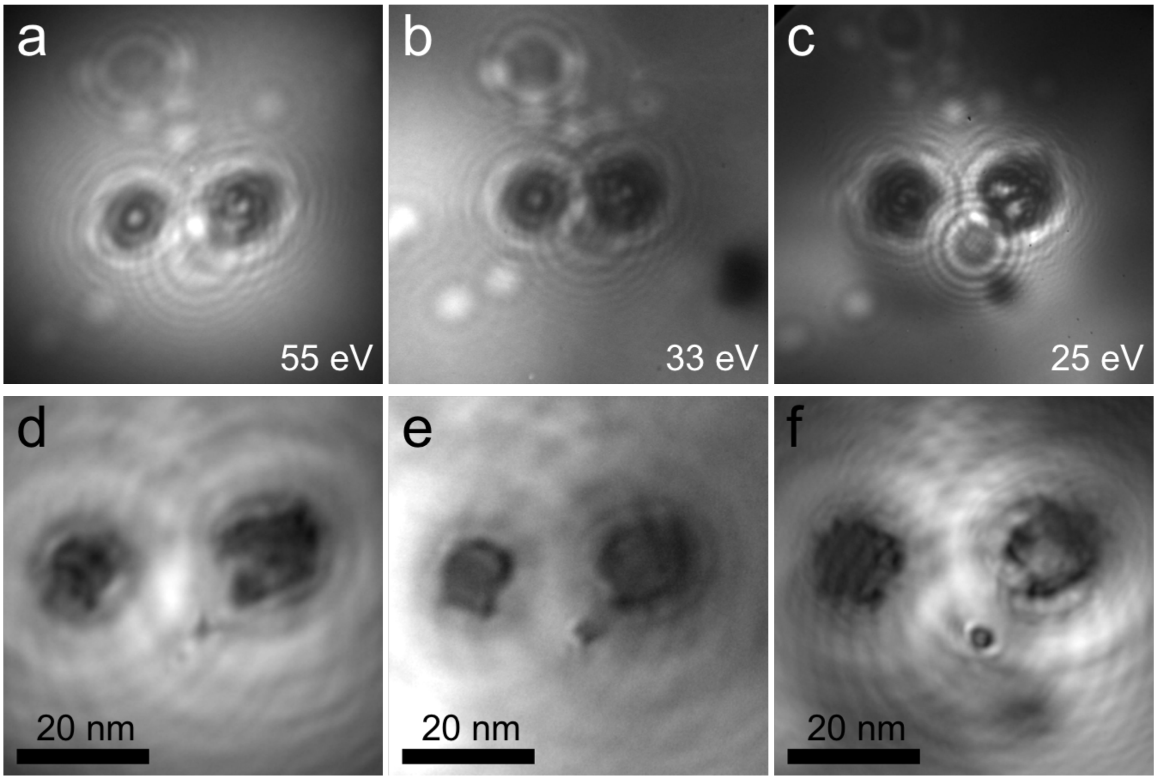

Figure 3.19: Subsections of the holograms from Fig. 3.17 (d) to (f) covering the same field of view. **(a)** Recorded with 55 eV electron energy at a tip-to-sample distance of 270 nm. **(b)** Recorded with 33 eV electron energy at a tip-to-sample distance of 280 nm. **(c)** Recorded with 25 eV electron energy at a tip-to-sample distance of 85 nm. **(d)** The object reconstruction of (a), with a resolution of 1.7 nm. **(e)** The object reconstruction of (b), with a resolution of 1.8 nm. **(f)** The object reconstruction of (c), with a resolution of 1.1 nm.

their Fourier spectra [44], yielding values of 1.7 nm for Fig. 3.19 (d), 1.8 nm for Fig. 3.19 (e) and 1.1 nm for Fig. 3.19 (f). The best resolution is achieved in the reconstruction from the hologram recorded with 25 eV and a short tip-to-sample distance despite the larger wavelength (2.5 Å for 25 eV, 1.7 Å for 55 eV), as a result of the increased effective numerical aperture. Note that the bright spots in the holograms do not converge to meaningful objects in the reconstruction. Their origin is discussed in chapter 5.

Additional examples of ultra-low-energy holograms of clusters on freestanding graphene are shown in Fig. 3.20. These holograms were recorded with different tips, that were all sharpened in a feedback-controlled tip crash procedure. The reconstructions reveal objects of a few nanometers in size and sub-nanometer resolution is achieved.

Sometimes also features that show only low interference contrast are observed in low-energy

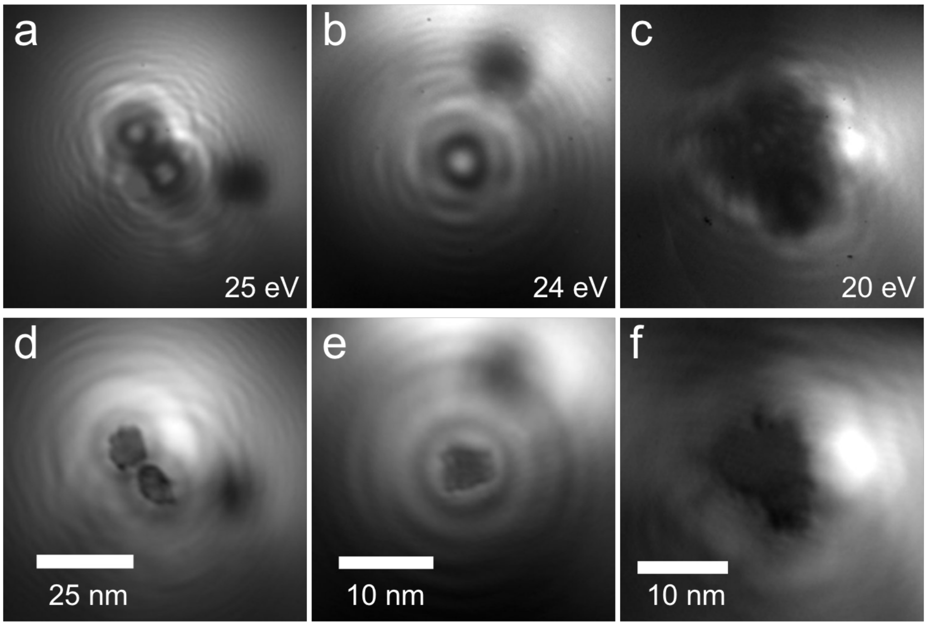

Figure 3.20: Ultra-low-energy electron holograms of clusters on freestanding graphene and their reconstructions. The holograms were acquired with different tips prepared in a feedback-controlled tip crashing procedure. **(a)** Recorded with 25 eV electron energy at a tip-to-sample distance of 88 nm. **(b)** Recorded with 24 eV electron energy at a tip-to-sample distance of 46 nm. **(c)** Recorded with 20 eV electron energy at a tip-to-sample distance of 58 nm. **(d)** The object reconstruction of (a), with a resolution of 1.0 nm. **(e)** The object reconstruction of (b), with a resolution of 0.8 nm. **(f)** The object reconstruction of (c), with a resolution of 0.9 nm.

electron holograms apart from the usually observed clusters with stronger contrast. A hologram of such an object is shown Fig. 3.20. The contrast is increased at very low electron energies, which allows to acquire holograms in which a lot of interference fringes are visible. The numerical reconstruction of such a hologram acquired with 27 eV electron energy reveals an object with a full width at half maximum of 1.5 nm in the intensity distribution.

3.4.5 Preliminary STM Measurements

First experiments with STM on freestanding graphene have been performed as well. The tip is positioned above a freestanding graphene layer in the LEEPS mode. Approaching the graphene with the tip under feedback control always leads to a sudden increase of the current signal to a value saturating the current amplifier, rendering it impossible to obtain a stable tunneling junction. This behavior is observed for a large range of bias voltages of

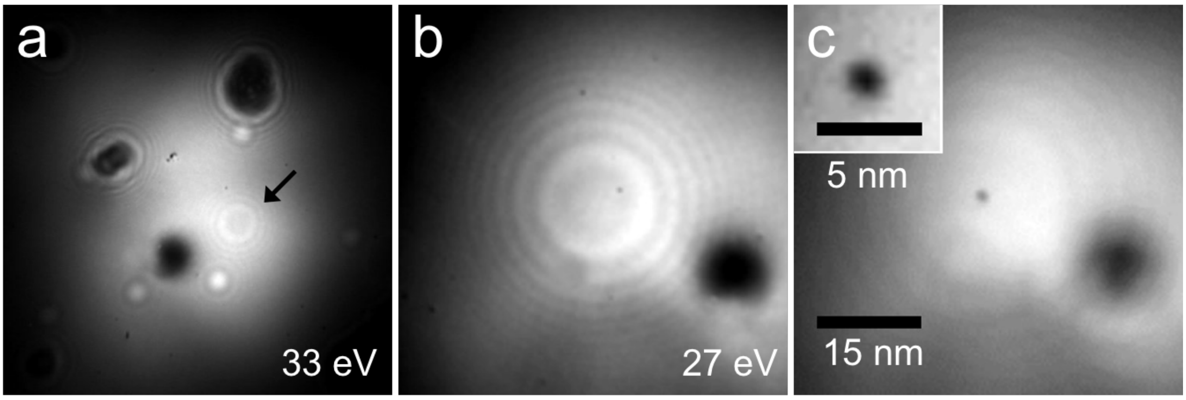

Figure 3.21: Holograms of an adsorbate with low contrast. **(a)** Recorded at a tip-to-sample distance of 250 nm and an electron energy of 33eV. The object marked with an arrow shows low interference contrast compared to typical clusters observed on freestanding graphene. **(b)** A hologram of the low contrast object recorded at 27 eV electron energy and a tip-to-sample distance of 93 nm. **(c)** The object reconstruction of (b), revealing a small object with a full width at half maximum of 1.5 nm. The inset shows a magnified view with enhanced contrast.

both polarity and for different set points of the current. When the tip is retracted to a large distance afterwards, the LEEPS mode can be used again to image the graphene sheet. The field emission performance of the tip does not change significantly due to the unsuccessful attempts to establish a tunneling junction; no change of the tip sharpness is observed. Also the freestanding graphene layer remains intact. This shows that the feedback control performs well, and the difficulties are attributed to a lack of mechanical rigidity of the setup.

Further tests showed that a stable tunneling junction can be established on more rigid substrates. As an example, STM images of a palladium layer sputter-coated on a silicon nitride membrane have been recorded. Prior to the STM measurement the tip is brought into a distance of approximately 100 nm to the sample with the coarse piezo positioner in the LEEPS mode, with a hole in the membrane serving as a reference point. The tip is then laterally shifted to a distance of 1 micrometer from the hole. Afterwards the electric connections to all coarse piezo positioner are grounded, to avoid the coupling of electrical noise from the coarse piezo control unit. A constant bias voltage V_{bias} is applied to the tip and the sample current is measured with the Femto I-V converter (IV1). When the feedback control is turned on, the tip gradually approaches the sample to safely enter the tunneling regime. STM images are then recorded in constant current mode, revealing Pd clusters with an average lateral size of approximately 5 nm and a layer corrugation of the same order, as seen in Fig. 3.22 (a).

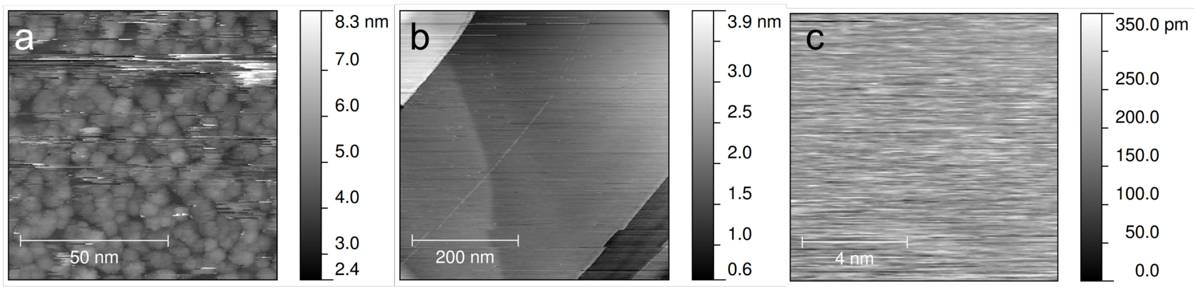

Figure 3.22: Constant current STM images. **(a)** A sputter coated Pd layer, recorded with a set current of $I_A = 0.5$ nA and a bias voltage $V_{bias} = 500$ mV. Clusters with an overall size of about 5 nm are visible. **(b)** Cleaved HOPG recorded with a set current of $I_A = 1$ nA and a bias voltage of $V_{bias} = -500$ mV. Steps with a height of of several atomic layers are visible. **(c)** 10×10 nm^2 scan on a flat sample region on HOPG recorded with a set current of $I_A = 0.5$ nA and a bias voltage $V_{bias} = 150$ mV. No atomic resolution is achieved, but rather a noisy variation of the z-signal in the order of 3 Å is measured.

The horizontal stripes or scars in the image are attributed to tip instabilities, which are likely to occur for such a strongly corrugated sample. Nevertheless, a stable tunneling junction is maintained for several scanning lines, and the clusters are resolved with nanometer resolution.

Cleaved HOPG (highly oriented pyrolytic graphite) has been used as an additional test sample. Due to the non-transparency of the sample in the LEEPS mode, a standard STM auto approach is used to bring the tip into tunneling distance: The coarse z-piezo motor is first driven forth for about 500 nm, then the tip is further approached by the piezo tube scanner with the feedback control enabled. If no tunneling current is sensed before the end of the scan range is reached, the tip is retracted by the piezo tube scanner to repeat the approach procedure by again bringing the tip closer via the coarse piezo. Once the tip is in tunneling junction, the coarse piezo motors must be grounded before starting the actual STM measurements.

It proved to be much easier to maintain a stable tunneling junction on such a flat sample, as can be seen in Fig. 3.22 (b) for example. However, even on supposedly atomically flat regions of the HOPG sample, no atomic resolution has been obtained so far. The z-signal only shows a noisy signature with a variation in the order of 3 Ångstrom, as shown in Fig. 3.22 (c). It is believed, that this is due to a lack of rigidity of the setup, leading to a relative motion of the tip with respect to the sample in the course of an STM measurement.

To achieve atomic resolution imaging and stable tunneling for freestanding samples further improvements of the experimental setup will be needed. Most likely the remaining lack of stability stems from the Attocube coarse piezo positioners due to their poor mechanical rigidity. Related resonance frequencies in the order of a few hundred Hz have occasionally been observed in accordance to what was reported for such motors [83].

CHAPTER 4

Mapping Unoccupied Electronic States of Freestanding Graphene by Angle-Resolved Low-Energy Electron Transmission

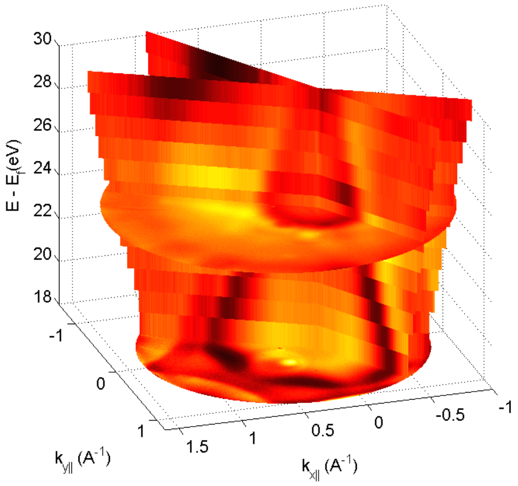

The following chapter contains a modified version of a manuscript published in Physical Review B:

F. Wicki, J.-N. Longchamp, T. Latychevskaia, C. Escher, H.-W. Fink, *Mapping Unoccupied Electronic States of Freestanding Graphene by Angle-Resolved Low-Energy Electron Transmission*, Physical Review B, **94**, 075424 (2016).

Abstract

We report angle-resolved electron transmission measurements through freestanding graphene sheets in the energy range of 18 to 30 eV above the Fermi level. The measurements are carried out in a low-energy electron point source microscope, which allows simultaneously probing the transmission for a large angular range. The characteristics of low-energy electron transmission through graphene depend on its electronic structure above the vacuum level. The experimental technique described here allows mapping of the unoccupied band structure of freestanding two-dimensional materials as a function of energy and probing angle, respectively in-plane momentum. Our experimental findings are consistent with theoretical predictions of a resonance in the band structure of graphene above the vacuum level [84].

4.1 Introduction

The electronic structure of a material is of great interest for a fundamental understanding of its mesoscopic properties and associated applications. While the occupied bands below the Fermi energy may be determined by different experimental methods like for example angle-resolved photoemission spectroscopy (ARPES) [85–88], the unoccupied bands are much more difficult to measure. However, experimental access to the unoccupied band structure above the vacuum level is possible to some extent with very low-energy electron diffraction (VLEED) spectroscopy [89–91], where the intensity of a reflected electron beam is measured as a function of electron energy and in-plane momentum. The electron reflectivity depends on the degree of coupling of the probing electron to empty states in the electronic structure of the sample. Another approach involves angle-resolved secondary electron emission (ARSEE), where excited electrons emitted from previously unoccupied states are identified in the fine structure of the secondary electron emission spectra [92, 93].

Already in 1947, the linear dispersion of the electronic bands of graphene in the vicinity of the K point was predicted by Wallace using a tight binding model [94]. But it was only in 2004, when graphene became accessible to experimentalists [95] and since then, the energy states below and a few eV above vacuum level have been studied extensively both in theory and experimentally and are well understood by now [96–101]. However, only few studies are available concerning the higher lying electronic structure above the vacuum level. Ab-initio calculations show the existence of discrete states immersed in the continuous spectrum above the vacuum level [84, 102]. Only recently, the existence of a special kind of scattering resonance in graphene originating from a strong coupling of the in-plane and perpendicular motions was predicted [84]. Ab-initio scattering theory [84,103] predicts that such resonances lead to a sharp transition from high to low transmission of an incident electron above respectively below the resonance energy. Measurements of the electronic structure above the vacuum level of single and multilayer graphene on SiC have been reported in a low-energy electron microscopy (LEEM) study based on the measuring principle of VLEED [104]. In an ARSEE experiment on graphene/Ni(111), spectral features were assigned to empty states in the graphene band structure by comparison with density functional theory calculations and a first experimental evidence of the aforementioned scattering resonance was provided [102]. To our knowledge, no experimental findings concerning the electronic structure of freestanding graphene above the vacuum level have been published so far.

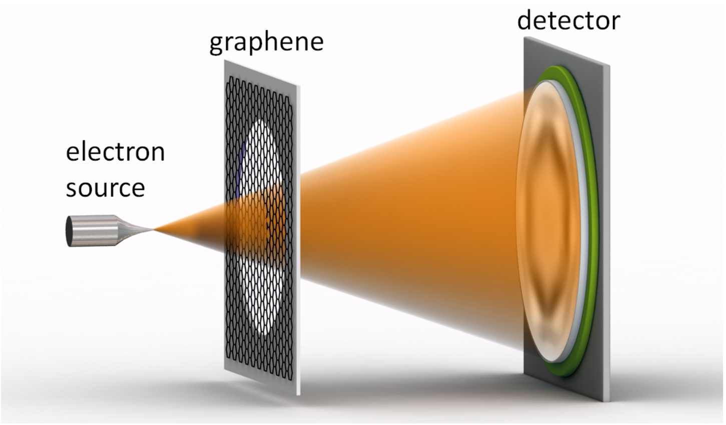

Figure 4.1: Schematics of the LEEPS microscope setup. A sharp W(111) tip acts as a field emitter source of a divergent electron beam. The electron wave is scattered off the sample placed in close proximity to the source. The result of this scattering experiment is captured at a distant detector.

4.2 Experimental Methods and Results

Here, we report the measurement of angle-resolved electron transmission through freestanding graphene using a low-energy electron point source (LEEPS) microscope [22]. A schematic of the experimental setup is shown in Fig. 4.1. A divergent beam of coherent low-energy electrons, field emitted from a sharp W(111) tip, is directed towards the graphene sample held at a distance of a few tens to hundreds of nanometers from the electron source. By means of a piezo positioner, the electron point source can accurately be positioned in front of the graphene sheet. The transmission signal through the graphene is recorded on a detector unit consisting of a micro-channel plate (MCP), a phosphor screen and a digital camera. The sensitive detector area has a diameter of 75 mm and is placed 47 mm behind the sample. Hence, transmission signal is captured within a full angle of 77°. Freestanding graphene over holes of 2 micrometer in diameter in a palladium coated silicon nitride membrane is prepared following the procedure described elsewhere [105].

Single layer graphene has proven to be a suitable sample substrate with a transparency of the order of 70 % for electron energies of 50 to 250 eV typically employed in LEEPS holography experiments [46, 47]. However, when lowering the electron energies to about 30 eV and below, we find a rather strong angular dependence of the electron transmission through freestanding graphene. The transmission images from a single layer graphene sheet show 6-fold symmetric patterns. Moreover, the orientation of the patterns depends on the one of the crystal lattice of the particular graphene domain. This observation is exemplified in Fig. 4.2,

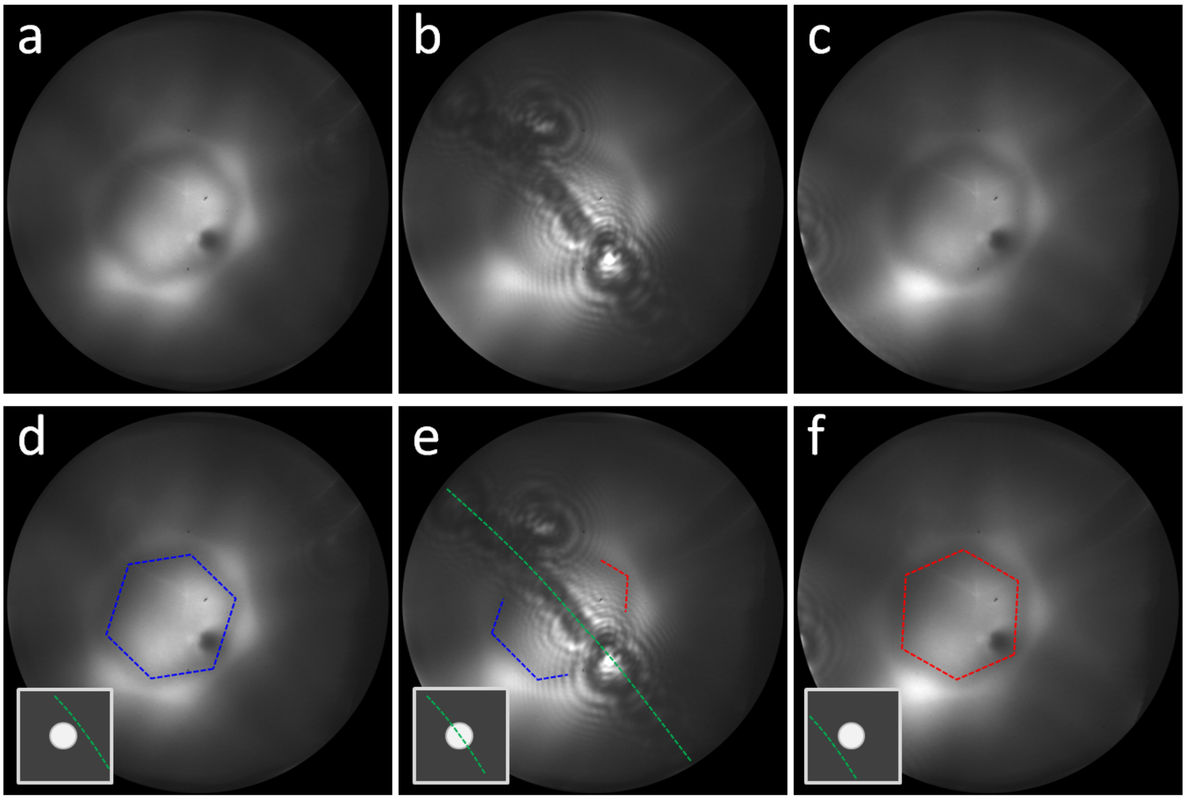

Figure 4.2: Low-energy electron transmission images of single layer freestanding graphene recorded while moving the field emission tip across a domain boundary. **(a)** Transmission image recorded with the tip on the left side of the boundary. **(b)** Image recorded with the tip in front of the boundary. Clusters decorating the boundary lead to the formation of an in-line hologram. **(c)** Transmission image recorded on the right side of the domain boundary. **(d)-(f)** The same images as in (a)-(c) but with blue and red colored dashed lines to guide the readers eye to the different orientations of the 6-fold symmetric pattern, which depend on the orientation of the crystal lattice of the particular graphene domain. In (e) the green dashed line indicates the domain boundary. The bright discs in the sketches at the bottom left corner of (d)-(f) indicate the position of the probed sample area with respect to the domain boundary. The diameter of the probed sample area amounts to about 100 nm.

where LEEPS microscopy images are shown recorded with 22 eV electrons while moving the field emission tip across the boundary of two adjacent domains in a single layer graphene sheet. Apparently, the orientation of the 6-fold symmetric pattern in the transmission image changes according to the change of the domain orientation, as indicated in Fig. 4.2(d) and (f). The transmission image shown in Fig. 4.2 (b) is recorded with the tip placed right in front of the domain boundary. Elastic scattering of clusters decorating the domain boundary leads to the formation of a hologram. Note that part of the 6-fold symmetric pattern associated with the transmission through graphene is apparent with different orientation on either side of the domain boundary. At first sight, one might be tempted to consider the appearance of the hexagon being due to some sort of diffraction pattern. However, the condition of a plane or slightly divergent wave creating a far-field diffraction pattern are not given and moreover, such pattern, probing two graphene domains at once would resemble a superposition of two similar 6-fold symmetric patterns. The diameter of the probed area varies with the source to sample distance and amounts to about hundred nanometers in Fig. 4.2.

In the transmission images presented here, the sample is probed at once under a large angular range and at constant kinetic energy of the incident electrons. The in-plane momentum component $k_{\|}$ of a probing electron is determined by the angle θ as illustrated in Fig. 4.3 (a). A single transmission measurement thus corresponds to a constant energy map in $T(\boldsymbol{k}_{\|}, E)$, the electron transmission as a function of in-plane momentum and energy. Since the transmission probability for a low-energy electron depends on its specific coupling to the electronic states of the sample, such a measurement allows drawing conclusions about the electronic structure $E(\boldsymbol{k})$ of the sample.

The energy E of the probing electrons with respect to the Fermi level E_f of the graphene sample is given by the tip potential $E = eU_0$, and their kinetic energy E_{kin} behind the sample is given by $E_{\text{kin}} = eU_0 - \Phi_{\text{s}}$, with Φ_{s} being the work function of the sample. The width of the energy distribution of the emitted electrons amounts to roughly 250 meV, typical for field emission from a (111)-oriented tungsten emitter [20,21]. The in-plane wave vector magnitude of the electrons is conserved in a sample/vacuum transition and is given by $k_{\|} = k \cdot \sin\theta$ with the total momentum $\hbar k = \sqrt{2m_{\text{e}}E_{\text{kin}}}$ and the probing angle θ.

A raw data transmission image recorded with an electron energy of 20 eV is shown in Fig. 4.3(b). We correct for the anisotropic emission of the electron source by dividing the transmission images with an approximate background image calculated as the average of a series of transmission images recorded with different energies (see Fig. 4.7 (c)). In Fig. 4.3 (c) the background corrected data of Fig. 4.3 (b) are shown, interpolated to $\boldsymbol{k}_{\|}$-space [23]. The arrows indicate the directions along $\overline{\Gamma M}$ and $\overline{\Gamma K}$ of the Brillouin zone. The orientation of the Brillouin zone is determined by a comparison with the first order diffraction disks apparent when larger electron energies are used (see Fig. 4.7 (a) and (b)).

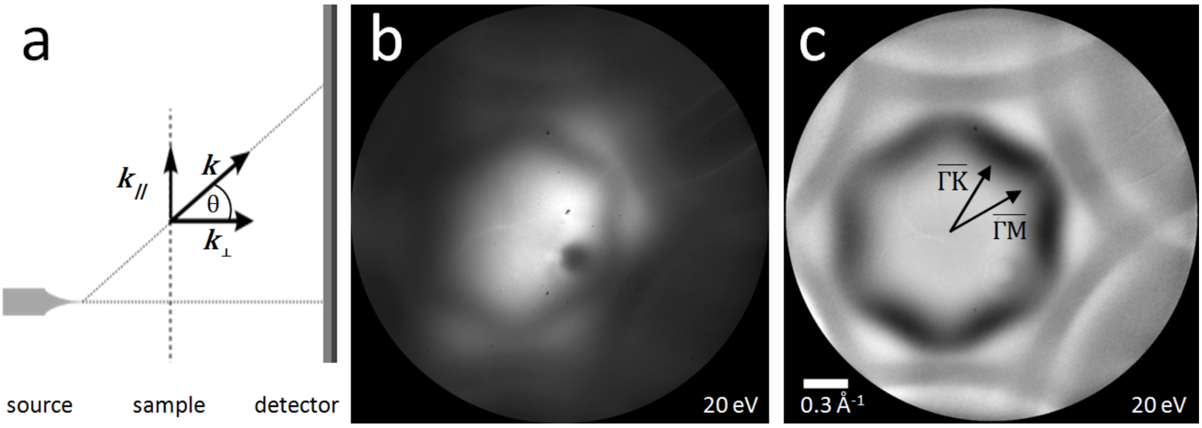

Figure 4.3: Principle of in-plane momentum resolved transmission measurements in the LEEPS microscope. **(a)** Schematics illustrating the determination of the in-plane momentum components of the incident electrons. Electrons are field-emitted from a sharp tip and arrive at the freestanding graphene sheet under a large angular range. The in-plane momentum of an electron in the graphene plane is related to the probing angle θ and the total momentum $\hbar k = \sqrt{2m_\mathrm{e}E_\mathrm{kin}}$. While the kinetic energy is determined by the tip bias potential and the work function of the sample, the angle can be determined from the position where the electron is recorded in the detector plane. **(b)** Raw data image of the transmission intensity recorded with an electron energy of 20 eV. The transmission intensity shows a 6-fold symmetry in accordance with the reciprocal crystal lattice of graphene, the background intensity varies due to anisotropic emission from the field emitter tip. The small dark spots are due to detector defects, the larger dark spot in the bottom-right corner of the dark hexagonal shape is the blind spot of the MCP where electrons enter nearly parallel to the channels and are less amplified. **(c)** Background corrected transmission intensity of (b) interpolated to $\boldsymbol{k}_{\|}$-space. The arrows indicate the directions along the high symmetry axes $\overline{\Gamma M}$ and $\overline{\Gamma K}$ in the Brillouin zone.

A relatively high transmission is observed for low $\boldsymbol{k}_{\|}$-values. For increasing $\boldsymbol{k}_{\|}$-values a dark hexagonal region of low transmission oriented with the edges pointing in the $\overline{\Gamma M}$ direction passes into a region of high transmission with a larger extent in the $\overline{\Gamma K}$ direction. The positions and widths are in agreement with the lowest branch of the scattering resonance predicted by Nazarov et al. (see Fig. 4 in Ref. [84]). We therefore conclude that this is the first experimental observation of this scattering resonance in freestanding graphene.

The transitional region from low to high transmission is surrounded by a region of reduced transmission in the form of a six-pointed star with nearly constant width in $\boldsymbol{k}_{\|}$-space. This again is in good agreement with ab-initio calculations [84][1].

---

[1] The presence of this feature in the ab-initio calculations presented in Fig. 4 in Ref. [84] was confirmed by

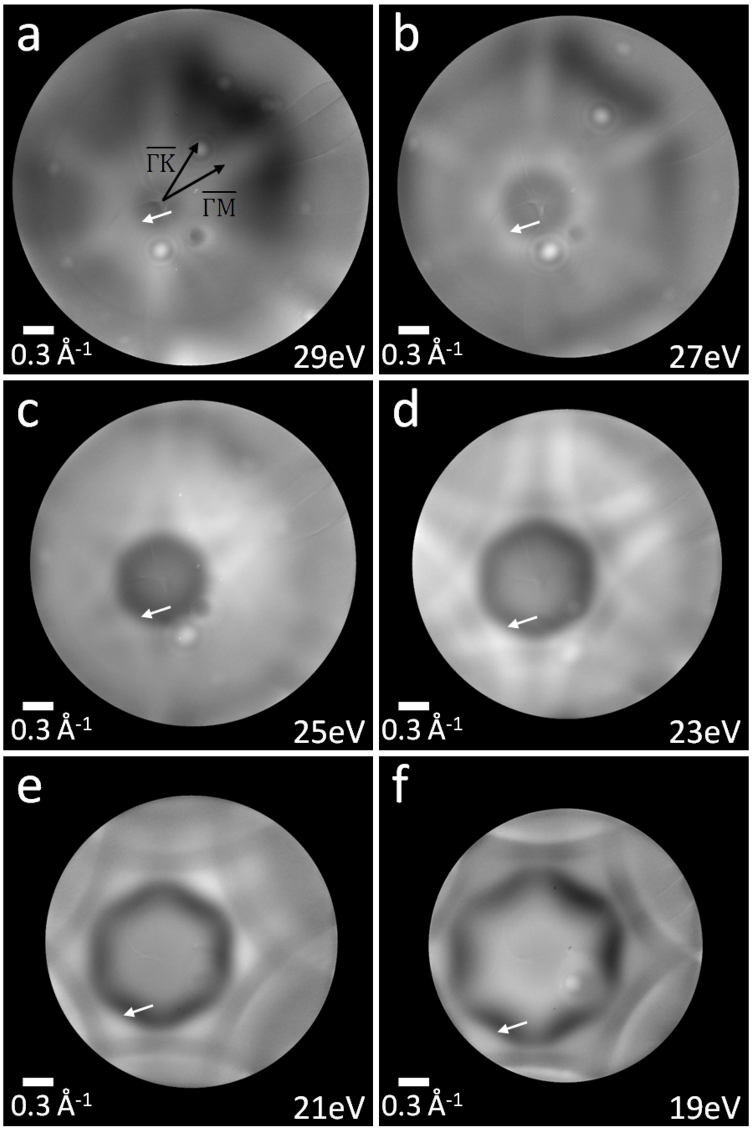

Figure 4.4: Background corrected transmission intensity in linear grayscale as a function of $\boldsymbol{k}_{\|}$ recorded with electron energies ranging from 29 eV down to 19 eV. The orientation of the Brillouin zone is indicated with according black arrows in (a). Each image corresponds to a constant energy map of the scattering band structure $T(\boldsymbol{k}_{\|}, E)$. The few bright spots are due to impurities on the graphene (e.g. visible in (a)). The transmission probability for a probing electron depends on its specific coupling to the unoccupied states of the sample which leads to signatures in the constant energy maps of $T(\boldsymbol{k}_{\|}, E)$ with a 6-fold symmetry. The pronounced transition from low to high transmission (marked with white arrows) is associated with a scattering resonance in compliance with ab-initio predictions [84].

E. E.Krasovskii (private communication).

In Fig. 4.4, background corrected transmission images are shown for electron energies of 29 eV down to 19 eV in steps of 2 eV. The probed sample area, which is determined by the tip to sample distance, is about 300 nm for the measurement recorded with 29 eV shown in Fig. 4.4 (a). When lowering the electron energy respectively the bias potential, the tip to sample distance is reduced to maintain a constant emission current of a few nanoamperes. Accordingly, the probed sample area gradually shrinks to about 50 nm in diameter at 19 eV as shown in Fig. 4.4 (f). Although the background correction provides transmission intensities in arbitrary units only, the intensities can reasonably be compared among different energies. The transition from low to high transmission associated with the scattering resonance can clearly be distinguished for all energies. With decreasing energy this transition shifts to higher $\boldsymbol{k}_{\|}$-values and the dispersion is in good agreement with theoretical predictions [84].

The dispersion of the low transmission branch of the scattering resonance can easily be recognized in Fig. 4.5, where the transmission intensity along the high symmetry directions $\overline{\mathit{\Gamma} M}$ and $\overline{\mathit{\Gamma} K}$ is shown as a function of E and $k_{\|}$. The intensity is extracted along the direction of the arrows indicated in Fig. 4.4 (a) from a measurement series recorded with electron energies from 30 eV down to 18 eV in 1 eV steps (see Fig. 4.6). The transmission intensity along the high symmetry lines is in qualitative agreement with measurements of electron reflection from graphene on SiC [104]. A reduced transmission is measured for regions in $(E, \boldsymbol{k}_{\|})$-space where a relatively high reflection has been reported. In the transmission intensity distributions at electron energies of 29 eV and 27 eV shown in Fig. 4.4 (a) and (b), the transmission at $\boldsymbol{k}_{\|}$-values above the scattering resonance is larger along the $\overline{\mathit{\Gamma} M}$ direction than along the $\overline{\mathit{\Gamma} K}$ direction, in accordance with theoretical predictions. This gradually changes when the energy is lowered and for 23 eV, shown in Fig. 4.4 (d), the transmission along the $\overline{\mathit{\Gamma} M}$ direction is reduced. In the transmission images recorded at the very low electron energies of 21 eV and 19 eV, there is an additional region of lower transmission appearing for $\boldsymbol{k}_{\|}$-values above the scattering resonance. This outer domain of low transmission can be clearly recognized as six-pointed star enclosing the hexagonal pattern in Fig. 4.4 (e) and (f).

In general, the characteristics observed here are in excellent agreement with the ab-initio predictions regarding their position in energy and in-plane momentum space. However, the relative transmission intensities deviate from the calculations. For example, the highest transmission probability is predicted to be at $\boldsymbol{k}_{\|}$-values above the scattering resonance for all energies. In contrary to that, the experimental findings suggest a larger transmission in the centre of the Brillouin zone at an energy of 19 eV as shown in Fig. 4.4 (f). We attribute this discrepancy to inelastic processes giving rise to enhanced absorption at higher $\boldsymbol{k}_{\|}$-values. Such effects have not been taken into account for the ab-initio calculations [84].

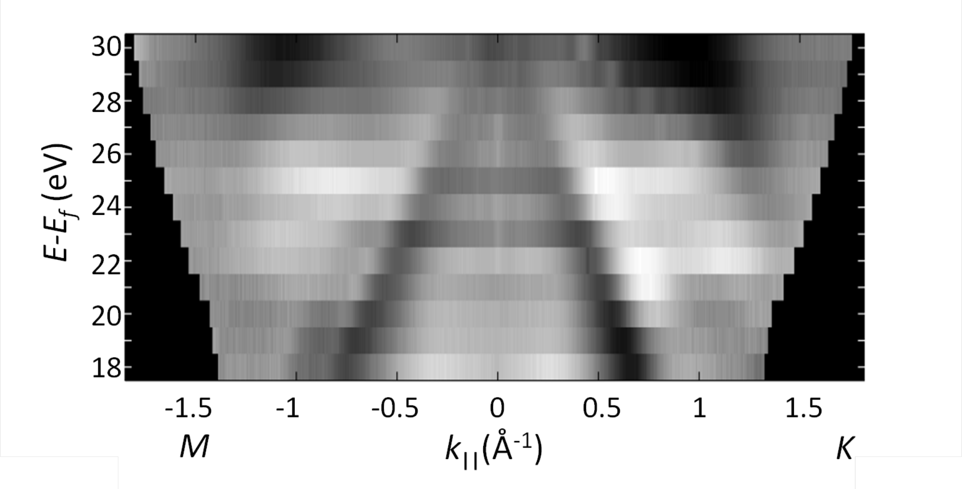

Figure 4.5: Plot of the background corrected transmission intensity as a function of the electron energy and the $k_{\|}$-values in $\overline{\Gamma M}$ and $\overline{\Gamma K}$ direction of the Brillouin zone. The intensity was extracted in the direction of the arrows indicated in Fig. 4.4 (a) for transmission images recorded with energies from 30 eV down to 18 eV in steps of 1 eV. The dispersion of the low transmission signature associated with the scattering resonance is in good agreement with theoretical predictions [84].

4.3 Conclusions

To summarize, we carried out angle-resolved electron transmission measurements on freestanding graphene revealing scattering resonances predicted by theory. Using the setup of a LEEPS microscope, it is possible to record constant energy maps of the transmission function $T(\boldsymbol{k}_{\|}, E)$ in a fraction of a second. Unoccupied states can thus be mapped in all directions of the Brillouin zone at once, rather than having to scan along a certain direction of the Brillouin zone and measuring point fort point as in common VLEED or ARSEE setups. Moreover, the probing area can be as small as a few tens of nanometers in diameter and thus allows probing of freestanding two-dimensional materials, which can often be prepared on the micrometer scale only.

The technique described here can also be applied to study other two-dimensional materials provided that they are sufficiently transparent to low-energy electrons and can be prepared freestanding. Possible candidates for further studies are few layer graphene sheets, single layer hexagonal boron nitride/graphene compounds, exfoliated single layer molybdenum disulphide [106] or heterostructures of graphene and transitional metal dichalcogenides [107].

4.4 Supplementary

Background Corrected Transmission Images from Single Layer Graphene

In Fig. 4.6 background corrected transmission images are shown for electron energies ranging from 30 eV down to 18 eV in 1 eV steps. The data shown in Fig. 4.5 was extracted from this series.

Orientation of Brillouin Zone and Background Intensity

In Fig. 4.7 (a) an image displaying first order diffraction disks is shown, which can be used to determine the orientation of the Brillouin zone (see Fig. 4.7 (b)).

In Fig. 4.7 (c) a background intensity image calculated as the average of a series of transmission images recorded at different energies is shown. The individual background corrected transmission images are obtained by dividing the raw data transmission image by the background image.

Angle-resolved Transmission Images from Bilayer Graphene

Preliminary experimental data has been recorded on bilayer graphene as well, in the energy range of 19 eV up to 29 eV, as is shown in Fig. 4.8. A three-fold symmetry is found in the constant energy maps of the transmission function for bilayer graphene at the higher energies, which gradually converts to a more or less six-fold symmetry towards the lower energies. Unfortunately, due to experimental difficulties (very unstable field emission and a serious amount of secondary electrons) the data is not of very good quality. A voltage of -5 V was applied to the entrance of the multichannel plate to block the secondary electrons. This however leads to a small distortion of the electron trajectories, making it difficult to properly transform the data to $\boldsymbol{k}_{\|}$-space. Nevertheless, it was possible to correct for the anisotropic field emission by background correction, at least to some extent. However, some artifacts are present in the background corrected images, as for example the bright features in the top right corner of Fig. 4.8 (f).

The position in $\boldsymbol{k}_{\|}$-space of the six-fold symmetric scattering resonance feature observed for bilayer graphene in Fig. 4.8 (e) and (f) is in agreement with the position of the feature for single layer graphene, as confirmed by comparison with single layer data recorded with the same voltage on the multichannel plate entrance.

On different bilayer graphene sheets no three-fold symmetry is found in the angle-resolved transmission images, rather very similar patterns as for single layer graphene are observed. We therefore conclude that the presence of the three-fold symmetric pattern in the constant energy map of the transmission function of a bilayer graphene sheet depends on the stacking order of the two layers.

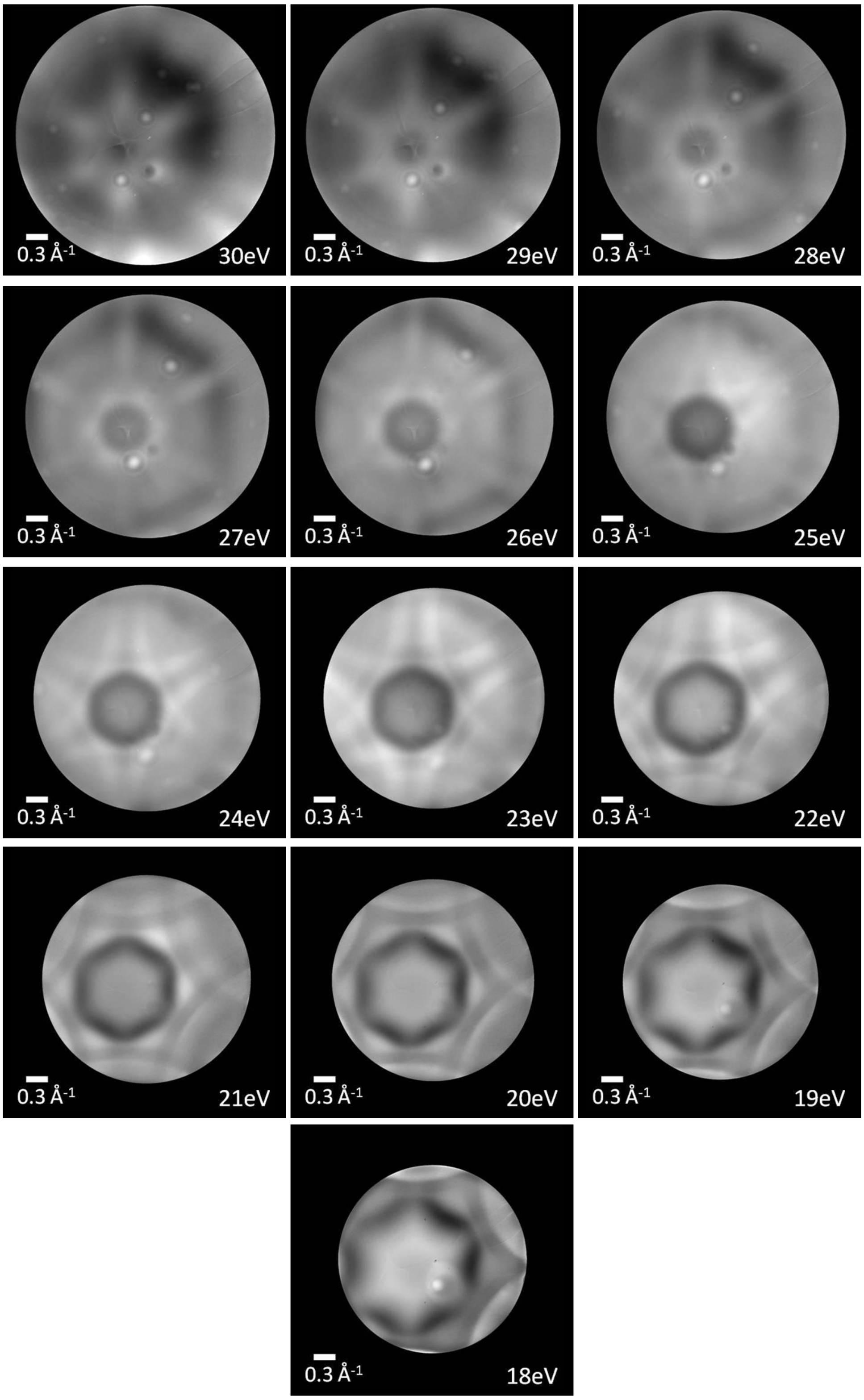

Figure 4.6: Background corrected transmission images for electron energies from 30 eV down to 18 eV in 1 eV steps.

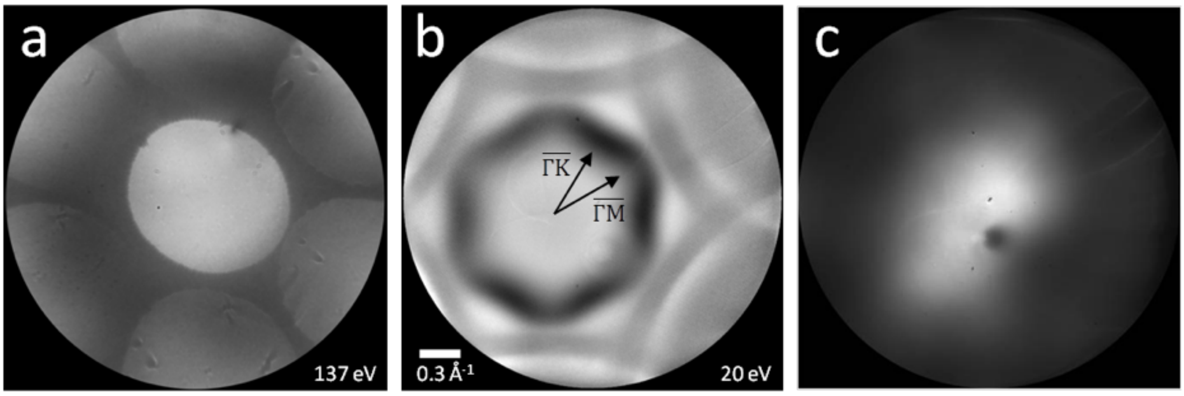

Figure 4.7: **(a)** First order diffraction disk image used to determine the orientation of the Brillouin zone. **(b)** Background corrected transmission image at 20 eV with arrows to indicate the orientation of the Brillouin zone. **(c)** Background intensity calculated as the average of a series of transmission images recorded at different energies.

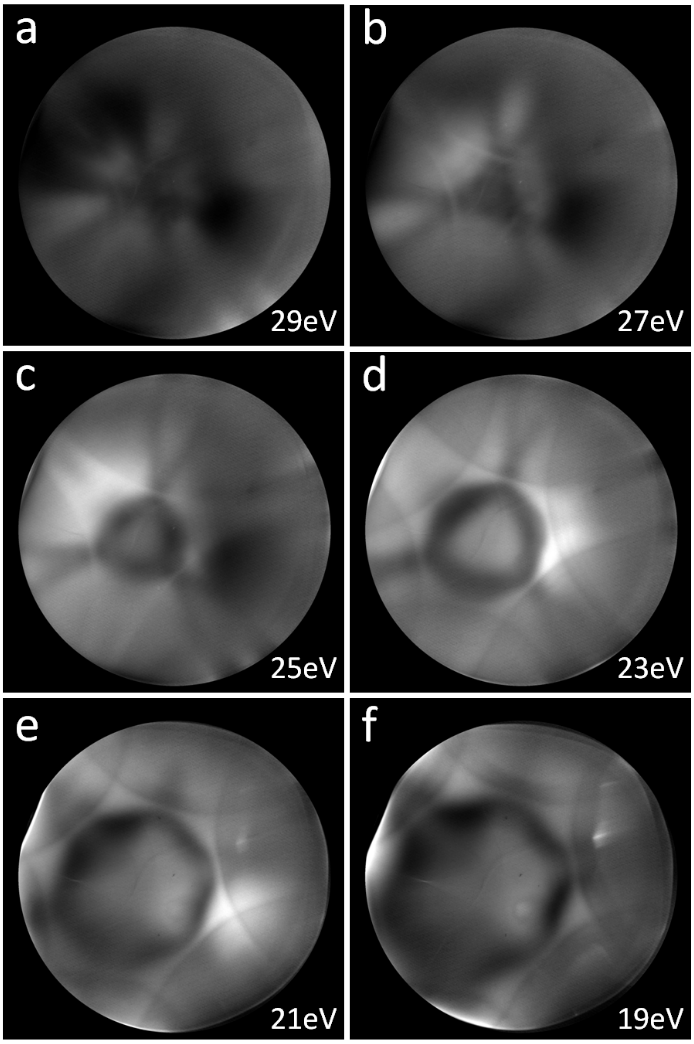

Figure 4.8: Preliminary angle-resolved transmission data recorded on bilayer graphene with electron energies ranging from 29 eV down to 19 eV in 2 eV steps. The data are detector images only, not yet properly scaled to $\boldsymbol{k}_{\|}$-space. A three-fold symmetric pattern is observed in the transmission images recorded at the higher energies, which gradually transforms into a more six-fold symmetric pattern at lower energies. The position in $\boldsymbol{k}_{\|}$-space of the scattering resonance feature observed at 21 eV and 19 eV is in agreement with the position of the feature for single layer graphene.

CHAPTER 5

Direct Observation of Individual Charges and their Dynamics on Graphene by Low-Energy Electron Holography

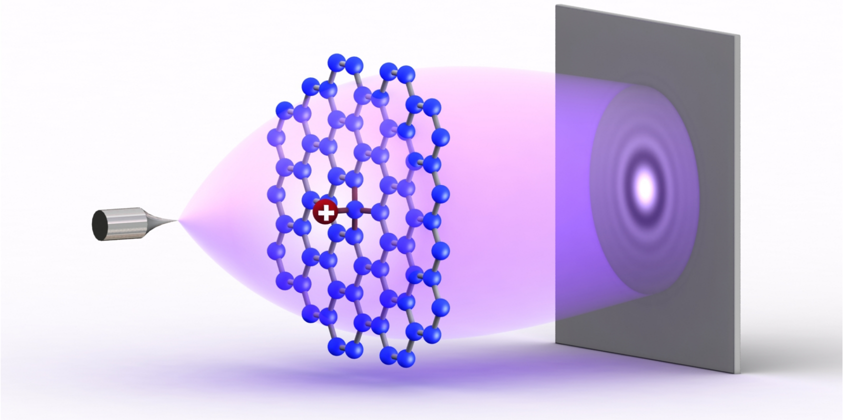

The following chapter contains a modified version of a manuscript accepted by Nano Letters:

T. Latychevskaia, F. Wicki, J.-N. Longchamp, C. Escher, H.-W. Fink, *Direct Observation of Individual Charges by Low-Energy Electron Holography*, Nano Letters, *in press*.

The author of the thesis contributed to the manuscript mostly by experimental work. The simulations and most of the data analysis were performed by Tatiana Latychevskaia.

Abstract

Visualizing individual charges confined to molecules and observing their dynamics with high spatial resolution is a challenge for advancing various fields in science, ranging from mesoscopic physics to electron transfer events in biological molecules. We show here, that the high sensitivity of low-energy electrons to local electric fields can be employed to directly visualize individual charged adsorbates and to study their behavior in a quantitative way. This makes electron holography a unique probing tool for directly visualizing charge distributions with a sensitivity of a fraction of an elementary charge. Moreover, spatial resolution in the nanometer range and fast data acquisition inherent to lens-less low-energy electron holography allows for direct visual inspection of charge transfer processes.

5.1 Introduction

There exist just a few tools, most of them based on scanning probe technologies, that allow for indirect imaging of individual charges [108–110]. Recently, Gatel et al demonstrated that high energy off-axis electron holography can be employed for imaging individual charges by applying contour integration data analysis [111]. We show here that low-energy electron holography can be employed for the direct visualization of individual charges bound to adsorbates on graphene. Graphene is partly transparent to low-energy electrons (30 – 250 eV) [46,47] and can be used as a support for samples [112] to be studied using Low-Energy Electron Point Source (LEEPS) microscopy [22]. Depending on the graphene preparation method, adsorbates of different chemical specificity are present. These individual adsorbates might be light organic molecules stemming from residual solvents [113] or from contamination due to air exposure [114]; possibly also individual C, H or Si atoms [115,116], other possible candidates are metal atoms [117]. Previous studies indicate that there is a charge transfer between graphene and its adsorbates [117]. Depending on the charge transfer direction, the adsorbates represent either a highly localized negatively or positively charged entity on graphene. Density functional theory (DFT) calculations show that almost all metal adatoms transfer electrons to graphene, whereby the transferred charge Δq is typically $-1.6\ e < \Delta q < 0$, where e is the elementary charge [117], except for Au adatoms for which $\Delta q = +0.18\ e$ [118]. Accordingly, most individual metal atoms may constitute highly localized charges on graphene. Furthermore, DFT calculations predict that charge transfer between graphene and adsorbed small molecules can lead to both, negatively or positively charged entities: $\Delta q = -0.025\ e$ for H_2O, $\Delta q = -0.099\ e$ for NO_2, $\Delta q = -0.012\ e$ for CO, $\Delta q = -0.018\ e$ for NO, and $\Delta q = -0.027\ e$ for NH_3 [119]. Electrons of low kinetic energy are sensitive to local variations in the electric potential distribution confined to individual adsorbates on freestanding graphene. We show how individual charges of the order of just one elementary charge associated with the adsorbates on graphene can directly be visualized by low-energy electron holography. And as a consequence also charge transfer processes as well as the diffusion of adsorbates too small for direct observation can be studied.

5.2 Experimental Arrangement

The low-energy electron holographic experimental setup has previously been described in the literature [22] and is shown in Fig. 5.1 (a). A hologram is formed in the detector plane as a result of interference between the wave scattered by the object, and the unscattered (reference) wave [5,120]. The sample can be numerically reconstructed from such a hologram by propagation of the wavefront from the detector plane backwards to the object plane [23]. Ultra-

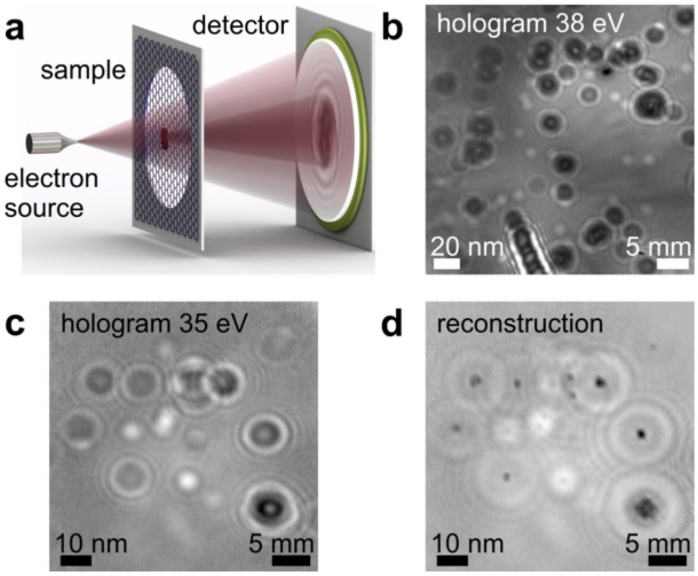

Figure 5.1: Imaging of adsorbates on freestanding graphene by low-energy electron holography. **(a)** Experimental scheme. **(b)** Low-energy electron hologram of adsorbates on graphene acquired with electrons of 38 eV at a tip-to-sample distance of 230 nm, at a resolution of 1.0 nm. **(c)** Another low-energy electron hologram of a graphene sample acquired with electrons of 35 eV at a tip-to-sample distance of 116 nm, at a resolution of 0.8 nm. **(d)** Amplitude reconstruction of the hologram in (c). The source-to-detector distance corresponding to the holograms shown in (b) and (c) is 47 mm. The scale bars indicate the sizes in the object plane (left) and in the detector plane (right).

clean freestanding graphene spanning holes of 2 micrometers in diameter in a Pd/Cr covered silicon nitride membrane is prepared following the procedure described elsewhere [105]. However, if the sample is not transferred into the vacuum chamber fast enough, occasionally small, individual adsorbates are found when investigating freestanding graphene by LEEPS microscopy. Low-energy electron holograms of adsorbates on freestanding graphene are shown in Fig. 5.1 (b) and (c), where a distribution of dark and bright features is apparent. Bright spots, as apparent in Fig. 5.1 (b) and (c), are usually observed even when the graphene samples are carefully prepared. When applying a conventional hologram reconstruction routine [23, 121, 122] to the pattern shown in Fig. 5.1 (c), the dark features converge and reveal well resolved clusters of adsorbates as small as 2 nm in diameter, as shown in Fig. 5.1 (d). In the course of the reconstruction procedure, the object distribution at different source-to-sample distances is calculated and converges towards an in-focus object reconstruction; beyond that distance the object distribution is diverging again. The source-to-sample distance is derived from the position at which the reconstructed objects, as for example clusters, appear in focus. The resolution of the reconstructed objects is determined by a Fourier transformation of the hologram respectively the reconstruction [44], details are provided in the Supporting Information. The concentric interference fringes around the reconstructed objects are due to the so-called twin-image effect which is intrinsic to in-line holography [120, 123]. In contrast to the holograms of the clusters in Fig. 5.1 (c) and (d), the bright spots do not lead to a meaningful object reconstruction but preserve the same blurry appearance at all reconstruction distances.

5.3 Holograms of Individual Localized Charged Adsorbates

Fig. 5.2 (a) depicts a normalized hologram [121,123] where four bright features are observed. The corresponding radial distributions, plotted in Fig. 5.2 (b), show that all four intensity distributions display the first and the second minima at approximately the same radial coordinates. In order to verify the possible origin of the bright features we performed a series of simulations: a hole, a single atom adsorbate and a charged adsorbate, as discussed in the Supporting Information. The simulated holograms of a hole, as well as those of neutral adatoms do not match the experimentally observed holograms, see Fig. 5.8. Simulated holograms of charged adsorbates are shown in Fig. 5.2 (c), the corresponding radial distributions are plotted in Fig. 5.2 (e) and an illustration of the arrangement of a charged adsorbate on the graphene surface is provided in Fig. 5.2 (d). The holograms of $(-e)$ and $(+e)$ exhibit reversed contrast. This distinction is preserved at all studied electron energies: a positive charge results in a bright spot and a negative charge results in a dark spot. Additional simulations are presented in the Supporting Information and Fig. 5.9. All simulated holograms of point charges exhibit the same diameter of the zero-diffraction order and approximately the same position of the minima, in good agreement with the experimental observation, as evident when comparing Fig. 5.2 (e) with Fig. 5.2 (b). In low-energy electron holography, a charged object not only influences the object wave, but also distorts the reference wave, which complicates the interpretation of the object reconstruction [28, 122, 124]. Thus, the fact that the reconstructions of bright features do not converge to meaningful objects can be attributed to the electron wave being diffracted by charged objects. It was also verified that the simulated hologram of a charge leads to a non-meaningful reconstruction. We thus attribute the observed spots in the holograms to small adsorbates carrying positive or negative charges.

5.4 Charged Adsorbates of Opposite Sign

In addition to the spots discussed above, there are spots exhibiting non-rotational symmetric contrast, as apparent for example in the hologram in Fig. 5.3 (a). The observed contrast char-

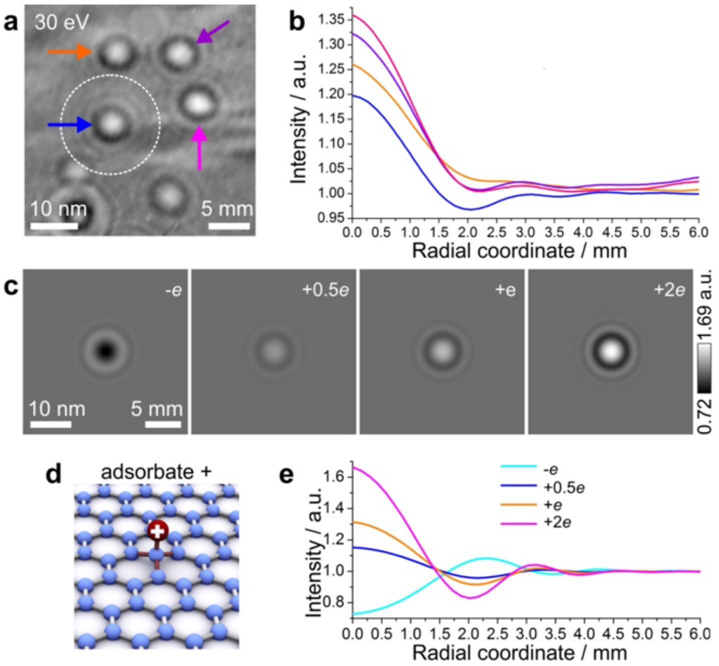

Figure 5.2: Holograms of charged adsorbates. **(a)** A hologram exhibiting bright spots, recorded with 30 eV electrons, at a source-to-detector distance of 47 mm and a source-to-sample distance of 82 nm, at a resolution of 0.6 nm. **(b)** Intensity profiles corresponding to the four bright spots marked in (a) averaged over the angular coordinate as a function of the radial coordinate counted from the centre of the spot. The intensity distribution range extends out to 6 mm on the detector corresponding to the radius of the dashed circle indicated in (a). **(c)** Simulated holograms of a point charge of four different charge values at an electron energy of 30 eV at a source-to-detector distance of 47 mm and a source-to-sample distance of 82 nm. **(d)** Schematic representation of a charged adsorbate on graphene. **(e)** The angular averaged intensity profiles as a function of the radial coordinate calculated from the simulated holograms shown in (c). The scale bars in (a) and (c) indicate the sizes in the object plane (left) and in the detector plane (right)

acteristics are in compliance with the ones arising in simulations concerning two oppositely charged adsorbates in close proximity as illustrated in Fig. 5.3 (c). Note that the spot in the right bottom corner in Fig. 5.3 (a) suddenly turns into a regular bright spot, indicating that the negative charge has vanished, while the positive charge is still present. For this very spot, the distance between the two charges, estimated from the distance between the centers of the two sets of the concentric rings, as shown in Fig. 5.3 (b), amounts to 1.4 ± 0.8 nm. The simulated holograms of two charges, $+0.7\ e$ and $-0.7\ e$, separated by 0.5 nm, 1 nm, 1.5 nm and 2 nm are shown in Fig. 5.3 (c). From the fitting of the radial intensity curve of the hologram

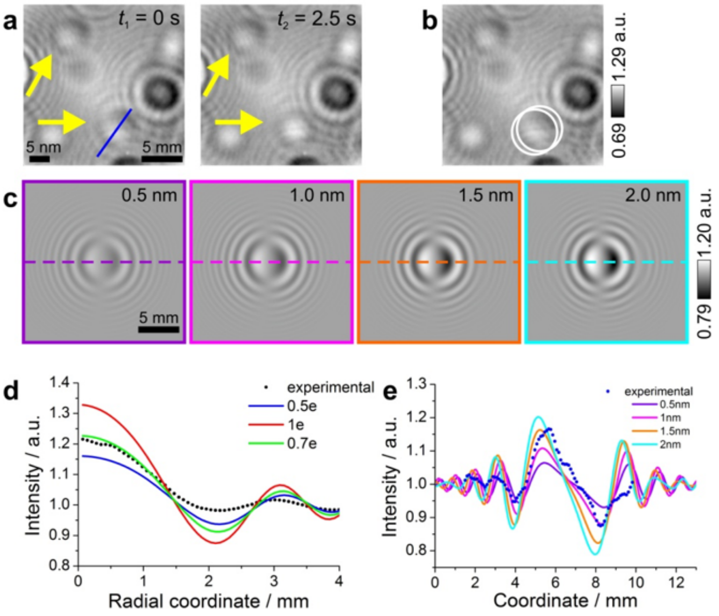

Figure 5.3: Charges of opposite sign. **(a)** Experimental hologram recorded with 30 eV electrons, at a source-to-detector distance of 47 mm and a source-to-sample distance of 95 nm, at a resolution of 0.5 nm. Two spots with gradient contrast, attributed to a positive charge on the left and a negative charge on the right side, are indicated by the yellow arrows, and the hologram acquired 2.5 s later is showing that the spot of former gradient contrast at the bottom right has turned into a bright spot. **(b)** The same hologram as in (a, left), but with white circles to denote the difference in position of the positive and negative charges. **(c)** Simulated holograms of two charges, $+0.7\ e$ (left) and $-0.7\ e$ (right) separated by 0.5 nm, 1.0 nm, 1.5 nm and 2.0 nm. In the simulations the source-to-detector distance is 47 nm and the source-to-sample distance is 95 nm. **(d)** The averaged radial intensity profiles of the bright spot at the bottom right in the experimental hologram (a, right) and that of the related simulated holograms of a positive charge of 0.5 e , 0.7 e and 1 e. **(e)** The intensity profiles through the experimental (a, left) and simulated (c) holograms along the colored lines.

of the remaining positive charge, as illustrated in Fig. 5.3 (d), we estimate the charge to be $+0.7 \pm 0.2\ e$. The comparison with the profiles of the simulated holograms of two separated charges, shown in Fig. 5.3 (e), leads to a distance of 1.5 ± 0.5 nm between the charges.

5.5 Charge Transfer Dynamics of Charged Adsorbates

Under continuous observation by low-energy electrons, the bright spots exhibit intensity dynamics: blinking, complete disappearance as well as reversal of the contrast from bright to dark and inversely. We observed such intensity dynamics at different electron energies, ranging from 30 eV to 129 eV and currents between 10 nA and 500 nA. An example is shown in Fig. 5.4 where the intensity maxima for all three bright spots marked in the hologram in Fig. 5.4 (a), show the same value of about 1.19 a.u., see plot in Fig. 5.4 (b). The spots also exhibit an intermediate intensity at about a.u. that we define as neutral state; at this intensity the spots can no longer be distinguished from the background. One of the spots (see spot 1 in Fig. 5.4 (b)) displays an inversion of its contrast from bright to dark with a minimum of the intensity at about 0.9 a.u., as shown in Fig. 5.4 (c) at the frame $t = 180$ s. The experimental observations of features changing their contrast from bright to dark can be attributed to a change in the charged state, while a vanishing contrast is attributed to a neutral state of an adsorbate too small to be resolved. These transitions between the states can either be caused by a charge re-distribution between adsorbate and graphene, by the impact of an imaging electron or by phonon scattering. We estimate an electron current density of $1.56 \cdot 10^6$ $\mathrm{e}/(\mathrm{s} \cdot \mathrm{nm}^2)$ for a total emission current of 10 nA. This amounts to about $2.40 \cdot 104$ e/s for a circle with a radius of 70 pm occupied by a carbon atom. However, we found no correlation between the variation of the intensity of the illuminating electron beam and the dynamics of the change in the charge state for a selected spot, as discussed in the Supporting Information.

The charged adsorbates exhibit different intensity fluctuation characteristics. Some adsorbates remain positively charged over long time with occasional transitions to neutral and negatively charged states while others turn into a stable negatively charged state. The intensity of one of the spots, marked by a blue circle in Fig. 5.4 (d), has been investigated in more detail. 15083 frames were acquired at a frame rate of 60 fps. The intensity of the spot as a function of the frame number is shown in Fig. 5.4 (e). The total number of frames in each of the three states are: $N_{-1} = 985$, $N_0 = 1310$ and $N_{+1} = 12788$, and the related total time durations in each state are: $T_{-1} = 16.42$ s, $T_0 = 21.83$ s and $T_{+1} = 213.13$ s, where -1, 0 and $+1$ are negatively charged, neutral and positively charged states, accordingly. This translates into the probabilities of finding the adsorbate in a selected state: $p_{-1} = 0.065$, $p_0 = 0.087$ and $p_{+1} = 0.848$. To get a first, albeit still rough, idea about the energetics involved, in using the formula for the ratio of probabilities $p_i/p_j = \exp\left((E_j - E_i)/k_B T\right)$, where E_i is the energy of state i, and k_B denotes the Boltzmann constant, we estimate the free energy differences for the three states: $E_0 - E_{+1} = 59$ meV and $E_{-1} - E_0 = 7$ meV.

This however assumes that the population of each state is representative for the distribution under ordinary thermal equilibrium, not affected by the kinetics of the transitions. To be on the safe side, we also computed the population distribution by taking only every 50^{th} frame into account. In this way we ensure that the system has had a chance to frequently change its state during this elongated time interval before every 50^{th} frame is used to probe its configuration. This analysis leads to: $N_{-1} = 21$, $N_0 = 27$ and $N_{+1} = 254$ with the

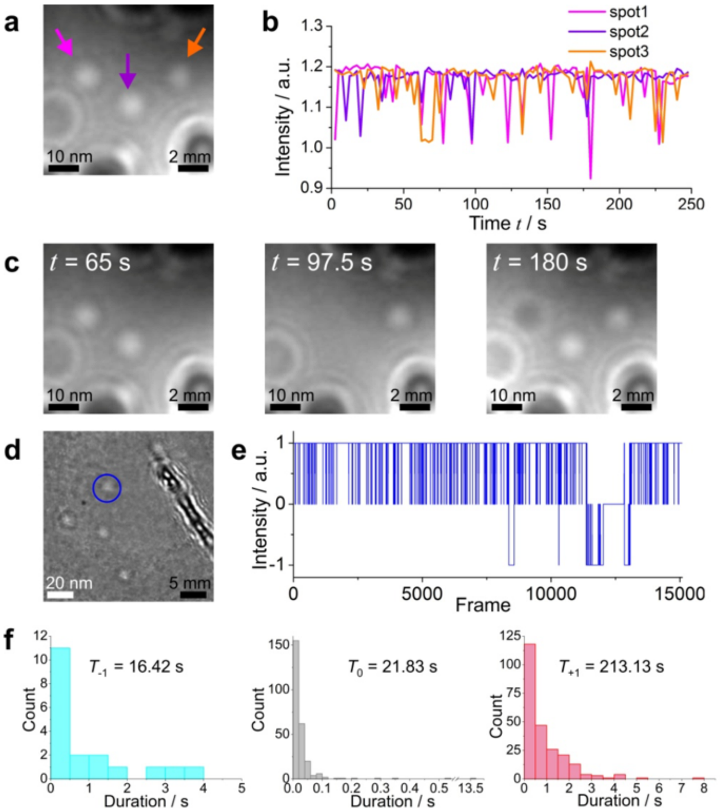

Figure 5.4: Intensity dynamics of bright features in holograms. **(a)** A hologram exhibiting spots acquired with 38 eV energy electrons at a source-to-detector distance of 47 mm and a source-to-sample distance of 235 nm, at a resolution of 1.7 nm. **(b)** Maximal intensity as a function of time for each of the three bright spots marked in (a). A total of 99 frames were acquired during 247.5 s. **(c)** Region of interest recorded at different times. **(d)** A selected region in a hologram acquired with 129 eV energy at a source-to-detector distance of 70 mm and a source-to-sample distance of 280 nm, at a resolution of 1.3 nm. **(e)** Relative intensity at the spot shown in the blue circle in (d) as a function of frame number. **(f)** Three histograms showing the counts for negative, neutral and positive states of the selected spot. The scale bars in (a), (c) and (d) indicate the sizes in the object plane (left) and in the detector plane (right).

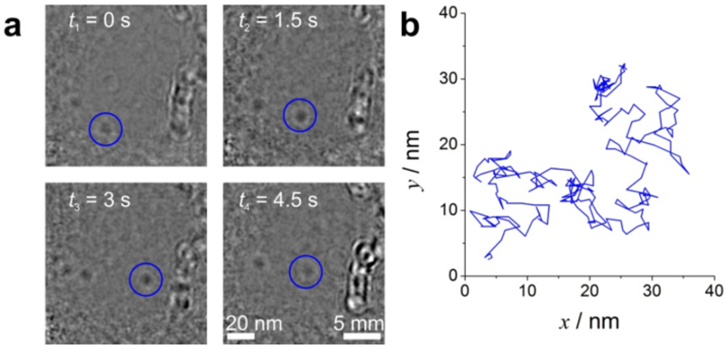

Figure 5.5: Mobility of adsorbates on graphene. Holograms were recorded with 125 eV electrons, at a source-to-detector distance of 70 mm and a source-to-sample distance of 380 nm, at a resolution of 1.7 nm. **(a)** Four contrast-enhanced holograms from a series of holograms showing the motion of a negatively charged adsorbate on graphene. The scale bars indicate the sizes in the object plane (left) and in the detector plane (right). **(b)** Trajectory of the adsorbate marked with blue circles in (a), followed over a duration of 4.5 s.

corresponding probabilities: $p_{-1} = 0.065$, $p_0 = 0.089$ and $p_{+1} = 0.841$ leading to: $E_0 - E_{+1} = 58 \pm 7$ meV and $E_{-1} - E_0 = 6 \pm 2$ meV, values that are comparable to the ones above within the statistical errors given by the square root of the number of observations. However, these values should so far only be taken as an order of magnitude of the energetics involved.

5.6 Mobility of Charged Adsorbates

In the following we take advantage of the enhanced holographic contrast of a charged object that enables tracking of entities too small to be detected otherwise. Adatoms are adsorbed at distinct sites on graphene, and they can migrate until they find an energetically favorable site [125]. DFT calculations show that most chemical elements, including Al, Si, Pt, Pd, Au, Cu and others have a diffusion barrier energy less than 0.4 eV and several elements such as V, Cr, Mn, Fe Co, Mo and Ru have a diffusion barrier energy higher than 0.4 eV [126]. The diffusion barrier energies of Au, Cr, and Al adatoms on pristine monolayer, bilayer and trilayer graphene were found to be of the order of $k_B T$ at room temperature (25.7 meV) or even smaller [127]. This implies that adatoms of most chemical elements can easily and quickly migrate across the graphene lattice before they bind to an energetically favorable site. Hardcastle et al. [127] performed scanning transmission electron microscopy (STEM) on graphene samples and they speculated that all metal adatoms are highly mobile on graphene, but that they all migrated to stable sites before the samples were characterized in the microscope. We also observed that the positively charged adsorbates, represented by bright spots in the hologram, exhibit some mobility on the graphene but only in the first few seconds during the exposure to the low-energy electron beam. Afterwards no movement of the bright spots was observed. However, the negatively charged adsorbates, represented by dark spots in the hologram, often carry out a random walk during the electron exposure, as for example illustrated in Fig. 5.5. For a selected adsorbate shown in Fig. 5.5 (a), its random walk, shown in Fig. 5.5 (b), is characterized by the mean squared displacement: $\overline{r^2} = \frac{1}{N}\sum_{i=1}^{N-1}[(x_{i+1} - x_i)^2 + (y_{i+1} - y_i)^2] = 3.33 \pm 0.17\ \mathrm{nm}^2$, where N is the number of frames $N = 271$ acquired at a time interval $\Delta t = 1/60\ \mathrm{s} = 0.0167\ \mathrm{s}$ for a total time of 4.5 s, and (x_i, y_i) are the adsorbate coordinates at frame i. This leads to a diffusion coefficient of $D = \overline{r^2}/(4\Delta t) = 50.0 \pm 2.6\ \mathrm{nm}^2/\mathrm{s}$.

5.7 Conclusions

We have shown that the high sensitivity of low-energy electrons to local electric fields can be employed to directly visualize charge distributions with a sensitivity of a fraction of an elementary charge carried by adsorbates on freestanding graphene and to quantitatively study their behavior. By means of low-energy electron holography we were able to observe charge transfer processes. While positively charged states are found to be the most frequently observed ones, adsorbates are also occasionally neutralized or are undergoing a transition to a negatively charged state with a comparably short life-time. Pairs of two oppositely charged adsorbates separated by a distance in the order of one nanometer were also found, and for a selected pair of such charges the estimated distance amounts to 1.5 nm. Charged adsorbates, mainly those carrying a negative charge, perform a random walk on freestanding graphene. Although adsorbates are known to quickly occupy some stable sites on graphene, we were able to observe their random walk behavior on graphene before they were finally trapped.

5.8 Supplementary Material

Resolution Estimation

The resolution with which an object is reconstructed from its hologram can be estimated from the Fourier spectrum of the hologram or the reconstructed object [44]. We define the maximal frequency in the spectrum k_{max} as the frequency where the peaks of the spectrum are still distinguishable from noise, as illustrated in Fig. 5.6. The resolution is then given by $R = 2\pi/k_{max}$. The spectrum of the hologram shown in Fig. 5.1 (b) is displayed in Fig. 5.6; with values $k_{max} = 6.15\ \text{nm}^{-1}$ and $R = 1.0$ nm.

Calculation of the Transmission Function for Simulating the Hologram of a Point Charge

The electric potential distribution of a point-like charge q in free space is given by:

$$\varphi(r) = \frac{q}{4\pi\varepsilon_0}\frac{1}{r} \tag{5.1}$$

and the corresponding electric field distribution is found as:

$$\vec{E}(r) = -\text{grad}\varphi(r) = \frac{q}{4\pi\varepsilon_0}\frac{1}{r^2}\vec{e}_r, \tag{5.2}$$

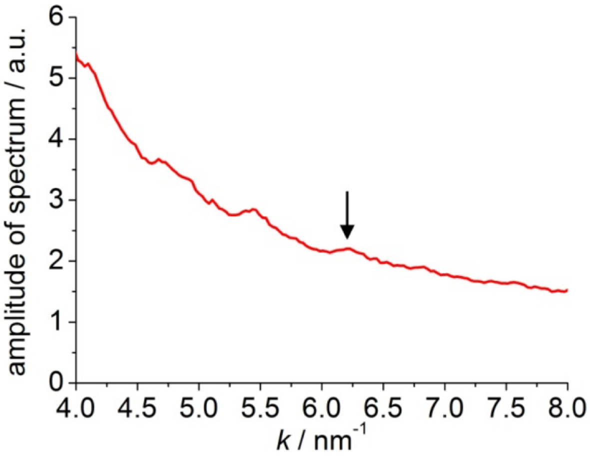

Figure 5.6: Resolution estimation. Radial distribution of the amplitude of the Fourier spectrum of a hologram $\mathcal{F}(H(x_d, y_d))$ as function of the Fourier domain coordinate k . The arrow indicates k_{max} .

where ε_0 is the vacuum permittivity, r is the distance from the charge and $\vec{e}_r$ is the unit vector in the spherical coordinate system.

The movement of an electron is described by the equation:

$$m\ddot{\vec{r}} = -e\vec{E}(r), \tag{5.3}$$

where e is the elementary charge and m is the mass of the electron.

We are only interested in the (x, z)-projection due to the rotational symmetry around the z-axis. We consider the electron moving parallel to the z-axis at a speed v_0.

For infinitesimal small Δx and Δz, equations for x and z coordinates are:

$$\begin{aligned} \tfrac{\Delta v_x}{\Delta t} &= -\tfrac{e}{m}E_x(x,y,z) \\ \tfrac{\Delta v_z}{\Delta t} &= -\tfrac{e}{m}E_z(x,y,z), \end{aligned} \tag{5.4}$$

or

$$\begin{aligned} \Delta v_x &= -\tfrac{e}{m}E_x(x,y,z)\Delta t \\ \Delta v_z &= -\tfrac{e}{m}E_z(x,y,z)\Delta t. \end{aligned} \tag{5.5}$$

Since the velocity in the x-direction can be expressed as:

$$v_x = v_{ox} + \Delta v_x \tag{5.6}$$

where $v_{ox} = 0$, we can re-write Equation 5.5:

$$\begin{aligned} v_x &= -\tfrac{e}{m}E_x(x,y,z)\Delta t \\ v_z &= -\tfrac{e}{m}E_z(x,y,z)\Delta t + v_0 \approx v_0, \end{aligned} \tag{5.7}$$

where the approximation in Equation 5.7 can be applied since at an electron energy of 30eV the following expression holds: max $\left|\tfrac{e}{m}E_z(x,y,z)\Delta t\right| \approx 0.022v_0$. By solving the last equations for coordinates, we obtain:

$$\begin{aligned} \tfrac{\Delta x}{\Delta t} &= -\tfrac{e}{m}E_x(x,y,z)\Delta t \\ \tfrac{\Delta z}{\Delta t} &\approx v_0. \end{aligned} \tag{5.8}$$

or

$$\begin{aligned} &\Delta x = -\tfrac{e}{m} E_x(x,y,z)(\Delta t)^2 \\ &\Delta t \approx \tfrac{\Delta z}{v_0}. \end{aligned} \tag{5.9}$$

By substituting Δt into the expression for Δx, we obtain:

$$\Delta x = -\frac{e}{m} E_x(x,y,z)\left(\frac{\Delta z}{v_0}\right)^2. \tag{5.10}$$

The deflection of an electron passing the electric field can then be expressed as:

$$\gamma(x) = \frac{\Delta x}{\Delta z} = -\frac{e}{m v_0^2} E_x(x,y,z)\Delta z, \tag{5.11}$$

$E_x(x,y,z)$ is calculated as:

$$E_x(x,y,z) = \frac{q}{4\pi\varepsilon_0} \frac{x}{(x^2+y^2+z^2)^{3/2}}. \tag{5.12}$$

Next, we simplify the z-dependency of the electric field distribution by replacing it with the distribution at the fixed z-coordinate where the point-like charge is located ($z = 0$):

$$E_x(x,y,z) = \frac{q}{4\pi\varepsilon_0} \frac{1}{x^2}. \tag{5.13}$$

By substituting Equation 5.13 into Equation 5.11, we obtain:

$$\tan(\gamma(x)) = -\frac{e}{m v_0^2} \frac{q}{4\pi\varepsilon_0} \frac{1}{x^2} \Delta z \tag{5.14}$$

The deflection of an electron is maximal when it passes the charge in close proximity. Therefore we consider a distance a of a few Ångstrom as a reasonable approximation for the interaction region, see Fig. 5.7.

We set $\Delta z = 2a$, which provides

$$\gamma(x) = \alpha(x) \arctan\left(\frac{e}{m v_0^2} \frac{q}{4\pi\varepsilon_0} \frac{2a}{x^2}\right), \tag{5.15}$$

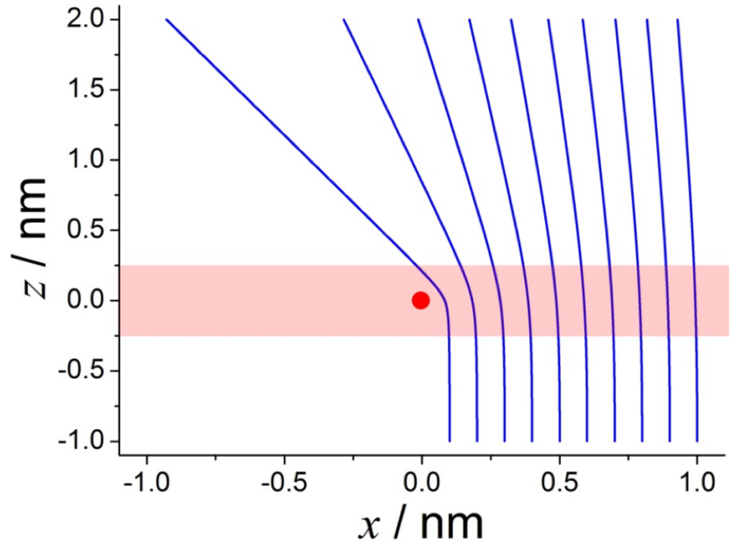

Figure 5.7: Simulated trajectories for 30 eV electrons passing a positive charge e. The region marked exhibits a height of $2a = 5$ Å.

whereby $\alpha(x) = 1$ for $x < 0$ and $\alpha(x) = -1$ for $x > 0$. The total phase shift introduced into an electron wave can be represented as a phase shift in the object plane:

$$\Delta\chi(x) = -\frac{2\pi}{\lambda}\left|\gamma(x)\right|\left|x\right| \approx -\frac{2\pi}{\lambda}\frac{e}{mv_0^2}\frac{q}{4\pi\varepsilon_0}\frac{2a}{|x|} \tag{5.16}$$

We set $2a = 5$ Å as shown in Fig. 5.7, as the region where significant bending of the electron trajectories occurs.

The total transmission function in the object plane is then given by:

$$T(x,y) = \exp(-A(x,y))\exp(i\Delta\chi(x,y)), \tag{5.17}$$

whereby $A(x,y)$ is the absorption distribution. For a single point-like charge we assume zero absorption and thus $\exp(-A(x,y)) = 1$.

Simulated Holograms of Holes in and Adatoms on Graphene

Holes

A hole, a prominent defect in graphene, is illustrated in Fig. 5.8 (a). It was simulated as a fully transparent region in a sheet exhibiting a complex-valued transmission function which takes scattering off carbon atoms into account:

$$T(x,y) = 1 - g(x_i,y_i) + \alpha g(x_i,y_i) f(\vartheta) e^{i\varphi(\vartheta)}, \tag{5.18}$$

where $g(x_i,y_i)$ is 1 at the position (x_i,y_i) of carbon atom i and 0 elsewhere, α represents the fraction of elastically scattered electrons, $f(\vartheta)$ is the amplitude of the scattered wave and $\varphi(\vartheta)$ is the phase of the scattered wave. The phase shifts for the simulation are taken from the NIST library [128] and for 50 eV electrons we obtain: $f(\vartheta = 0) = 7.389$ and $\varphi(\vartheta = 0) = 0.725$ rad.

In the absence of the graphene patch, $T(x,y) = 1$, and a wave which passes through the aperture is described in the detector plane as $U_0(X,Y)$.

With graphene being present, the incoming wave is partly absorbed by graphene

$$T(x,y) = 1 - g(x_i,y_i) \tag{5.19}$$

where $G(x_i,y_i)$ is 1 at the position (x_i,y_i) of carbon atom i and 0 elsewhere. A wave passing through an aperture in graphene is thus described in the detector plane as $U_0(X,Y) - U_G(X,Y)$.

By taking the absorption as well as the forward scattering of carbon atoms into account, we obtain:

$$T(x,y) \approx 1 - g(x_i,y_i) + \alpha g(x_i,y_i) f(0) e^{i\varphi(0)}, \tag{5.20}$$

and the wave in the detector plane is approximately described by

$$U_0(X,Y) - U_G(X,Y) + \alpha G(X,Y) f(0) e^{i\varphi(0)}, \tag{5.21}$$

where $f(0)$ denotes the amplitude and $\varphi(0)$ the phase of the scattered wave in forward direction, and $G(X,Y)$ is the complex-valued distribution describing the wave scattered by graphene described by $g(x_i,y_i)$.

Since a transmission of 73 % was measured for low-energy electrons through graphene [47], we simulated the situation with 50 eV electrons passing through a 40 nm in diameter patch of graphene. Under such condition, we found that the intensity of the transmitted wave amounts to 73 % of the initial intensity when $\alpha = 0.073$. With these parameters, the transmission function of graphene given by Equation 5.18 was simplified to $T(x,y) = 0.856e^{0.105i}$. Thus, in the simulation graphene is described as a sheet exhibiting the complex-valued transmission function $T(x,y) = 0.856e^{0.105i}$ containing a hole.

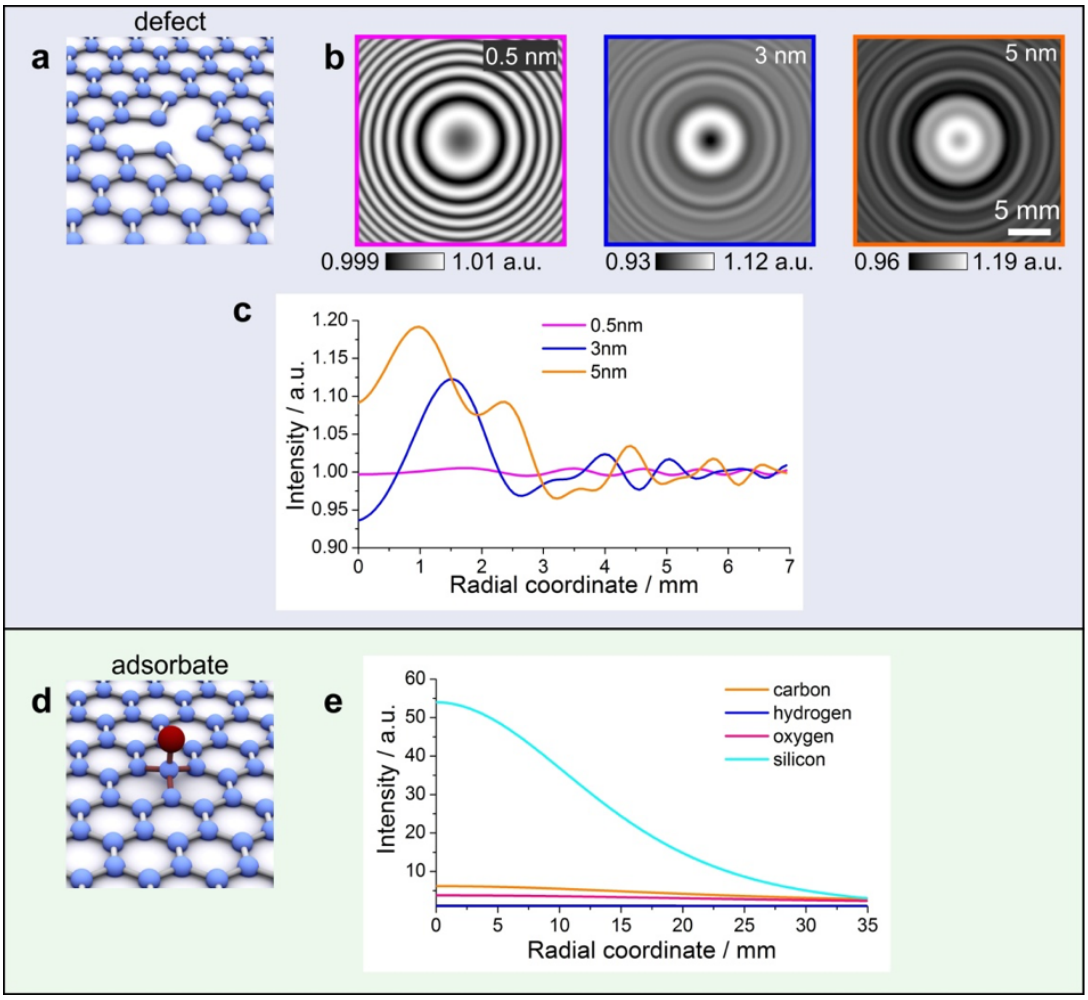

Figure 5.8: Simulated holograms of holes in graphene and adatoms on graphene. **(a)** Artistic representation of a hole in graphene. **(b)** Simulated holograms of holes of different diameter in a graphene sheet. **(c)** Angular averaged intensity profiles as a function of the radial coordinate calculated from the simulated holograms shown in (b). **(d)** Artistic representation of a single atom adsorbate on graphene. **(e)** Angular averaged intensity profiles as a function of the radial coordinate calculated from the distribution of the intensity of the 50 eV electron wave scattered off individual atoms. In the simulations, the electron energy amounts to 50 eV, the source-to-detector distance to 47 mm and the source-to-sample distance to 82 nm.

Fig. 5.8 (b) shows the central 200 × 200 pixels region of the simulated holograms for holes of 0.5, 3 and 5 nm in diameter. The holograms are normalized by division with the background formed by the wave passing through a defect-free graphene sheet. Fig. 5.8 (c) shows the corresponding radial intensity profiles. The following conclusions can be drawn from the data shown in Fig. 5.8 (b) and (c): (1) For any hole exhibiting a diameter of a few times the wavelength there is a decrease of intensity in the centre of the hologram. Such decrease was experimentally not observed in the centre of the bright spots. (2) The holograms of holes with larger diameter exhibit a relatively high intensity in the centre displaying values close to the experimentally observed intensity. (3) The holograms of holes with larger diameter show a pronounced first minimum and its radial position is close to the radial position of the first minimum observed within the bright features of the experimental holograms.

Single Atoms on Graphene

Here, we simulate a situation where a coherent low-energy electron wave is scattered off a single atom on graphene, as illustrated in Fig. 5.8 (d) by accounting for the anisotropic scattering typical for low-energy electrons. We selected a few adsorbate atoms which can typically be found on graphene: carbon, hydrogen, oxygen and silicon. The complex-valued amplitudes of the scattered electron wave were constructed using the partial wave expansion [129, 130], whereby the phase shifts were provided by the NIST library [128]. The electron energy was selected to be 50 eV, the lowest energy for which the NIST library provides the phase shifts and representative for the experimental energy range. The simulation resulted in the complex-valued wave U_0 originating from a point-like source. To create a more realistic distribution for a single atom a Gaussian-like distribution was imposed such that its full width at half maxima equals twice the empiric covalent radii (70 pm for carbon, 25 pm for hydrogen, 60 pm for oxygen and 110 pm for silicon). The complex-valued wave at the detector was obtained by a convolution of U_0 with the atom distribution. Next, a reference wave with an amplitude equal to the maximum of the amplitude of a wave scattered by a carbon atom was superimposed and the hologram computed as the squared absolute value of the result.

It is evident that for all waves scattered off individual atoms, the intensity distribution is broad, not exhibiting a pronounced peak within the detector area. The scattering off an individual atom thus contributes to the featureless background only, while a pronounced peak can only be observed for a charged adsorbate. Thus, we can exclude that a single atom is the cause for the bright spots observed in the experimental holograms.

Simulated Holograms of Charges at Different Electron Energies

In the simulated holograms of charges at different electron energies shown in Fig. 5.9 (a) and (b), a positive charge results in a bright spot and a negative charge results in a dark spot and this contrast is preserved at all electron energies. It can be seen from Fig. 5.9 (c) that the positions of the first minima are found at smaller radial coordinates when the energy of the electrons is increased. A higher electron energy and thus shorter wavelength leads to a downscaled pattern, as also apparent in the holograms in Fig. 5.9 (a) and (b). It should

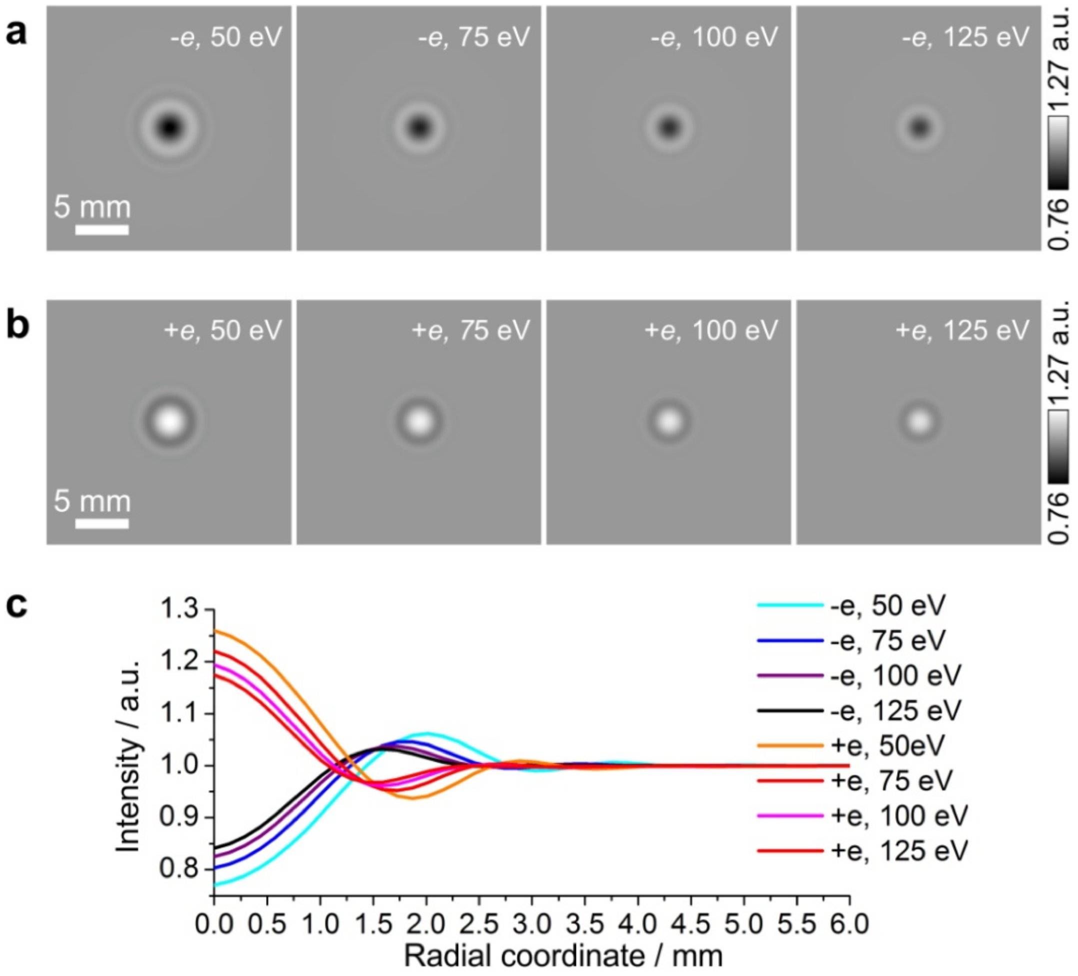

Figure 5.9: Simulated holograms of charges at different energies. **(a)** Holograms of a negative charge. **(b)** Holograms of a positive charge. **(c)** Angular averaged intensity profiles as a function of the radial coordinate. In all simulations, in order to match the experimental conditions, we set the source-to-sample distance to 82 nm and the source-to-detector distance to 47 mm.

also be noted that the amplitude of the zero-order diffraction spot varies with the electron wavelength as well. Thus, for a quantitative estimation of the charge value, the precise energy of the imaging electrons must be known.

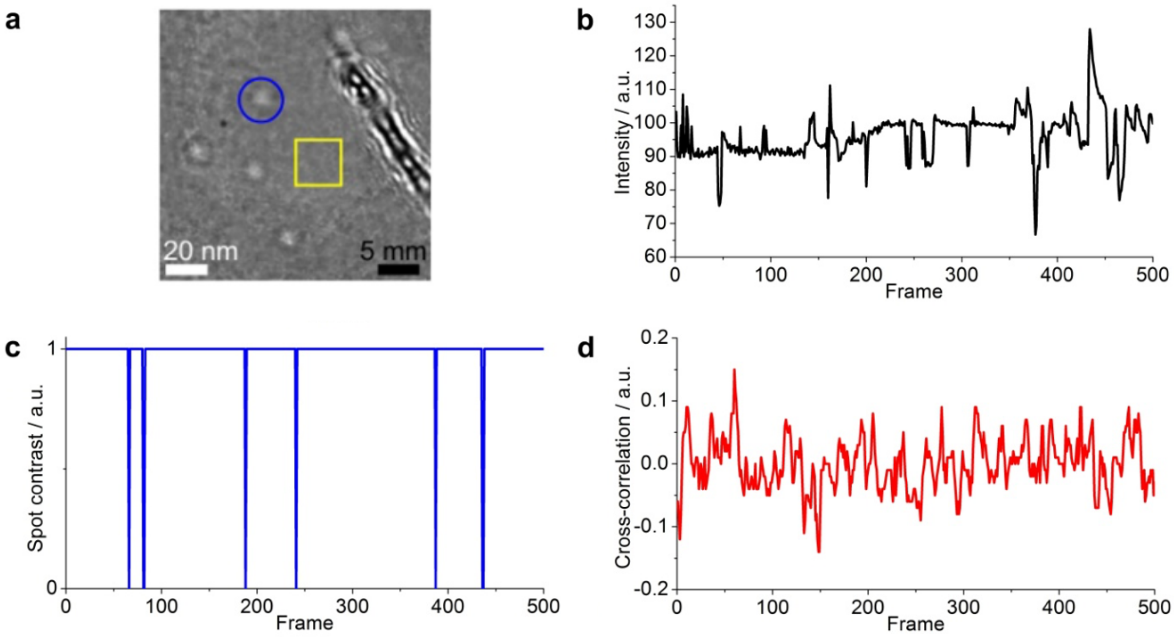

Figure 5.10: Cross-correlation between the electron bean intensity and the contrast of a selected spot. **(a)** A selected spot in the hologram indicated by the blue circle. The selected region for to evaluate beam intensity fluctuations is indicated by the yellow square. Frames were acquired with 129 eV energy at a source-to-detector distance of 70 mm and the source-to-sample distance of 280 nm. The scale bars in (a) indicate the sizes in the object plane (left) and in the detector plane (right). **(b)** Intensity as a function of frame number. **(c)** Contrast of a selected spot as a function of frame number. **(d)** Cross-correlation between the signals shown in (a) and (b).

Cross-Correlation Between the Electron Beam Intensity and the Contrast of a Selected Spot

To evaluate the cross-correlation between the contrast of a selected spot at the detector and the intensity of the electron beam, we estimated the averaged intensity at a region nearby the spot, as shown in Fig. 5.10 (a). The intensity of the illuminating electron beam as a function of frame number for the first 500 frames is shown in Fig. 5.10 (b). It displays a mean value of 96.0 a.u with a standard deviation of 4.9 a.u.. The time evolution of the contrast of a selected spot, shown in Fig. 5.10 (c). The spot is observed bright most of the time corresponding to a positive charge with a few transitions to the neutral state. The cross-correlation between the intensity of the illuminating beam and the contrast of the selected spot is shown in Fig. 5.10 (d), and indicates no correlation between the two signals.

CHAPTER 6

Conclusions and Outlook

Four novel electron point source applications were developed in the course of this thesis.

A miniaturized electron column comprising two electrostatic lens elements was designed and fabricated. A micro-lens is employed as beam limiting aperture and the extractor for field emission from an electron point source and is used to prefocus the electron beam. Subsequently, a three-electrode mini-lens element shapes the electron beam to its final form. The formation of a nearly parallel beam of 100 eV electrons with a residual minimal half divergence angle of 2 mrad was demonstrated experimentally. The dual lens system allows to accelerate or decelerate the electrons within the column by biasing the source/micro-lens ensemble with respect to the sample potential and a parallel beam is shaped by adjusting the focusing potential on the mini-lens accordingly. This gives access to final beam energies ranging from a few eV up to more than 1 keV. This aspect is very beneficial for coherent diffraction imaging applications: a coherent parallel electron beam of tunable energy allows adjusting the spatial resolution contained in the diffraction record without reconditioning the acceptance angle of the detector unit.

The second half of the Phd concerned setting up an instrument merging LEEPS microscopy and SPM. This involved the implementation of a piezo tube scanner, a new high numerical aperture detector system to acquire LEEPS images and a complete SPM control system. The new instrument allows to consecutively image the same sample region in LEEPS mode and field emission SPM (FESPM) mode. Two current-to-voltage amplifiers allow to measure simultaneously the current emitted by the electron point source I_E and the current absorbed by the sample I_A. Both current signals can be used as contrast signal and feedback parameter in absorption contrast FESPM (AC-FESPM). Moreover, the relative absorption $A_r = I_A/I_E$ serves as a robust contrast signal, which allows to effectively avoid image distortions due to abrupt changes in the field emission performance of the tip.

The new system also allows to modify the field emitter tip such that it emits at lower bias voltages with an enlarged emission angle: In a feedback-controlled tip crash procedure, the tip is approached to a freestanding graphene sample until the graphene sheet breaks locally. It is speculated that during such a process a small graphene flake occasionally attaches to the tip and builds an elongated protrusion, from which the field emission occurs afterwards. Further insight could be achieved by studying such a tip by high resolution transmission electron microscopy or field ion microscopy.

With the improvements of the new experimental setup, ultra-low-energy electron holograms of clusters on freestanding graphene were acquired, featuring high interference contrast, tip-to-sample distances below 50 nm, electron energies as low as 20 eV and sub-nanometer resolution. The LEEPS/SPM instrument shall eventually also allow to perform STM imaging on freestanding graphene samples, giving access to electron energies below the work function of the sample and possibly atomic resolution. First STM measurements were performed on rigid substrates, but additional improvements of the experimental setup will be needed to study freestanding graphene.

The possibility to operate the electron point source at very low electron energy in the new LEEPS/SPM system leads to the development of a completely new application of LEEPS microscopy: Mapping unoccupied electronic states by angle-resolved electron transmission. A strong angular dependence of the electron transmission is observed when lowering the electron energy in LEEPS imaging of a freestanding graphene sheet to about 30 eV and below. As the in-plane momentum of an electron depends on its probing angle, a single LEEPS measurement corresponds to a constant energy map in the transmission function $T(\boldsymbol{k}_{\|}, E)$. This allows to probe unoccupied states in all directions of the Brillouin zone at once, as the transmission reflects the coupling of the probing electrons to electronic states in the sample. Regarding their position in energy and in-plane momentum space, the observed characteristics are in good agreement with ab-initio calculations of the transmission function along the high symmetry axes $\overline{\Gamma M}$ and $\overline{\Gamma K}$ in the Brillouin zone [84]. A predicted scattering resonance is clearly identified in the experimental data. Deviations of the measured relative transmission intensities from the calculations are attributed to inelastic effects, not taken into account in the ab-initio calculations. The experimental findings could thus be used as a reference for future ab-initio calculations, where inelastic effects might be included by an imaginary potential in the Hamiltonian of the scattering region [131]. In preliminary measurements on different bi-layer graphene samples, three-fold or six-fold symmetric patterns are observed in constant energy maps of the transmission function, most likely reflecting the two stacking orders of bi-layer graphene. In future studies, angle-resolved electron transmission measurements could be performed on other two-dimensional materials provided that they are sufficiently transparent to low-energy electrons and can be prepared freestanding. Possible candidates are few layer graphene sheets, twisted bi-layer graphene, single layer hexagonal boron nitride/graphene compounds, exfoliated single layer molybdenum disulphide or heterostructures of graphene and transitional metal dichalcogenides.

In a further application of the new experimental setup, non-reconstructable features observed in low-energy electron holograms of freestanding graphene samples were investigated and identified to arise due to charged adsorbates. The high sensitivity of low-energy electrons to local variations in an electric potential is employed to directly visualize charge distributions with a sensitivity of a fraction of an elementary charge. Moreover, spatial resolution in the nanometer range and fast data acquisition inherent to lens-less low-energy electron holography allows for direct visual inspection of charge transfer processes and adsorbate diffusion.

Bibliography

[1] E. Abbe,
Beiträge zur Theorie des Mikroskops und der mikroskopischen Wahrnehmung,
Archiv für mikroskopische Anatomie **9**, 413–418 (1873).

[2] M. Knoll and E. Ruska,
Beitrag zur geometrischen Elektronenoptik I und II,
Annalen der Physik **12**, 607–661 (1932).

[3] E. Ruska,
The development of the electron microscope and of electron microscopy,
Bioscience Reports **7**, 607–629 (1987).

[4] O. Scherzer,
Über einige Fehler von Elektronenlinsen,
Zeitschrift für Physik **101**, 593–603 (1936).

[5] D. Gabor,
A New Microscopic Principle,
Nature **161**, 777–778 (1948).

[6] O. Scherzer,
Sphärische und chromatische Korrektur von Elektronen-Linsen,
Optik **2**, 114–132 (1947).

[7] H. H. Rose,
Historical aspects of aberration correction,
Journal of Electron Microscopy **58**, 77–85 (2009).

[8] U. Kaiser, J. Meyer, J. Biskupek, J. Leschner, A. N. Khlobystov, H. Müller, P. Hartel, M. Haider, S. Eyhusen and G. Benner,

High Resolution 20kV Transmission Electron Microscopy of Nanosystems – First Results Towards Sub Ångstrom Low Voltage EM (SALVE – Microscopy),
Microscopy and Microanalysis **16**, 1702–1703 (2010).

[9] T. Zoberbier, T. W. Chamberlain, J. Biskupek, M. Suyetin, A. G. Majouga, E. Besley, U. Kaiser and A. N. Khlobystov,
Investigation of the Interactions and Bonding between Carbon and Group VIII Metals at the Atomic Scale,
Small **12**, 1649–1657 (2016).

[10] T. Sasaki, H. Sawada, F. Hosokawa, Y. Kohno, T. Tomita, T. Kaneyama, Y. Kondo, K. Kimoto, Y. Sato and K. Suenaga,
Performance of low-voltage STEM/TEM with delta corrector and cold field emission gun,
Journal of Electron Microscopy **59**, S7–S13 (2010).

[11] N. Dellby, N. J. Bacon, P. Hrncirik, M. F. Murfitt, G. S. Skone, Z. S. Szilagyi and O. L. Krivanek,
Dedicated STEM for 200 to 40 keV operation,
The European Physical Journal Applied Physics **54**, 33505 (2011).

[12] T. Sasaki, H. Sawada, F. Hosokawa, Y. Sato and K. Suenaga,
Aberration-corrected STEM/TEM imaging at 15kV,
Ultramicroscopy **145**, 50–55 (2014).

[13] E. Knapek and J. Dubochet,
Beam damage to organic material is considerably reduced in cryo-electron microscopy,
Journal of Molecular Biology **141**, 147–161 (1980).

[14] M. van Heel, B. Gowen, R. Matadeen, E. V. Orlova, R. Finn, T. Pape, D. Cohen, H. Stark, R. Schmidt, M. Schatz and A. Patwardhan,
Single-particle electron cryo-microscopy: towards atomic resolution,
Quarterly Reviews of Biophysics **33**, 307–369 (2000).

[15] R. F. Egerton, P. Li and M. Malac,
Radiation damage in the TEM and SEM,
Micron **35**, 399–409 (2004).

[16] M. Germann, T. Latychevskaia, C. Escher and H.-W. Fink,
Nondestructive Imaging of Individual Biomolecules,
Physical Review Letters **104**, 095501 (2010).

[17] T. Latychevskaia, J.-N Longchamp, C. Escher and H.-W. Fink,
Holography and coherent diffraction with low-energy electrons: A route towards structural biology at the single molecule level,
Ultramicroscopy **159 II**, 395 – 402 (2015).

[18] H.-W. Fink,
Point source for ions and electrons,
Physica Scripta **38**, 260 (1988).

[19] R. Morin,
Point source physics: Application to electron projection microscopy and holography,
Microscopy Microanalysis Microstructures **5**, 501–508 (1994).

[20] R. Gomer,
Field emission and field ionization,
Harvard University Press, Cambridge, (1961).

[21] L. W. Swanson and L. C. Crouser,
Total-Energy Distribution of Field-Emitted Electrons and Single-Plane Work Functions for Tungsten,
Physical Review **163**, 622–641 (1967).

[22] H.-W. Fink, W. Stocker and H. Schmid,
Holography with low-energy electrons,
Physical Review Letters **65**, 1204–1206 (1990).

[23] T. Latychevskaia and H.-W. Fink,
Practical algorithms for simulation and reconstruction of digital in-line holograms,
Applied Optics **54**, 2424–2434 (2015).

[24] V. T. Binh, V. Semet and N. Garcia,
Low-energy-electron diffraction by nano-objects in projection microscopy without magnetic shielding,
Applied Physics Letters **65**, 2493–2495 (1994).

[25] M. P. Silverman, W. Strange and J. C. H. Spence,
The brightest beam in science: New directions in electron microscopy and interferometry,
American Journal of Physics **63**, 800–813 (1995).

[26] M. Prigent and P. Morin,
Charge effect in point projection images of carbon fibres,
Journal of Microscopy **199**, 197–207 (2000).

[27] V. T. Binh, P. Vincent, F. Feschet and J.-M. Bonard,
Local analysis of the morphological properties of single-wall carbon nanotubes by Fresnel projection microscopy,
Journal of Applied Physics **88**, 3385–3391 (2000).

[28] I. S. Hwang, C. C. Chang, C. H. Lu, S. C. Liu, Y. C. Chang, T. K. Lee, H. T. Jeng, H. S. Kuo, C. Y. Lin, C. S. Chang and T. T. Tsong,
Investigation of single-walled carbon nanotubes with a low-energy electron point projection microscope,
New Journal of Physics **15**, 043015 (2013).

[29] J. Bardon, A. Degiovanni, V. Georges and R. Morin,
Conducting, semiconducting and insulating objects observed by low-energy electron holography,
Ultramicroscopy **92**, 133–142 (2002).

[30] J. Bardon, V. Georges, A. Degiovanni and R. Morin,
Improved low energy electron projection in-line holograms reconstruction: application to the holograms of a tungsten tip,
Micron **33**, 493–497 (2002).

[31] H.-W. Fink, H. Schmid, E. Ermantraut and T. Schulz,
Electron holography of individual DNA molecules,
J. Opt. Soc. Am. A **14**, 2168–2172 (1997).

[32] A. Eisele, B. Völkel, M. Grunze and A. Gölzhäuser,
Nanometer Resolution Holography with the Low Energy Electron Point Source Microscope,
Zeitschrift für Physikalische Chemie **222**, 779–787 (2008).

[33] M. Germann, T. Latychevskaia, C. Escher and H.-W. Fink,
Pulsed electron holography,
Applied Physics Letters **102**, 203115 (2013).

[34] A. Gölzhäuser, B. Völkel, B. Jäger, M. Zharnikov, H. J. Kreuzer and M. Grunze,
Holographic imaging of macromolecules,
Journal of Vacuum Science & Technology A **16**, 3025–3028 (1998).

[35] U. Weierstall, J. C. H. Spence, M. Stevens and K. H. Downing,
Point-projection electron imaging of tobacco mosaic virus at 40 eV electron energy,
Micron **30**, 335–338 (1999).

[36] J.-N. Longchamp, T. Latychevskaia, C. Escher and H.-W. Fink,
Low-energy electron holographic imaging of individual tobacco mosaic virions,
Applied Physics Letters **107**, 133101 (2015).

[37] G. B. Stevens, M. Krüger, T. Latychevskaia, P. Lindner, A. Plückthun and H.-W. Fink,
Individual filamentous phage imaged by electron holography,
European Biophysics Journal **40**, 1197–1201 (2011).

[38] J.-N. Longchamp, T. Latychevskaia, C. Escher and H.-W. Fink,
Non-destructive imaging of an individual protein,
Applied Physics Letters **101**, 093701 (2012).

[39] D. Sayre,
Some implications of a theorem due to Shannon,
Acta Crystallographica **5**, 843–843 (1952).

[40] R. W. Gerchberg and W. O. Saxton,
A practical algorithm for the determination of phase from image and diffraction plane pictures,
Optik **35**, 237–246 (1972).

[41] J. R. Fienup,
Reconstruction of an object from the modulus of its Fourier transform,
Optics Letters **3**, 27–29 (1978).

[42] E. Steinwand, J.-N. Longchamp and H.-W. Fink,
Fabrication and characterization of low aberration micrometer-sized electron lenses,
Ultramicroscopy **110**, 1148–1153 (2010).

[43] E. Steinwand, J.-N. Longchamp and H.-W. Fink,
Coherent low-energy electron diffraction on individual nanometer sized objects,
Ultramicroscopy **111**, 282–284 (2011).

[44] T. Latychevskaia, J.-N. Longchamp and H.-W. Fink,
When holography meets coherent diffraction imaging,
Opt. Express **20**, 28871–28892 (2012).

[45] J.-N. Longchamp, T. Latychevskaia, C. Escher and H.-W. Fink,
Graphene unit cell imaging by holographic coherent diffraction,
Physical Review Letters **110**, 255501 (2013).

[46] J. Y. Mutus, L. Livadaru, J. T. Robinson, R. Urban, M. H. Salomons, M. Cloutier and R. A. Wolkow,

Low-energy electron point projection microscopy of suspended graphene, the ultimate 'microscope slide',
New Journal of Physics **13**, 063011 (2011).

[47] J.-N. Longchamp, T. Latychevskaia, C. Escher and H.-W. Fink,
Low-energy electron transmission imaging of clusters on free-standing graphene,
Applied Physics Letters **101**, 113117 (2012).

[48] M. Haider, S. Uhlemann, E. Schwan, H. Rose, B. Kabius and K. Urban,
Electron microscopy image enhanced,
Nature **392**, 768–769 (1998).

[49] P. W. Hawkes,
Aberration correction past and present,
Philosophical Transactions of the Royal Society A – Mathematical Physical and Engineering Sciences **367**, 3637–3664 (2009).

[50] U. Kaiser, J. Biskupek, J. C. Meyer, J. Leschner, L. Lechner, H. Rose, M. Stöger-Pollach, A. N. Khlobystov, P. Hartel, H. M¸ller, M. Haider, S. Eyhusen and G. Benner,
Transmission electron microscopy at 20 kV for imaging and spectroscopy,
Ultramicroscopy **111**, 1239–1246 (2011).

[51] Z. Lee, H. Rose, O. Lehtinen, J. Biskupek and U. Kaiser,
Electron dose dependence of signal-to-noise ratio, atom contrast and resolution in transmission electron microscope images,
Ultramicroscopy **145**, 3–12 (2014).

[52] W. Telieps and E. Bauer,
Low energy electron microscopy of surfaces,
Surface Science **200**, 512–513 (1988).

[53] R. M. Tromp, J. B. Hannon, A. W. Ellis, W. Wan, A. Berghaus and O. Schaff,
A new aberration-corrected, energy-filtered LEEM/PEEM instrument. I. Principles and design,
Ultramicroscopy **110**, 852–861 (2010).

[54] T. Schmidt, H. Marchetto, P. L. Levesque, U. Groh, F. Maier, D. Preikszas, P. Hartel, R. Spehr, G. Lilienkamp, W. Engel, R. Fink, E. Bauer, H. Rose, E. Umbach and H. J. Freund,
Double aberration correction in a low-energy electron microscope,
Ultramicroscopy **110**, 1358–1361 (2010).

[55] I. Mullerova and L. Frank,
Very Low Energy Scanning Electron Microscopy,
Modern Research and Educational Topics in Microscopy , 795–804 (2007).

[56] I. Mullerova, M. Hovorka, R. Hanzlikova and L. Frank,
Very Low Energy Scanning Electron Microscopy of Free-Standing Ultrathin Films,
Materials Transactions **51**, 265–270 (2010).

[57] T. H. P. Chang, D. P. Kern and L. P. Muray,
Microminiaturization of electron-optical systems,
Journal of Vacuum Science & Technology B **8**, 1698–1705 (1990).

[58] G. M. Shedd, H. Schmid, P. Unger, H.-W. Fink and A. D. Dubner,
Combinations of point source electron beams and simple electrostatic lenses: Initial demonstrations of micron-scale lenses,
Review of Scientific Instruments **64**, 2579–2584 (1993).

[59] G. M. Shedd, H. Schmid and H.-W. Fink,
Building a micrometer-scale electrostatic lens by hand,
Ultramicroscopy **48**, 43–48 (1993).

[60] M. Despont, U. Staufer, C. Stebler, R. Germann and P. Vettiger,
Microfabrication of lenses for a miniaturized electron column,
Microelectronic Engineering **27**, 467–470 (1995).

[61] G. Binnig, H. Rohrer, C. Gerber and E. Weibel,
Surface Studies by Scanning Tunneling Microscopy,
Physical Review Letters **49**, 57–61 (1982).

[62] G. Binnig, H. Rohrer, C. Gerber and E. Weibel,
7×7 *Reconstruction on Si(111) Resolved in Real Space*,
Physical Review Letters **50**, 120–123 (1983).

[63] E. Meyer, H. J. Hug and R. Bennewitz,
Scanning Probe Microscopy: The Lab on a Tip, 1st ed.,
Springer, New York, (2003).

[64] B. Buhshan and H. Fuchs,
Applied Scanning Probe Methods II: Scanning Probe Microscopy Techniques, NanoScience and Technology, 1st ed.,
Springer, New York, (2006).

[65] J. Tersoff and D. R. Hamann,
Theory and Application for the Scanning Tunneling Microscope,
Physical Review Letters **50**, 1998–2001 (1983).

[66] J. Tersoff and D. R. Hamann,
Theory of the Scanning Tunneling Microscope,
Physical Review B **31**, 805–810 (1985).

[67] R. Young, J. Ward and F. Scire,
The Topografiner: An Instrument for Measuring Surface Microtopography,
Review of Scientific Instruments **43**, 999–1011 (1972).

[68] T. L. Kirk, U. Ramsperger and D. Pescia,
Theory of the Scanning Tunneling Microscope,
Journal of Vacuum Science & Technology B **27**, 152–155 (2009).

[69] D. A. Zanin, M. Erbudak, L. G. De Pietro, H. Cabrera, A. Redmann, A. Fognini, T. Michlmayr, Y. M. Acremann, D. Pescia and U. Ramsperger,
The Topografiner with Energy Analysis,
Proceeding of the 26th International Vacuum Nanoelectronics Conference , IEEE (2012).

[70] L. Livadaru, J. Mutus and R. A. Wolkow,
In-line holographic electron microscopy in the presence of external magnetic fields,
Ultramicroscopy **108**, 472–480 (2008).

[71] S. Park and C. F. Quate,
Theories of the feedback and vibration isolation systems for the scanning tunneling microscope,
Review of Scientific Instruments **58**, 2004–2009 (1987).

[72] R. A. Sun, Q. Wolkow and M. Salomons,
Low frequency vibration isolation through an active-on-active approach: Coupling effects,
Journal of Vibration and Acoustics **131**, 061010 (2009).

[73] J. P. Ibe, P. P. Bey, S. L. Brandow, R. A. Brizzolara, N. A. Burnham, D. P. DiLella, K. P. Lee, C. R. K. Marrian and R. J. Colton,
On the electrochemical etching of tips for scanning tunneling microscopy,
Journal of Vacuum Science & Technology A **8**, 3570–3575 (1990).

[74] R. Zhang and D. G. Ivey,
Preparation of sharp polycrystalline tungsten tips for scanning tunneling microscopy imaging,
Journal of Vacuum Science & Technology B **14**, 1–10 (1996).

[75] M. Klein and G. Schwitzgebel,
An improved lamellae drop-off technique for sharp tip preparation in scanning tunneling microscopy,
Review of Scientific Instruments **68**, 3099–3103 (1997).

[76] D. Xu, K. M. Liechti and K. Ravi-Chandar,
Mesoscale scanning probe tips with subnanometer rms roughness,
Review of Scientific Instruments **78**, 073707 (2007).

[77] A. P. Janssen and J. P. Jones,
The sharpening of field emitter tips by ion sputtering,
Journal of Physics D: Applied Physics **4**, 118 (1971).

[78] C. Schiller, A. A. Koomans, T. L. van Rooy, C. Schönenberger and H. B. Elswijk,
Decapitation of tungsten field emitter tips during sputter sharpening,
Surface Science **339**, 925 – 930 (1995).

[79] P. Zahl, M. Bierkandt, S. Schroder and A. Klust,
The Flexible and Modern Open Source Scanning Probe Microscopy Software Package GXSM,
Review of Scientific Instruments **74**, 1222–1227 (2003).

[80] P. Zahl, T. Wagner, R. Möller and A. Klust,
Open Source Scanning Probe Microscopy Control Software Package GXSM,
Journal of Vacuum Science & Technology B **28**, C4E39 (2010).

[81] P. Zahl and T. Wagner,
Smart & Customizable SPM Control,
Review of Scientific Instruments **17**, 38–41 (2015).

[82] R. Morin and A. Gargani,
Ultra-low-energy-electron projection holograms,
Physical Review B **48**, 6643–6645 (1993).

[83] D. J. Alton,
Interacting single atoms with nanophotonics for chip-integrated quantum networks,
PhD thesis, California Institute of Technology, 2013.

[84] V. U. Nazarov, E. E. Krasovskii and V. M. Silkin,
Scattering resonances in two-dimensional crystals with application to graphene,
Physical Review B **87**, 041405 (2013).

[85] N. V. Smith, M. M. Traum and F. J. Di Salvo,
Mapping energy bands in layer compounds from the angular dependence of ultraviolet photoemission,
Solid State Communications **15**, 211–214 (1974).

[86] P. J. Feibelman and D. E. Eastman,
Photoemission spectroscopy – Correspondence between quantum theory and experimental phenomenology,
Physical Review B **10**, 4932–4947 (1974).

[87] S. Hüfner,
Photoelectron Spectroscopy - Principles and Applications,
Springer, (2010).

[88] D. Andrea,
Probing the Electronic Structure of Complex Systems by ARPES,
Physica Scripta **109**, 61–74 (2004).

[89] V. N. Strocov,
Low energy electron reflection: Possibility for E(k) points mapping above the vacuum level,
Solid State Communications **78**, 845–847 (1991).

[90] V. N. Strocov,
Bandstructure effects in VeryLEED,
International Journal of Modern Physics B **09**, 1755–1796 (1995).

[91] I. Bartos,
Electronic structure of crystals via VLEED,
Progress in Surface Science **59**, 197–206 (1998).

[92] F. Maeda, T. Takahashi, H. Ohsawa, S. Suzuki and H. Suematsu,
Unoccupied-electronic-band structure of graphite studied by angle-resolved secondary-electron emission and inverse photoemission,
Physical Review B **37**, 4482–4488 (1988).

[93] M. Bovet, V. N. Strocov, F. Clerc, C. Koitzsch, D. Naumovic and P. Aebi,
Excited States Mapped by Secondary Photoemission,
Physical Review Letters **93**, 107601 (2004).

[94] P. R. Wallace,
The Band Theory of Graphite,
Physical Review **71**, 622–634 (1947).

[95] K. S. Novoselov, A. K. Geim, S. V. Morozov, D. Jiang, Y. Zhang, S. V. Dubonos, I. V. Grigorieva and A. A. Firsov,
Electric Field Effect in Atomically Thin Carbon Films,
Science **306**, 666–669 (2004).

[96] S. Latil and L. Henrard,
Charge Carriers in Few-Layer Graphene Films,
Physical Review Letters **97**, 036803 (2006).

[97] E. Kogan and V. U. Nazarov,
Symmetry classification of energy bands in graphene,
Physical Review B **85**, 115418 (2012).

[98] Y. Liu, L. Zhang, M. K. Brinkley, G. Bian, T. Miller and T. C. Chiang,
Phonon-Induced Gaps in Graphene and Graphite Observed by Angle-Resolved Photoemission,
Physical Review Letters **105**, 136804 (2010).

[99] D. Niesner, Th. Fauster, J. I. Dadap, N. Zaki, K. R. Knox, P. C. Yeh, R. Bhandari, R. M. Osgood, M. Petrovic and M. Kralj,
Trapping surface electrons on graphene layers and islands,
Physical Review B **85**, 081402 (2012).

[100] K. R. Knox, A. Locatelli, M. B. Yilmaz, D. Cvetko, T. O. Mentes, M. A. Nino, P. Kim, A. Morgante and R. M. Osgood,
Making angle-resolved photoemission measurements on corrugated monolayer crystals: Suspended exfoliated single-crystal graphene,
Physical Review B **84**, 115401 (2011).

[101] I. Razado-Colambo, J. Avila, C. Chen, J. P. Nys, X. Wallart, M. C. Asensio and D. Vignaud,
Probing the electronic properties of graphene on C-face SiC down to single domains by nanoresolved photoelectron spectroscopies,
Physical Review B **92**, 035105 (2015).

[102] M. Pisarra, P. Riccardi, A. Sindona, A. Cupolillo, N. Ligato, C. Giallombardo and L. Caputi,
Probing graphene interfaces with secondary electrons,
Carbon **77**, 796–802 (2014).

[103] E. E. Krasovskii,
Augmented-plane-wave approach to scattering of Bloch electrons by an interface,
Physical Review B **70**, 245322 (2004).

[104] J. Jobst, J. Kautz, D. Geelen, R. M. Tromp and S. J. van der Molen,
Nanoscale measurements of unoccupied band dispersion in few-layer graphene,
Nature Communications **6** (2015).

[105] J.-N. Longchamp, C. Escher and H.-W. Fink,
Ultraclean freestanding graphene by platinum-metal catalysis,
Journal of Vacuum Science & Technology B **31**, 020605 (2013).

[106] H. Zhu, Y: Wang, J. Xiao, M. Liu, S. Xiong, Z. J. Wong, Z. Ye, Y. Ye, X. Yin and X. Zhang,
Observation of piezoelectricity in free-standing monolayer MoS_2,
Nature Nanotechnology **10**, 151–155 (2015).

[107] A. Azizi, S. Eichfeld, G. Geschwind, K. Zhang, B. Jiang, D. Mukherjee, L. Hossain, A. F. Piasecki, B. Kabius, J. A. Robinson and N. Alem,
Freestanding van der Waals Heterostructures of Graphene and Transition Metal Dichalcogenides,
ACS Nano **9**, 4882–4890 (2015).

[108] M. J. Yoo, T. A. Fulton, H. F. Hess, R. L. Willett, L. N. Dunkleberger, R. J. Chichester, L. N. Pfeiffer and K. W. West,
Scanning single-electron transistor microscopy: Imaging individual charges,
Science **276**, 579–582 (1997).

[109] M. T. Woodside and P. L. McEuen,
Scanned probe imaging of single-electron charge states in nanotube quantum dots,
Science **296**, 1098–1101 (2002).

[110] L. Cockins, Y. Miyahara, S. D. Bennett, A. A. Clerk, S. Studenikin, P. Poole, A. Sachrajda and P. Grutter,
Energy levels of few-electron quantum dots imaged and characterized by atomic force microscopy,
Proceedings of the National Academy of Sciences of the United States of America **107**, 9496Ò9501 (2010).

[111] C. Gatel, A. Lubk, G. Pozzi, E. Snoeck and M. Hytch,
Counting elementary charges on nanoparticles by electron holography,
Physical Review Letters **111**, 025501 (2013).

[112] R. R. Nair, P. Blake, J. R. Blake, R. Zan, S. Anissimova, U. Bangert, A. P. Golovanov, S. V. Morozov, A. K. Geim, K. S. Novoselov and T. Latychevskaia,
Graphene as a transparent conductive support for studying biological molecules by transmission

electron microscopy,
Applied Physics Letters **97**, 153102 (2010).

[113] F. Schaffel, M. Wilson and J. H. Warner,
Motion of light adatoms and molecules on the surface of few-layer graphene,
ACS Nano **5**, 9428–9441 (2011).

[114] G. Algara-Siller, O. Lehtinen, A. Turchanin and U. Kaiser,
Dry-cleaning of graphene,
Applied Physics Letters **104**, 153115 (2014).

[115] J. C. Meyer, C. O. Girit, M. F. Crommie and A. Zettl,
Imaging and dynamics of light atoms and molecules on graphene,
Nature **454**, 319–322 (2008).

[116] T. Susi, J. Kotakoski, D. Kepaptsoglou, C. Mangler, T. C. Lovejoy, O. L. Krivanek, R. Zan, U. Bangert, P. Ayala, J. C. Meyer and Q. Ramasse,
Silicon-carbon bond inversions driven by 60-keV electrons in graphene,
Physical Review Letters **113**, 115501 (2014).

[117] X. J. Liu, C. Z. Wang, M. Hupalo, H. Q. Lin, K. M. Ho and M. C. Tringides,
Metals on graphene: interactions, growth morphology, and thermal stability,
Crystals **3**, 79–111 (2013).

[118] O. U. Akturk and M. Tomak,
Au_nPt_n clusters adsorbed on graphene studied by first-principles calculations,
Physical Review B **80**, 085417 (2009).

[119] O. Leenaerts, B. Partoens and F. M. Peeters,
Adsorption of H_2O, NH_3, CO, NO_2, and NO on graphene: A first-principles study,
Physical Review B **77**, 125416 (2008).

[120] D. Gabor,
Microscopy by reconstructed wave-fronts,
Proceedings of the Royal Society of London Series A – Mathematical and Physical Sciences **197**, 454–487 (1949).

[121] T. Latychevskaia and H.-W. Fink,
Simultaneous reconstruction of phase and amplitude contrast from a single holographic record,
Optics Express **17**, 10697–10705 (2009).

[122] T. Latychevskaia, J.-N. Longchamp, C. Escher and H.-W. Fink,
On artefact-free reconstruction of low-energy (30-250 eV) electron holograms,
Ultramicroscopy **145**, 22–27 (2014).

[123] T. Latychevskaia and H.-W. Fink,
Solution to the twin image problem in holography,
Physical Review Letters **98**, 233901 (2007).

[124] T. Latychevskaia and H.-W. Fink,
Reconstruction of purely absorbing, absorbing and phase-shifting, and strong phase-shifting objects from their single-shot in-line holograms,
Applied Optics **54**, 3925–3932 (2015).

[125] P. Serp and B. Machado,
Nanostructured Carbon Materials for Catalysis,
Royal Society of Chemistry, (2013).

[126] A. Ishii, M. Yamamoto, H. Asano and K. Fujiwara,
DFT calculation for adatom adsorption on graphene sheet as a prototype of carbon nano tube functionalization,
Journal of Physics: Conference Series **100**, 052087 (2008).

[127] T. P. Hardcastle, C. R. Seabourne, R. Zan, R. M. D. Brydson, U. Bangert, Q. M. Ramasse, K. S. Novoselov and A. J. Scott,
Mobile metal adatoms on single layer, bilayer, and trilayer graphene: An ab initio DFT study with van der Waals corrections correlated with electron microscopy data,
Physical Review B **87**, 195430 (2013).

[128] NIST,
NIST electron elastic-scattering cross-section database, (2000).

[129] L. D. Landau and E. M. Lifshitz,
Quantum Mechanics: Non-Relativistic Theory (Course of Theoretical Physics). Third Edition ed.,
Pergamon Press: Oxford, (1977).

[130] T. Latychevskaia and H.-W. Fink,
Atomically Resolved Structural Determination of Graphene and its Point Defects via Extrapolation Assisted Phase Retrieval,
Applied Physics Letters **106**, 021908 (2015).

[131] E. E. Krasovskii, W. Schattke, V. N. Strocov and R. Claessen,
Unoccupied band structure of $NbSe_2$ *by very low-energy electron diffraction: Experiment and theory*,
Phys. Rev. B **66**, 235403 (2002).

Curriculum Vitae

Personal

name	Flavio Bruno WICKI
date of birth	26.08.1986
place of citizenship	Aristau, AG

University education

2012 – 2016	Doctoral program in physics at the University of Zurich in the group of Prof. H.-W. Thesis title: *Four Novel Electron Point Source Applications*.
2012	Master of Science University of Zurich in Physics in the group of Prof. H.-W. Fink Thesis title: *Design and Implementation of a Miniaturized Electron Optical Column*.
2010 – 2012	Master program of the University of Zurich in Condensed Matter Physics
2010	Bachelor of Science University of Zurich in Physics in the group of Prof. H.-W. Fink Thesis title: *Kohärente Beugung niederenergetischer Elektronen: Beamstop und Probenpräparation*.
2006 – 2010	Bachelor of Science University of Zurich in Physics

School education

2005	Matura SF Mathematik und Physik, Kantonsschule Sursee
1999 – 2005	Kantonsschule Sursee
1993 – 1999	Primarschule Sursee

List of publications

- **F. Wicki**, J.-N. Longchamp, C. Escher, H.-W. Fink
  Design and Implementation of a Micron-Sized Electron Column Fabricated by Focused Ion Beam Milling.
  Ultramicroscopy **160**, 74–79 (2016).
- **F. Wicki**, J.-N. Longchamp, T. Latychevskaia, C. Escher, H.-W. Fink
  Mapping Unoccupied Electronic States of Freestanding Graphene by Angle-Resolved Low-Energy Electron Transmission.
  Physical Review B, **94**, 075424 (2016).
- T. Latychevskaia, **F. Wicki**, J.-N. Longchamp, C. Escher, H.-W. Fink
  Direct Observation of Individual Charges and their Dynamics on Graphene by Low-Energy Electron Holography.
  Nano Letters, *in press*.

Acknowledgements

I would like to thank Hans-Werner Fink, Conrad Escher, Jean-Nicolas Longchamp and Tatiana Latychevskaia for guiding and supporting me throughout my PhD.

I would like to thank the additional members of the committee: Jürg Osterwalder, Peter Hommelhoff and Roger Morin for generously offering their time, the pleasant meetings and valuable inputs for my work.

A special thanks goes to Percy Zahl, Thorsten Wagner and Alex Boudreau for their help regarding GXSM and the SPM controller and to Thomas Bähler for his assistance concerning the current-to-voltage converter. Thanks to Eugene Krasovskii for fruitful discussions about unoccupied states in graphene and ab-initio band structure calculation.